WEATHER & CLIMATE

JOURNAL OF THE METEOROLOGICAL SOCIETY OF NEW ZEALAND (INC.)

VOLUME 42 | ISSUE 1 | 2023

WEATHER & CLIMATE

JOURNAL OF THE METEOROLOGICAL SOCIETY OF NEW ZEALAND (INC.)

VOLUME 42 | ISSUE 1 | 2023

ISSN 0111-5499

Weather & Climate is the official journal of the Meteorological Society of New Zealand (Inc.). Any opinions, statements or recommendations expressed in this journal are those of the respective author(s) and do not necessarily reflect the views of the Meteorological Society of New Zealand (Inc.).

Contributions to *Weather & Climate* are welcome on any meteorological or climatological subject, but preference will be given to contributions related to New Zealand and/or the Southwest Pacific.

Submissions can be made via Scholastica at: https://weather-and-climate.scholasticahq.com/ or by emailing the editor at: nava.fedaeff@niwa.co.nz

Published: April 2023

EDITORS Nava Fedaeff, Petra Pearce
EDITORIAL ADVISOR Colin Barkus

COVER IMAGE Ben Cloke

"In August 2022 we had a couple of super foggy days in Auckland and I had seen images like this pop up on social media. There was no way I would miss this so the next morning at the crack of dawn my partner and I walked up Mt Eden. We caught this stunner of a scene (along with every single other photographer in Auckland!)"

THE METEOROLOGICAL SOCIETY OF NEW ZEALAND (INC.)

The Meteorological Society of New Zealand (Inc.) was inaugurated in October 1979. The objects of the Society are to encourage an interest in the atmosphere, the weather and the climate, particularly in the New Zealand and South Pacific regions. Membership is open to all those with an interest in the objects of the Society. Membership comprises both professionals and amateurs including meteorologists, climatologists, geographers, hydrologists, yachting and tramping enthusiasts, glider pilots, people involved in aviation and marine industries, agriculturalists, professional weather forecasters, ecologists, economists, farmers, engineers and weather observers.

Membership fees:

Ordinary members	$40.00
Student/retired/unwaged members	$20.00
Institutional members	$120.00
Overseas postage surcharge	$15.00

All members receive copies of *Weather and Climate* and the quarterly newsletter (which includes details of significant weather events in the previous period).

Correspondence:
The Secretary
Meteorological Society of New Zealand
PO Box 6523, Marion Square, Wellington, 6141, New Zealand
Web site: https://www.metsoc.org.nz/

Contents

A case of spillover rain coinciding with bushfire smoke

Fulong Lu[1] and Chris Webster[1]

[1] Meteorological Service of New Zealand (MetService – Te Ratonga Tirorangi), PO Box 722, Wellington, New Zealand
Corresponding author: Fulong Lu, fulong.lu@metservice.com

KEY WORDS
Heavy rain, thunderstorm, lightning, smoke, bushfire, spillover, ice nuclei, forecasting

ABSTRACT

Spillover rain occurs when orographically enhanced rain on the windward side of a mountain range is blown onto the lee side of the range. In Canterbury, this typically occurs in a strong northwesterly airstream ahead of an active front moving up the South Island of New Zealand (NZ). These northwesterly airstreams are of two types: one is a more common situation with a statically stable airmass, and the other involves an unstable airmass.

In general, northwesterly winds bring dry weather to the Canterbury Plains ahead of fronts. In a statically stable northwesterly storm, the rainfall maximum occurs on the windward upper slope of the Southern Alps. In an unstable northwesterly storm, the rainfall maximum shifts to the main divide of the Southern Alps, bringing wet weather ahead of the front in Canterbury. The storm of 6 - 7 December 2019 occurred in a particularly unstable environment (very large Total-Totals and CAPE) with strong upward motion on the West Coast and involved smoke particles from Australian bushfires.

The storm produced a new 24-hour lightning strike record and extensive rain and lightning across the Southern Alps and into South Canterbury, leading to the Rangitata River flooding onto the Canterbury Plains. The mechanism for such lightning to spread east to the Canterbury coast is explored. A secondary rainfall maximum was found on the South Canterbury coast under a quasi-stationary leeward mountain wave. The smoke particles likely played a role in the spillover and lightning. A conceptual model of enhanced spillover rain due to smoke particles in an unstable northwest flow is proposed.

1. INTRODUCTION

Orographic effects on precipitation have been studied by meteorologists around the world (e.g., Browning et al., 1974; Collier, 1975; Marwitz, 1980; Henderson, 1993; Singh et al.,1995). Several studies into the orographic influences on weather have been made in NZ, especially in the 1990s with the Southern Alps Experiment (e.g., SALPEX, Wratt, et al., 1996). The distribution and spillover of precipitation in the Southern Alps have been explored (Sinclair et al., 1997), including the influence of atmospheric conditions on spillover (Chater, et al., 1998; Wratt, et al., 2000). Detailed studies of spillover heavy precipitation in the Southern Alps when smoke particles were present have not been carried out.

The Southern Alps run an approximately 500km NE-SW oriented barrier to the predominantly westerly flow over NZ's South Island. Many peaks exceed 2500m in altitude between Westland and Canterbury (Figure 1).

When a cold front moves up the South Island, rain falls in the west ahead of the front, followed by a clearance or partial clearance. In the east, high clouds spread ahead of the front, and rain typically falls behind it in the post-frontal southerly or southwesterly airstream. Near the front, rain

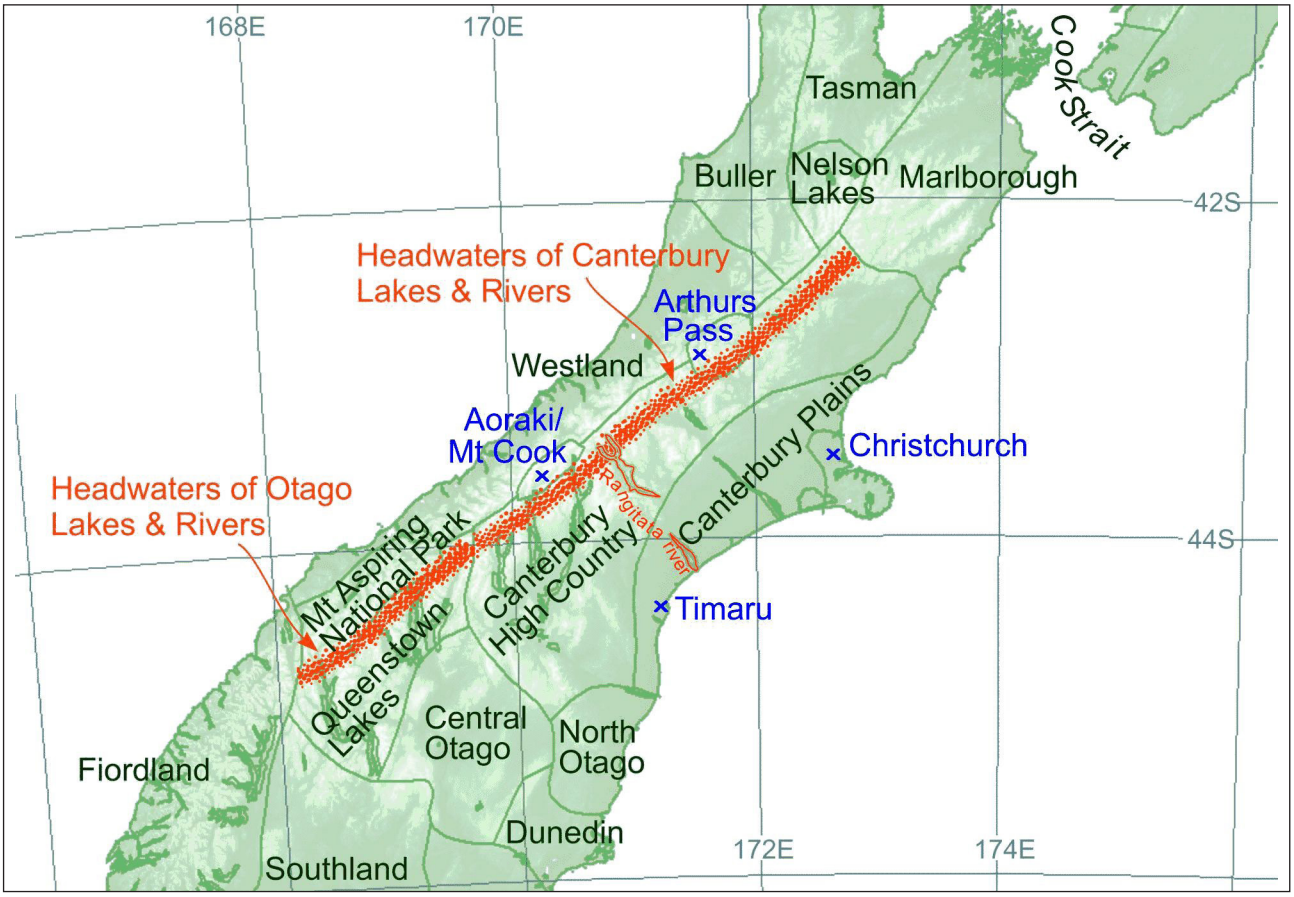

Figure 1: Map of the South Island with regional names and simplified topography. Main locations mentioned in the paper are marked, including the headwaters of the Otago and Canterbury lakes and rivers, and the Rangitata River (red).

spills over the headwaters of the Canterbury (and Otago) lakes and rivers, with a rain shadow further east. Figure 2 shows this weather pattern when the pre-frontal airmass is statically stable.

The extent of spillover heavy rain depends on:

1. the static stability of the pre-frontal airmass,
2. the baroclinicity of the front,
3. the amount of moisture advected in from upstream,
4. the vertical wind profile west of the mountains (both speed and direction),
5. the amount of upper-level divergence, and
6. the speed of movement of the front.

Further to point 1, in unstable northwesterly airstreams, rain ahead of the front spreads more readily across the Southern Alps onto the Canterbury Plains.

Many extreme weather events (EWEs) in NZ are associated with atmospheric rivers (ARs) (Reid et al., 2021; Little et al., 2019; Kingston et al., 2016), however, little is known about the effect of smoke particle ingestion on EWEs. The case study presented in this paper involves bushfire smoke particles. The aim is to better understand smoke particles' effect on atmospheric instability and cloud physics, and how that could enhance spillover heavy rain. It is also intended to improve the forecasting of EWEs.

2. DATA SOURCES

2.1 Rainfall observations and satellite

Rainfall data used in this paper are from NZ MetService real-time hourly data and NZ Regional Council rainfall data. Visible, infrared and water vapour satellite imagery are from the Himawari-8 geostationary satellite of the Japan Meteorological Agency (JMA), except for Figure 6 from the Terra MODIS Corrected Reflectance (True Colour) data supplied by NASA.

2.2 Radar

The NZ MetService weather radar network is comprised of ten C-band radars. Data from two of these radars, Westland and Canterbury, are used in this study. These two

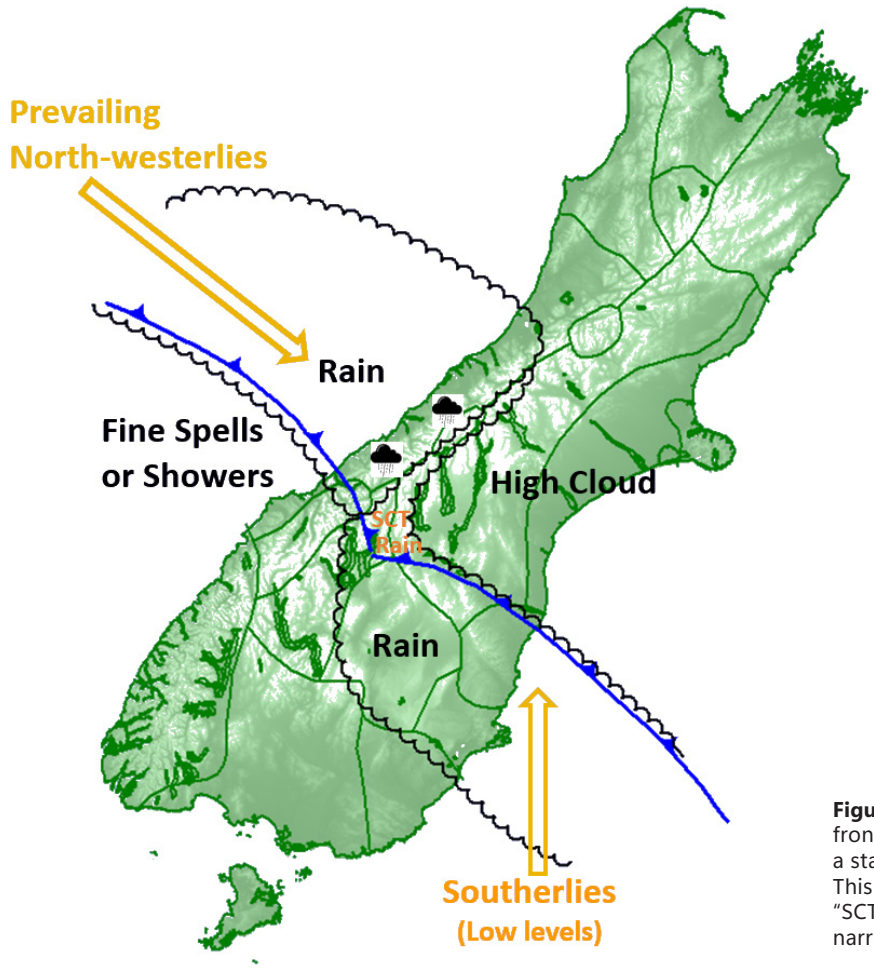

Figure 2: Weather pattern of a cold front moving up the South Island in a statically stable northwesterly flow. This is the most common situation. The "SCT Rain" region parallel to the Alps is narrow in stable flows.

radars are on opposite sides of the Southern Alps and are 140km apart. The Westland radar is a Vaisala WRM200 dual polarisation C-band Doppler radar. It is located 8km east of Hokitika at a height of 350m above Mean Sea Level (MSL). The Canterbury radar is an older Ericsson single polarisation C-band Doppler radar, located near Rakaia on the Canterbury Plains at a height of 124m above MSL. Both radars produce three-dimensional scans out to 250 km range every 7.5 minutes. The scans contain 13 elevation angles from 0.5° to 20.0°, with a range bin spacing of 200m at Westland and 125m at Canterbury.

2.3 Lightning

Lightning data come from the NZ Lightning Detection Network (LDN). The LDN consists of 10 Vaisala LS7002 sensors, of which 5 are located in the North Island and 5 in the South Island. The network is a hybrid system that uses both Time of Arrival and Magnetic Direction Finding to locate and classify lightning. The detection Efficiency of the network is modelled to be 95% for Cloud-to-Ground and 50% for Cloud-to-Cloud (including IntraCloud). For the majority of mainland NZ, the Location Accuracy of each flash is within 1km with a 50% confidence interval.

3. EVENT DESCRIPTION AND ANALYSIS

In early December of 2019, a week-long period of heavy rain affected the South Island (NZ Historic Weather Events Catalogue, NIWA). Rain fell over the Canterbury headwaters from 1 to 4 December, which pre-conditioned the Rangitata River to flood. There was considerable instability in the Tasman Sea and NZ region.

The storm of 6 to 7 December was the climax of the prolonged event. This coincided with widespread bushfires over eastern Australia from which significant amounts of smoke were blown across the Tasman Sea onto NZ. 101,202 lightning strikes were recorded from 0000UTC

6 to 0000UTC 7 December, which was twice the previous 24-hour record number of strikes (10 April 2018, based on the NZ lightning strike data since 2001). In Westland, 200 to 350mm of rain fell in 24 hours on the ranges but much less near the coast. Heavy rain led to landslides and flooding on the West Coast, cutting off towns and trapping about 1000 tourists. In Canterbury, 200 to 350mm of rain fell in 24 hours about the headwaters of the Canterbury rivers and lakes within 30km east of the main divide of the Southern Alps while, further east, significant but lesser falls were recorded. As context, warnings are issued when more than 50mm of rain in 6 hours or 100mm in 24 hours is expected over a wide area. In the Timaru District, a State of Emergency was declared on the morning of 7 December after the Rangitata River burst its banks downstream (Figure 3), and the only two bridges north to Christchurch were closed due to flooding.

On 8 December, thunderstorms and heavy rain battered the lower North Island. Nationwide, the storm cost insurers $15.29M but no deaths were reported.

Mean Sea Level Pressure (MSLP) map analyses (Figure 4) indicate a deep low to the south of the Tasman Sea, which brought troughs and fronts onto the South Island. The flow was cyclonic over the Tasman Sea and South Island. The troughs and fronts became slow-moving over the South Island due to a nearly stationary ridge of high pressure to the northeast of NZ.

Figure 5 shows the meteorological set-up, including the

Figure 3: The Rangitata River burst its banks on the morning of 7 December 2019 (Photo: Bejon Haswell / stuff.co.nz).

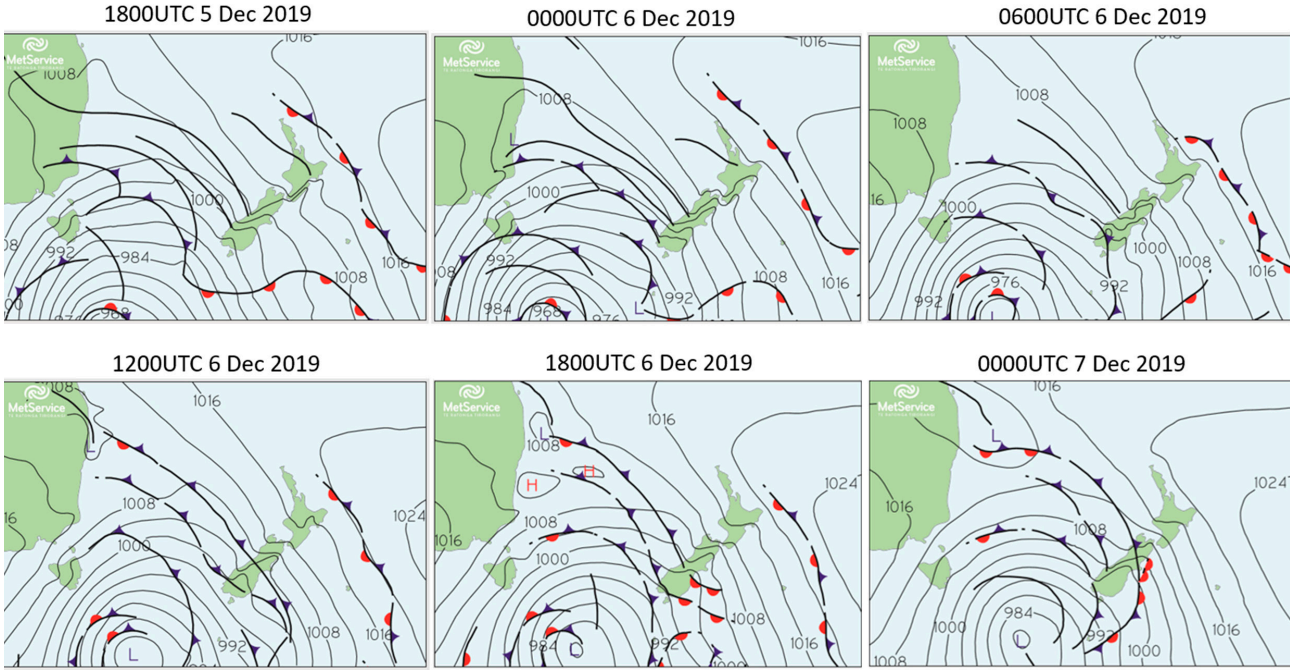

Figure 4: MSLP analyses from 1800UTC 5 December to 0000UTC 7 December 2019.

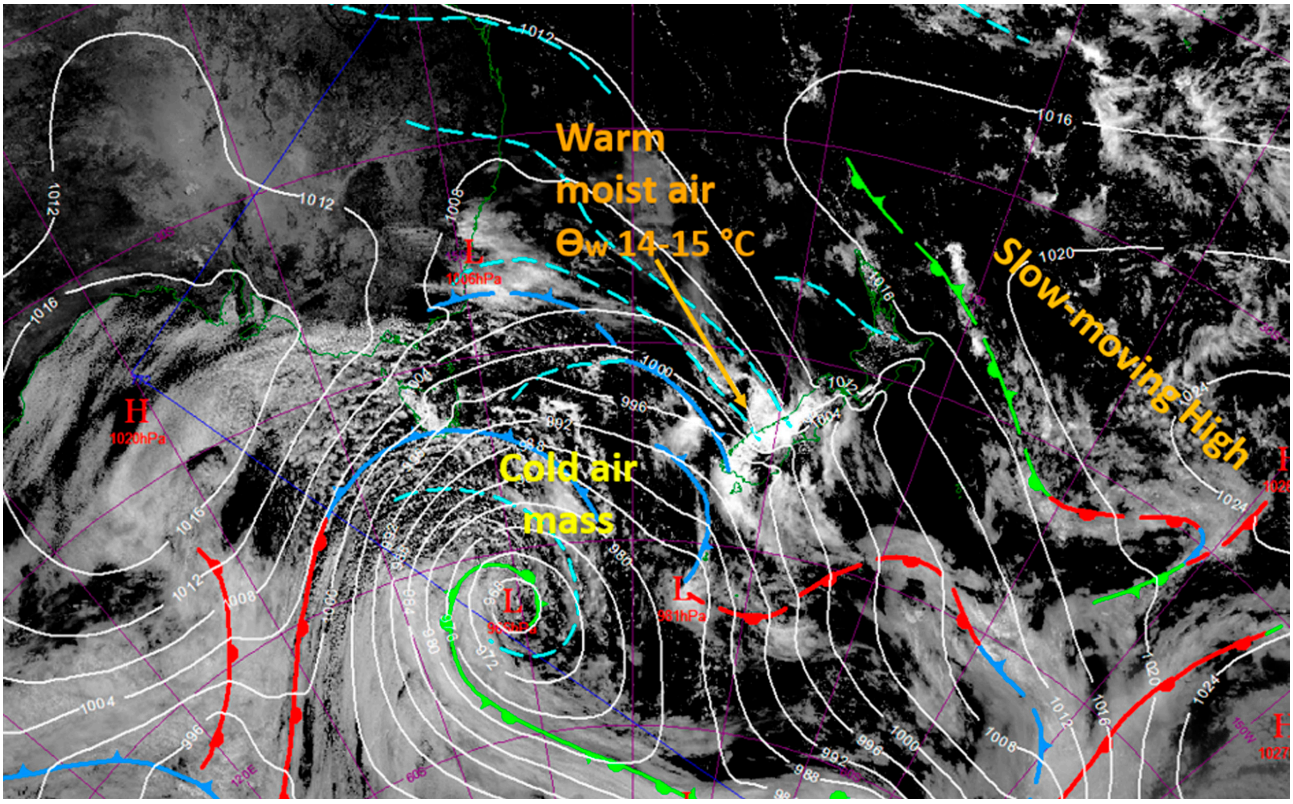

Figure 5: MSLP analysis superimposed on visible satellite image at 0000UTC 6 December 2019. Image courtesy JMA.

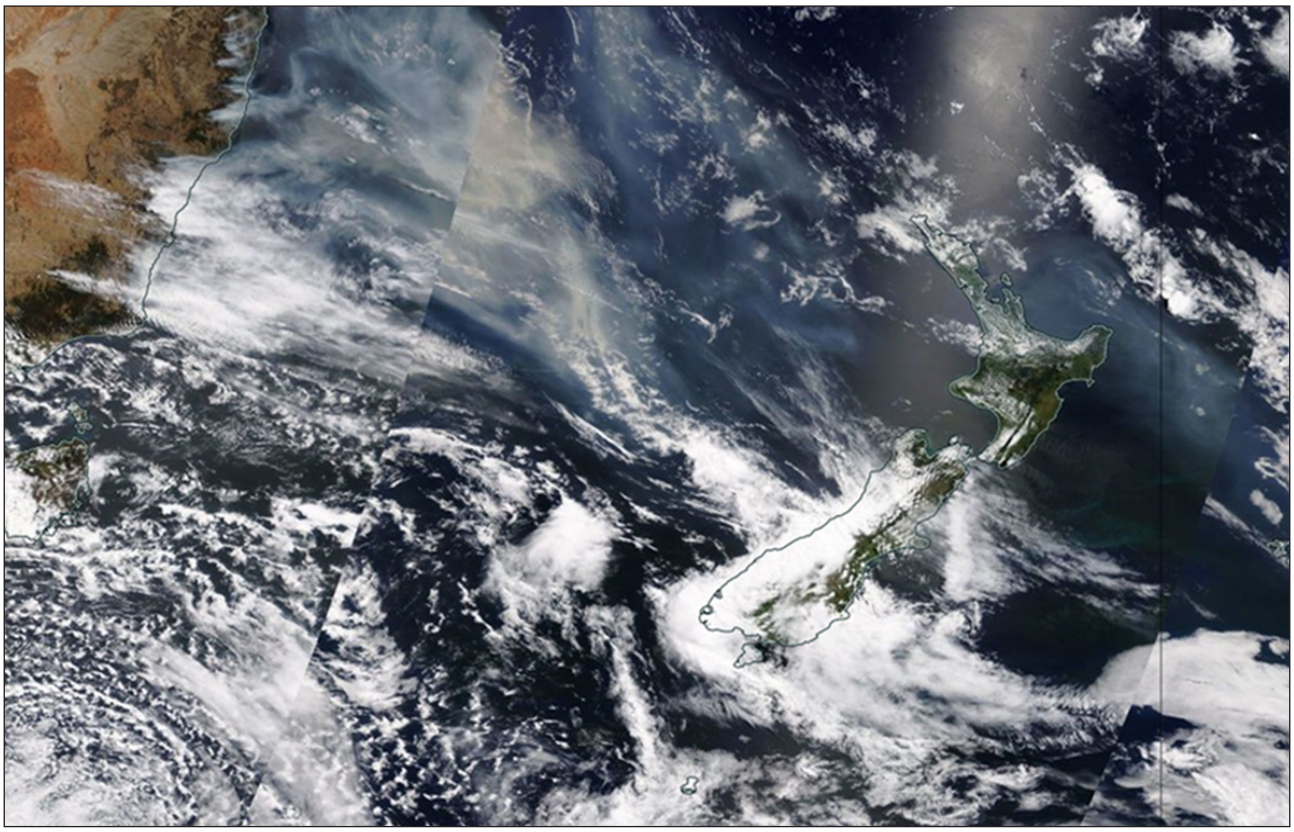

Figure 6: Terra MODIS Corrected Reflectance (True Colour) image at 2250UTC 5 December 2019 showing bushfires over eastern Australia with smoke particles (brown) extending over the Tasman Sea near and north of a front on the South Island West Coast. Note, a bright area to the north of the North Island was sun-glint. Image courtesy NASA.

moist northwesterly airstream extending from Australia onto NZ. Rain over the South Island was supported by an upper-level jet and bands of cyclonic vorticity advection at the 500hPa level (not shown), and cold advection from the south Tasman Sea. Figure 6 shows smoke particles from eastern Australian bushfires being blown across the Tasman Sea and becoming caught up in the fronts and troughs over NZ.

The lightning data in Figure 7 indicate a significant number of lightning strikes spread southeast to the Canterbury coast. Frequent lightning lasted for over 12 hours (0500-1900UTC 6 December) in South Canterbury where an eyewitness confirmed that he "had never seen this in the last 30 years" (personal communication: Laurence Smith, Environment Canterbury, 10/12/2019). The 24-hour rainfall accumulation plot (Figure 8a), valid to 9am 7 December, shows heavy rain spread east to the Canterbury High Country. The heaviest falls occurred about the headwaters of the Rangitata River, and significant rain fell further east into South Canterbury (Figure 8b).

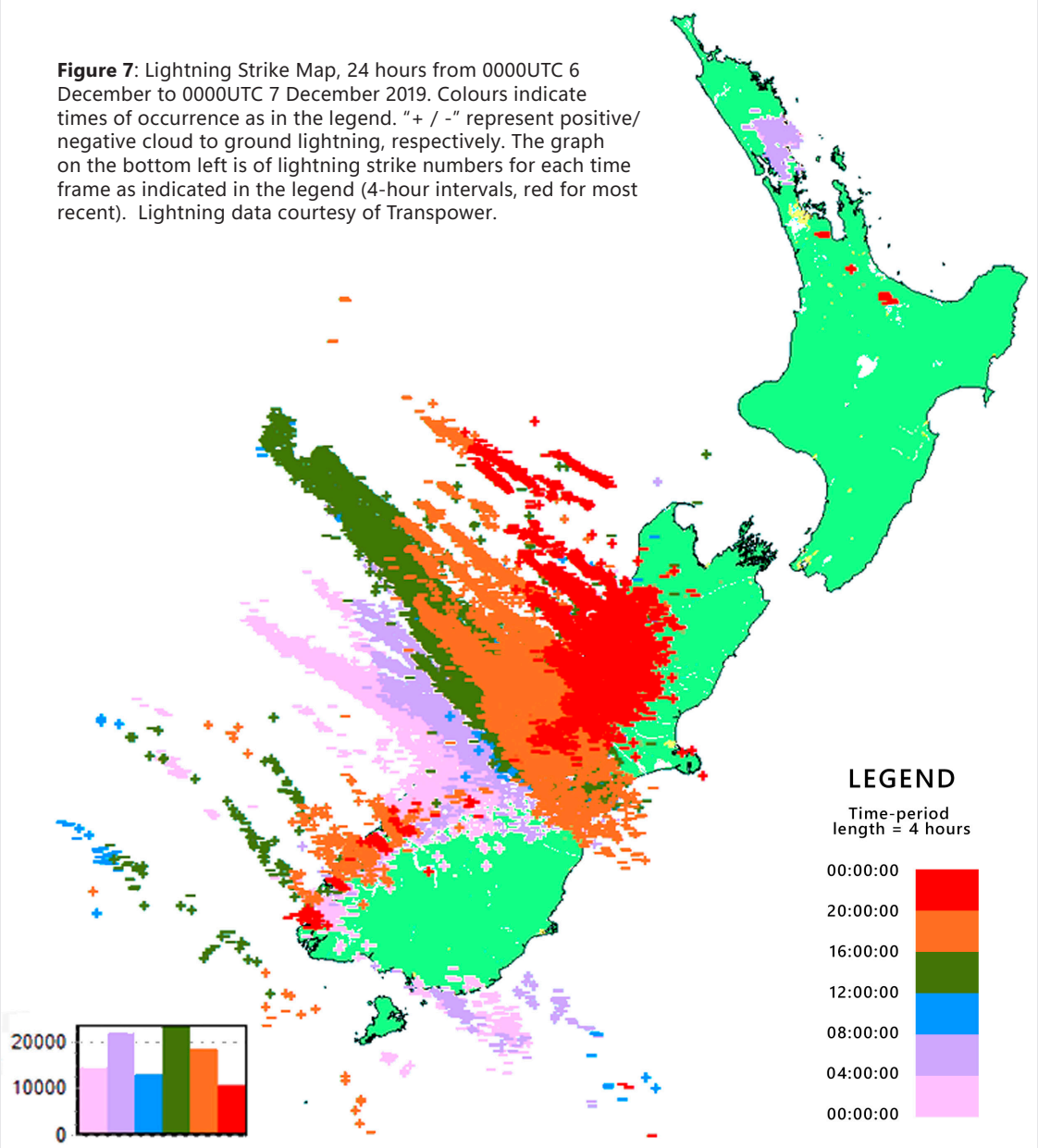

Figure 7: Lightning Strike Map, 24 hours from 0000UTC 6 December to 0000UTC 7 December 2019. Colours indicate times of occurrence as in the legend. "+ / -" represent positive/ negative cloud to ground lightning, respectively. The graph on the bottom left is of lightning strike numbers for each time frame as indicated in the legend (4-hour intervals, red for most recent). Lightning data courtesy of Transpower.

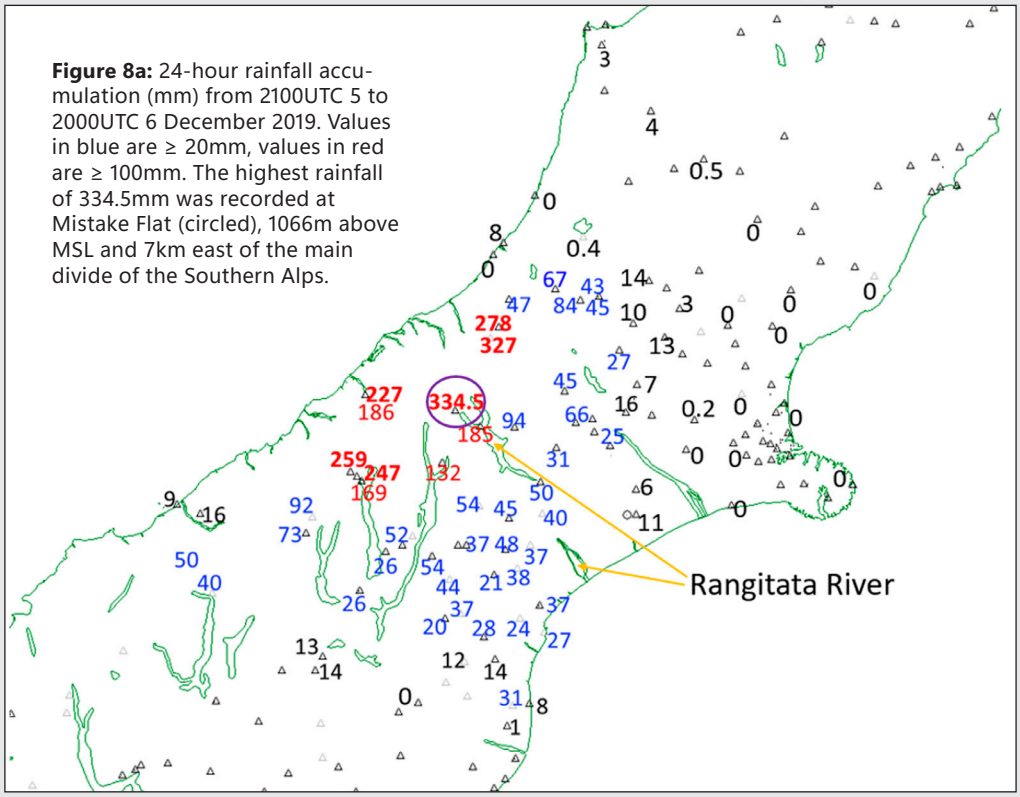

Figure 8a: 24-hour rainfall accumulation (mm) from 2100UTC 5 to 2000UTC 6 December 2019. Values in blue are ≥ 20mm, values in red are ≥ 100mm. The highest rainfall of 334.5mm was recorded at Mistake Flat (circled), 1066m above MSL and 7km east of the main divide of the Southern Alps.

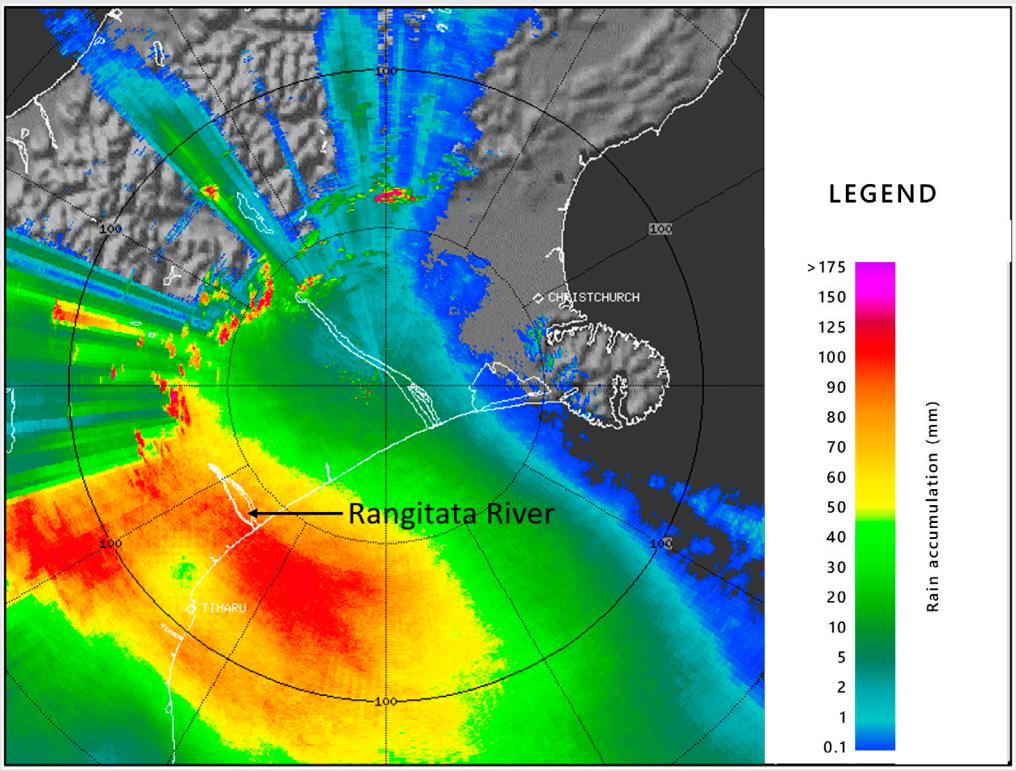

Figure 8b: Canterbury radar 24-hour gauge-corrected rainfall accumulation from 2100UTC 5 to 2000UTC 6 December 2019. This figure shows a rainfall maximum about and to the southeast of the Rangitata River mouth.

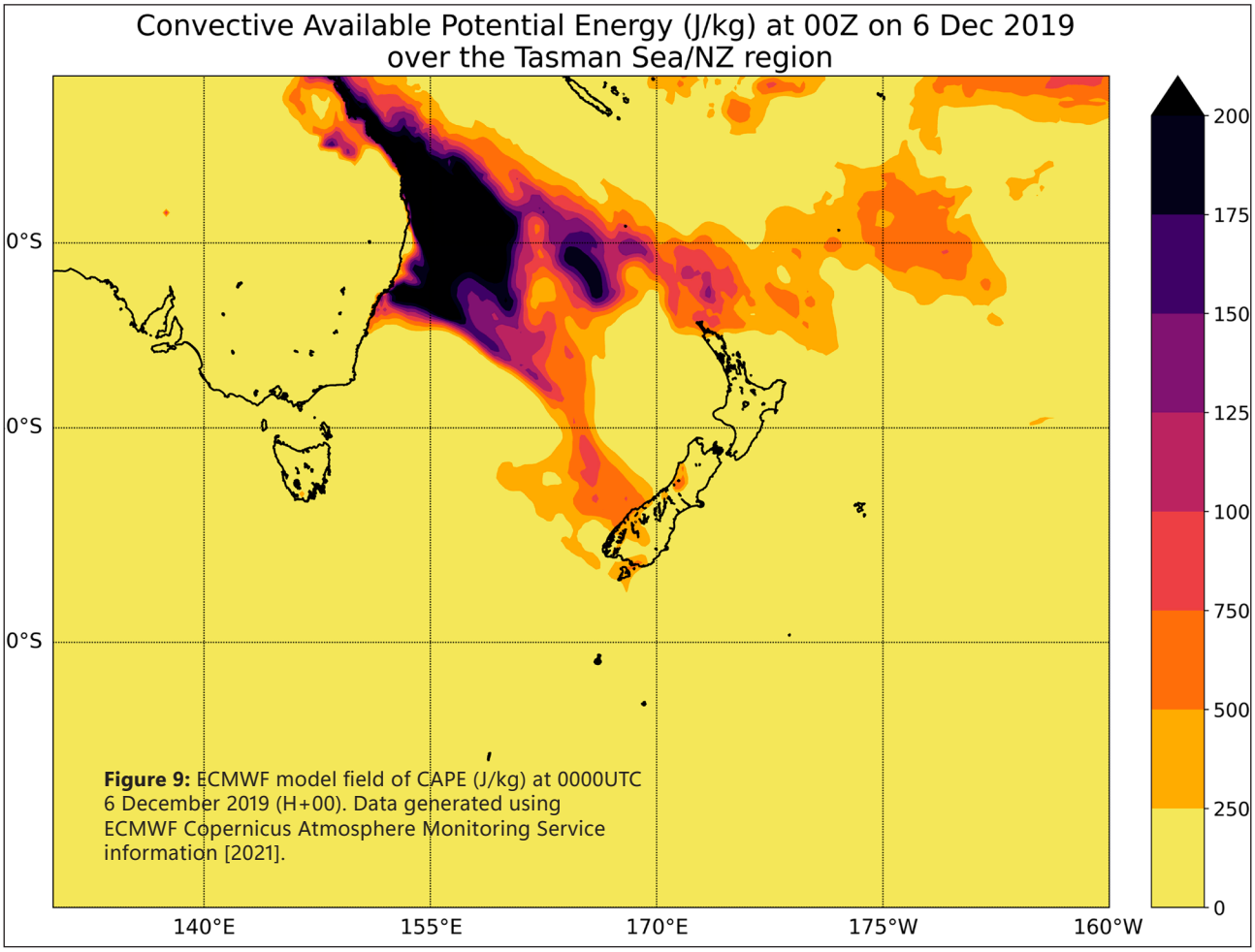

Figure 9: ECMWF model field of CAPE (J/kg) at 0000UTC 6 December 2019 (H+00). Data generated using ECMWF Copernicus Atmosphere Monitoring Service information [2021].

4. FINDINGS AND DISCUSSION

4.1 Event diagnosis

Modelled Convective Available Potential Energy (CAPE) in Figure 9 indicates substantial instability over the Tasman Sea. Significant CAPE (500-750J/kg) and Normalised Total-Totals[1] (NTT, 52.5-60) on the west of the South Island ahead of the front indicated that static instability was an important factor in generating the active lightning. Precipitable Water Vapour (PWV) was 25-30mm on 6 December and increased to 30-35mm the following morning.

Weather Research and Forecasting (WRF- GFS) model tephigrams (Figure 10) confirmed a deep, unstable airmass on the West Coast from the morning of 6 December to the morning of 7 December.

They indicated a buoyant and generally moist (but dry in the middle level at 1200UTC 6 December) airmass ahead of the slow-moving front, and northwesterly winds increasing with height and becoming very strong above mountain-top level. The strong winds favoured the propagation of hydrometeors and convective cells, as the windshear aloft was not so strong as to destroy convection. Winds perpendicular to the Southern Alps increased the orographic enhancement of rain and triggered thunderstorms over the ranges. Figure 10 indicates strong upward motion from low levels up to 300hPa in the hours before the Rangitata River burst its banks. The upward motion was -83 x 10^{-3} to -220 x 10^{-3}hPas^{-1} between 900hPa and 700hPa, and -250 x 10^{-3} to -330 x 10^{-3}hPas^{-1} between 700hPa and 500hPa at 1800UTC 6 December above the central Westland coast. Such values are extremely large for NZ. This set-up drove heavy rain and thunderstorms from the western slopes of the Southern Alps across to east of the Alps.

1 NTT (Normalised Total-Totals) calibrates the commonly used TT (Total -Totals) atmospheric stability index to correct for airmass dependence. Warm moist atmospheres that are unstable can yield TT values below 50, while cold dry atmospheres with the same overall stability might have values in excess of 60. The NTT normalises all atmospheres such that a value of 50 equates to neutral stability (with values above this indicating deep instability), no matter the location or season (Schwarz, 2004).

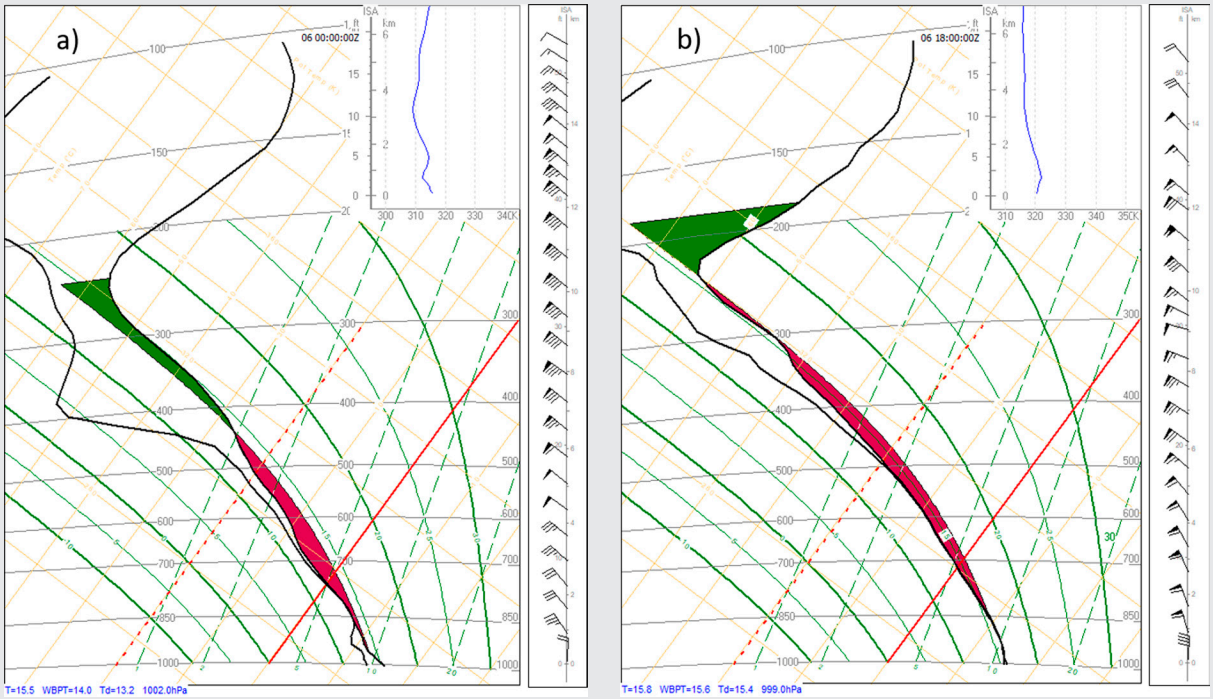

Figure 10: NZ4km WRF – GFS model tephigrams (H+00) for the central Westland coast at 0000UTC (left), and 1800UTC (right) 6 December 2019. Yellow lines orientated from top-right to bottom-left are isotherms; yellow lines from top-left to bottom-right are dry adiabats; solid dark-green curves are saturated adiabats. The red shaded area represents CAPE. Wind barbs (right) indicate direction with a full barb =10 knots, half barb = 5 knots, and solid triangle barb =50 knots. Inset at the top right is the equivalent potential temperature (K).

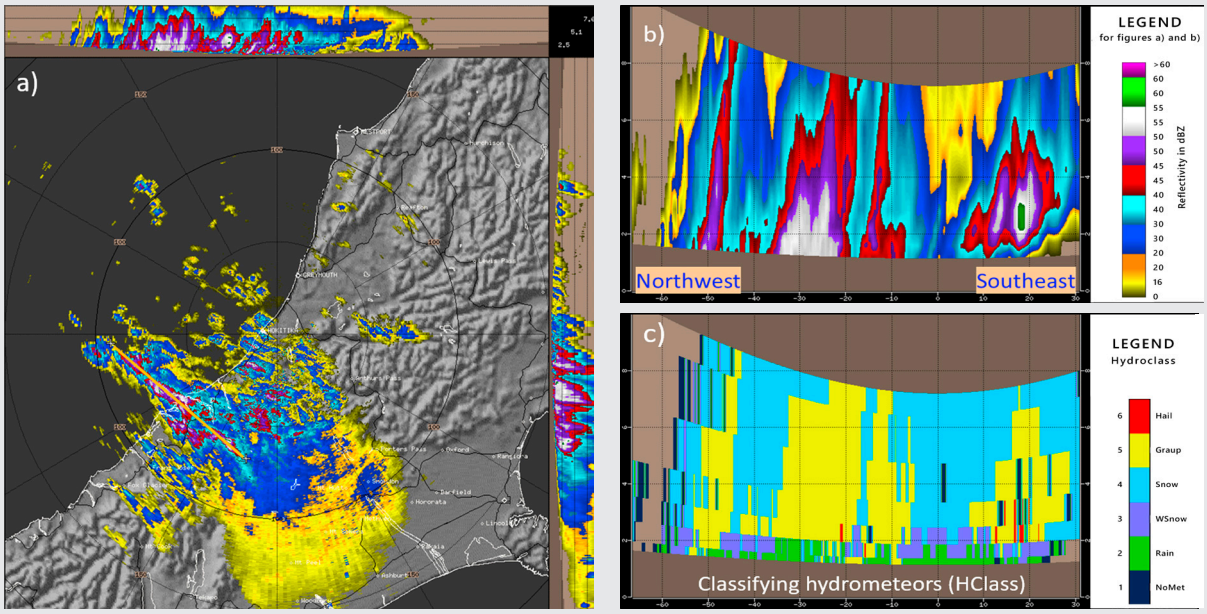

Figure 11: a) Westland radar Maximum Reflectivity, **b)** reflectivity cross-section, and **c)** HClass cross-section at 12:52UTC 6 December 2019. In a), the main image is maximum reflectivity in the vertical from all available radar beams; top panel is maximum reflectivity from north to south, plotted with respect to height (km); right panel is maximum reflectivity from east to west, also plotted with respect to height (km). The b) and c) cross-sections are taken along the orange line segment in a). Figure b) indicates approximate rainfall intensity: yellow = light precipitation, blue = moderate precipitation, purple/white = heavy precipitation or graupel. Figure c) is the hydrometeor class of b), where green = rain, purple = wet snow, blue = snow, yellow = graupel, red = hail.

4.2 Radar signatures

The Maximum Reflectivity composite data of the Westland and Canterbury Radars from 0000UTC to 1800UTC 6 December indicate that strong radar echoes moved onto South Canterbury. Figure 11a shows deep convective cells on the West Coast, tilting eastwards with height due to the wind profile. Figure 11b indicates very strong echoes to mid-high levels. Figure 11c shows extensive graupel (yellow) and some hail (red) within the convective cells. Graupel is being detected at more than 8km above the surface.

Figure 12a shows thunderstorms to the west of the Southern Alps, decaying thunderstorms just east of the main divide, and stratiform precipitation further east. Radar data before and after this time (not shown) indicated similar characteristics.

The inset in Figure 12b is a cross-section from the Canterbury radar along a line from South Canterbury to the Canterbury Bight showing enhanced radar reflectivity (dBZ) associated with aggregated or rimed snowflakes in falling snow (the mechanism explained in Figure 14, Ryan et al., 1976), and a radar bright-band associated with rain falling from melting snow below the freezing level. The weaker yellow radar reflectivities are associated with smaller ice crystals blown over the main divide from the west, while the darker blue reflectivities are likely from aggregated snowflakes and/or larger rimed crystals. The cross-section shows enhanced radar reflectivity associated with falling snow about the coast of South Canterbury (ahead of the front). Radar reflectivity time stamps in Figure 13 indicate stronger radar reflectivities (30 - 40dBZ) near the Rangitata River mouth. Tephigrams from WRF (Figure 14) show the upward motion in an upper layer from 380hPa to 200hPa, suggesting the precipitation about the coast of South Canterbury was likely associated with ascent in a quasi-stationary leeward mountain wave (Figure 15).

4.3 Eastward spread of thunderstorms and lightning

Aerosols such as smoke particles can enhance lightning activity through modifying cloud microphysical properties and invigorating convection (Yuan et al., 2011; Shi et al., 2020). They can also enhance spillover precipitation in a moist environment through riming and Wegener–Bergeron–Findeisen processes (Choudhury et al., 2019). The numerous smoke particles that originated from the Australian bushfires would have provided abundant cloud condensation nuclei (CCN) and ice nuclei, compared to the natural particulate environment dominated by salt CCN in NZ. This would have resulted in the cloud water being distributed into a larger number of smaller ice crystals at high altitudes (likely at the expense of saturated cloud liquid water).

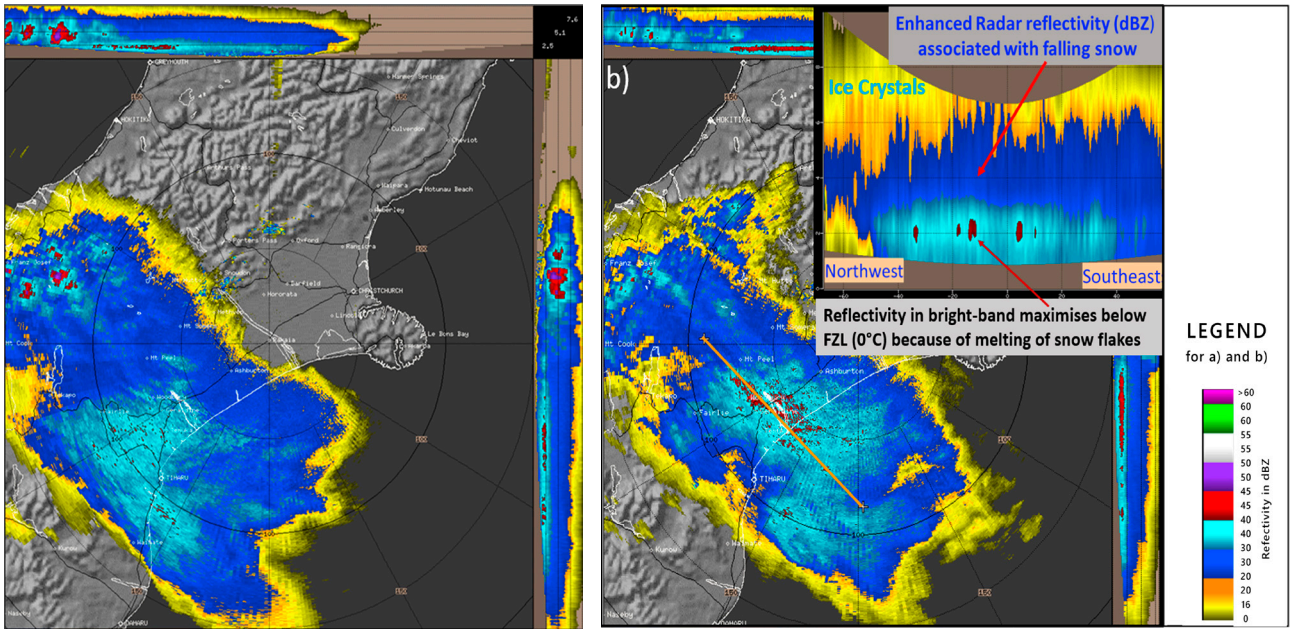

Figure 12: a) Canterbury radar Maximum Reflectivity at 06:07UTC and **b)** Maximum Reflectivity and cross-section of Canterbury radar (inset) at 07:00UTC 6 December 2019. The cross-section is taken along the orange line segment in the bottom right image. The times were chosen to match the satellite images in Figure 15 b) and c), respectively.

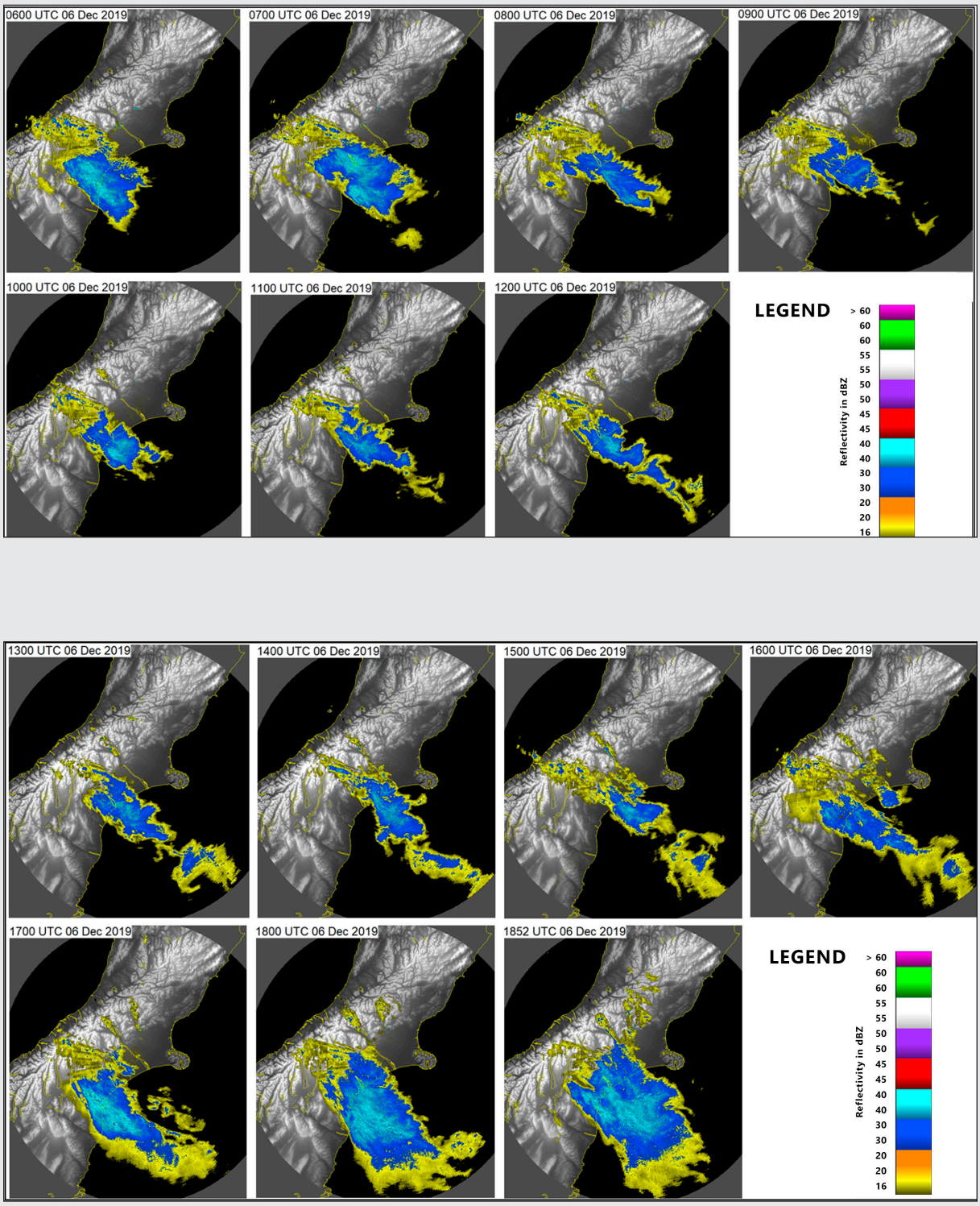

Figure 13: Canterbury radar Reflectivity time stamps in dBZ (decluttered, PPI and Elevation 0.5°) top: from 0600UTC to 1200UTC 6 December, bottom: from 1300UTC to 1852UTC 6 December 2019.

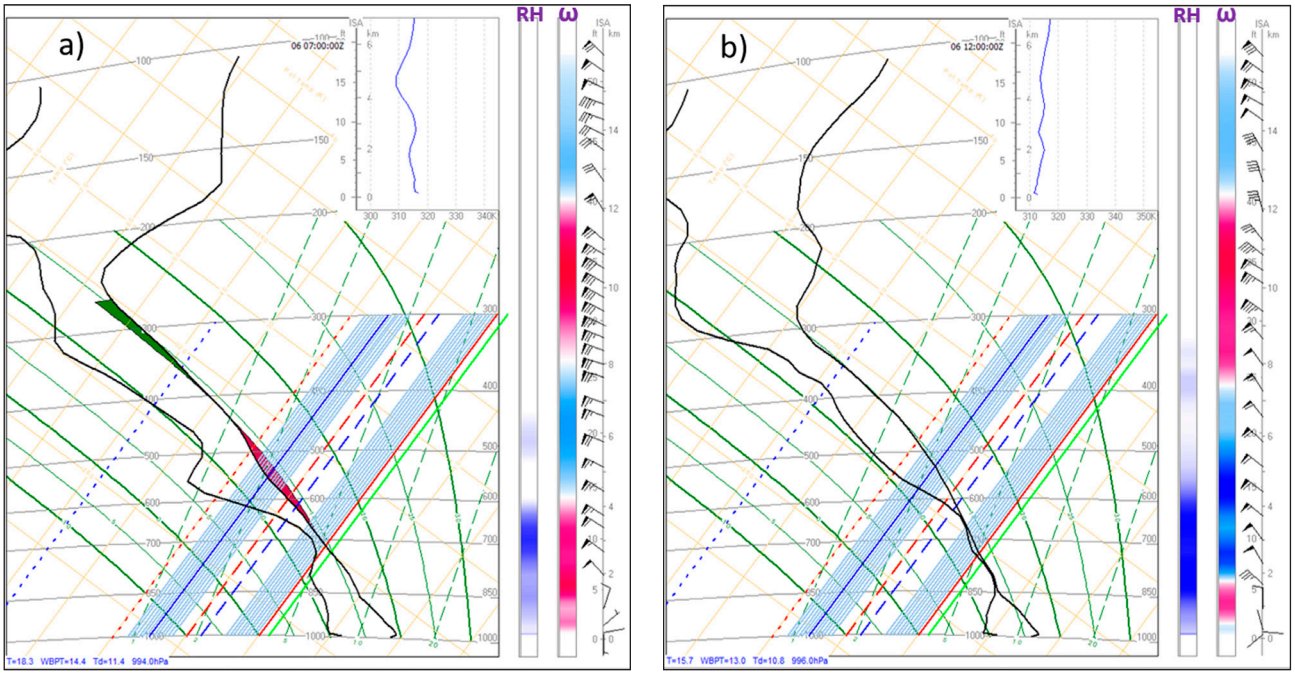

Figure 14: NZ4km WRF-GFS model tephigrams for Timaru (near the coast just south of Rangitata River mouth), **a)** 0700UTC 6 December 2019, and **b)** 1200UTC 6 December 2019. See Figure 10 for explanation of key lines on the tephigram. In addition, blue lines orientated from upper-right to bottom-left are snow production temperatures (solid red line is zero-degree line). There are two coloured vertical bars along the y-axis, relative humidity (light blue to dark blue representing RH from 50% to 100%) on the left, and Omega (vertical motion ω) on the right (red representing upward motion and blue representing downward motion). Both a) and b) show that temperature and dewpoint temperature separated when colder than -8°C; the airmass was humid between -4°C and 0°C at 0700UTC 6 December, and was near-saturated in a layer between -8°C and +1°C at 1200UTC 6 December 2019. This means ice crystals grew by aggregation and accretion (including riming).

REGION	WESTLAND			CANTERBURY HIGH COUNTRY			CANTERBURY PLAINS (incl. Christchurch)		
NUMBER OF STRIKES PER REGION	20,006			23,272			419		
NUMBER OF STRIKES BY TYPE	CG -	CG +	CC	CG -	CG +	CC	CG -	CG +	CC
	13,085	2,855	4,066	14,510	2,495	6,267	186	128	105
PROPORTION OF STRIKES PER REGION TO TOTAL NUMBER OF STRIKES ACROSS ALL THREE REGIONS (%)	45.8			53.3			0.9		

Table 1: 24-hour (0000 - 2359UTC 6 December 2019) lightning strike data in Westland and Canterbury High Country and Canterbury Plains. "CC" means Cloud-to-Cloud (including Intra-Cloud) lightning, "CG -" means negative Cloud to Ground lightning, and "CG +" means positive Cloud to Ground lightning.

Table 1 shows that the number of lightning strikes in the Canterbury High Country was significantly greater than in Westland.

Figure 11c indicated abundant graupel to high levels in convective clouds to the west of the Southern Alps (upstream). The process of graupel (or hail) formation is associated with strong cloud electrification, causing more intense thunderstorms (Andreae et al., 2004). Most of the hailstones (graupel) melted as they fell below a high freezing level (2700m), so they arrived at the surface as bursts of heavy rain. This is evident in the radar HydroClass cross-section which (Figure 11c) shows rain (coloured green) as the predominant hydrometeor class at the low levels within the convective cells. Radar imagery (Figure 12a) shows no

convective cells in South Canterbury (not only at this time stamp but also through the 24-hour period), so observed lightning there (from 0500-1900UTC 6 December) was likely due to spillover of charged snow/ice crystals at high altitudes rather than deep convective cells. Strong cross-mountain winds and an unstable airmass (Figure 10) brought abundant charged snow/ice across the Alps onto Canterbury, increasing spillover rain. This process, along with decaying convective cells just east of the main divide, resulted in the maximum rainfall distribution shifting eastward, and warning amounts of rain within 30km east of the main divide. This is consistent with the highest 24-hour rainfall being recorded at Mistake Flat (Figure 8a).

On 6 - 7 December, there was no broad raincloud extending across the Tasman Sea to NZ. However, from the afternoon of 6 December, there was a line of deep convection over the eastern Tasman Sea and Westland, and convective cells that moved across the Southern Alps (Figure 15). An upper "anvil cloud" from cumulonimbus extended towards the Canterbury Bight. The Infrared image (Figure 15c) indicated an area of high cloud tops near the Canterbury coast (green) just to the south of the Rangitata River mouth, coinciding with a secondary rainfall maximum (Figure 8b). This suggests lee-wave enhancement triggered by the Southern Alps.

Lightning was active from 1300UTC to 1900UTC on

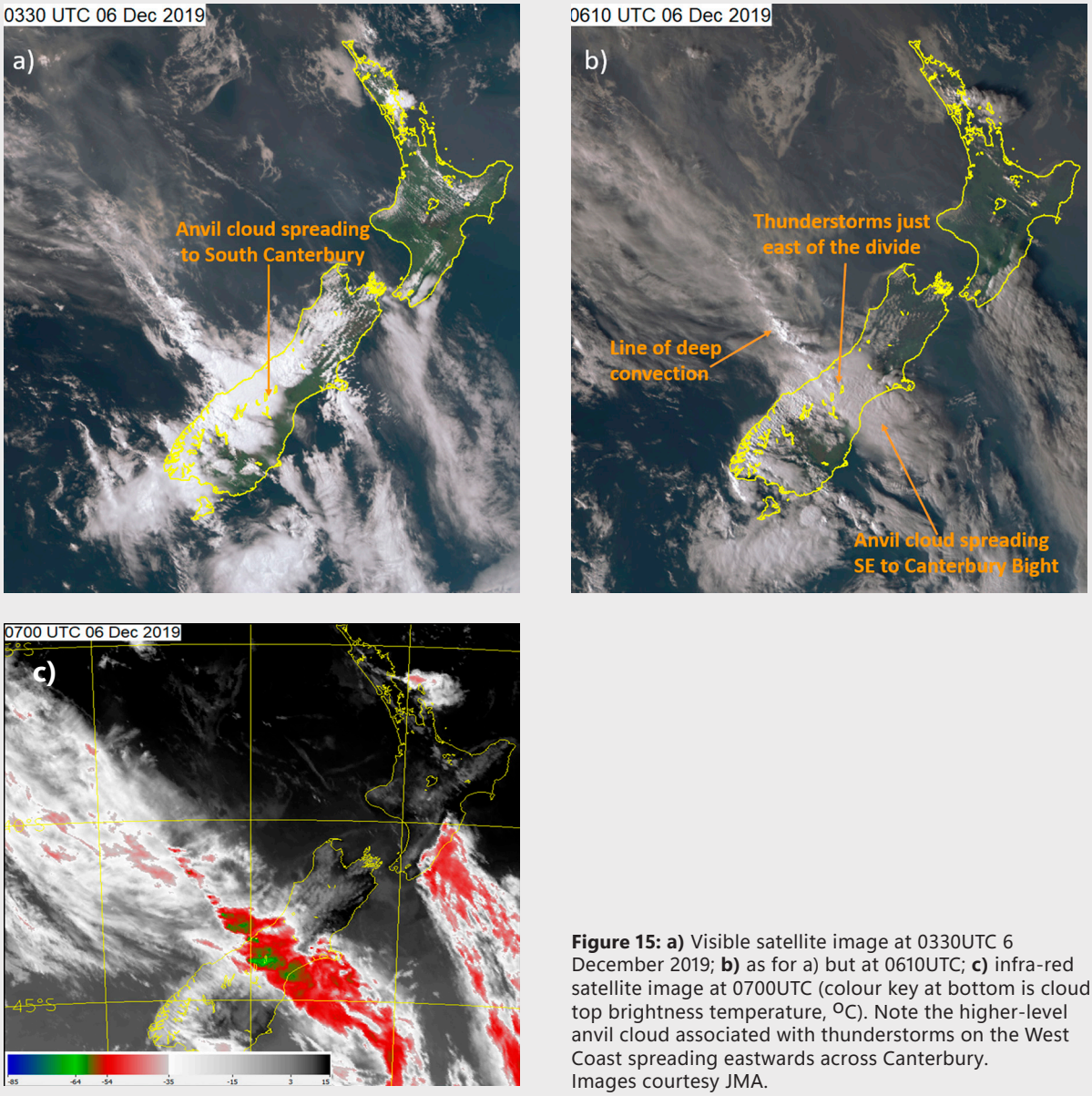

Figure 15: a) Visible satellite image at 0330UTC 6 December 2019; **b)** as for a) but at 0610UTC; **c)** infra-red satellite image at 0700UTC (colour key at bottom is cloud-top brightness temperature, ^{o}C). Note the higher-level anvil cloud associated with thunderstorms on the West Coast spreading eastwards across Canterbury. Images courtesy JMA.

6 December when spillover rain was heaviest. Lines of lightning strikes extended from the Tasman Sea onto the West Coast, and the strike density increased on the windward slopes and across the Southern Alps. Lightning then spread southeast to the Canterbury Bight, and most strikes that occurred from the Canterbury foothills to the Bight were Cloud-to-Ground, with one-third positively charged. There was no clear evidence that the wave enhancement increased lightning strikes in South Canterbury.

It is proposed that lightning spread to the Canterbury coast due to the discharge of charged ice crystals from anvil cloud and mid to low-level convective cloud further west, rather than due to deep convection spreading off the Southern Alps. This process lasted for an extended period because the frontal system was slow-moving, the airmass was unstable and the winds across the mountain ridge were strong.

4.4 A conceptual model of enhanced spillover rain with smoke particles in an unstable northwest flow

Figure 16 is a schematic diagram of convective cells about the Southern Alps, spillover rain further east, and significant snow/ice crystals that became electrically charged due to embedded smoke particles. The diagram also shows mountain wave cloud over eastern Canterbury that likely enhanced dendritic growth aloft, resulting in significant rain falling over South Canterbury in a region that would otherwise be dry.

5. CONCLUSIONS

The December 2019 storm occurred in a particularly unstable environment and involved smoke particles from Australian bushfires. The airmass had very large NTT (52.5-60) and CAPE (500-750J/kg), and strong upper divergence. The storm was slowed by a nearly stationary high-pressure system to the northeast of NZ. It had strong northwesterlies (but weak windshear) over the Southern Alps, and weak cold advection aloft. Extreme upward motion (-250 x 10^{-3} to -330 x 10^{-3}hPas^{-1} between 700 and 500hPa) occurred on the Westland coast ahead of the front.

The storm brought warning amounts of heavy rain to 30km east of the main divide of the Southern Alps, significantly further east than in most EWEs. The maximum 24-hour rainfall shifted to about or just east of the main divide. The storm produced a new 24-hour lightning strike record (101,202) and extensive lightning across the Southern Alps and into South Canterbury. Lightning spreading to the Canterbury coast was likely due to the discharge of charged ice crystals from anvil cloud and mid to low-level convective cloud further west, rather than due to deep convection spreading off the Southern Alps. A secondary rainfall maximum was found on the South Canterbury coast under a quasi-stationary leeward mountain wave.

Smoke particles likely played a role in the spillover and lightning. Without the effect of the smoke particles,

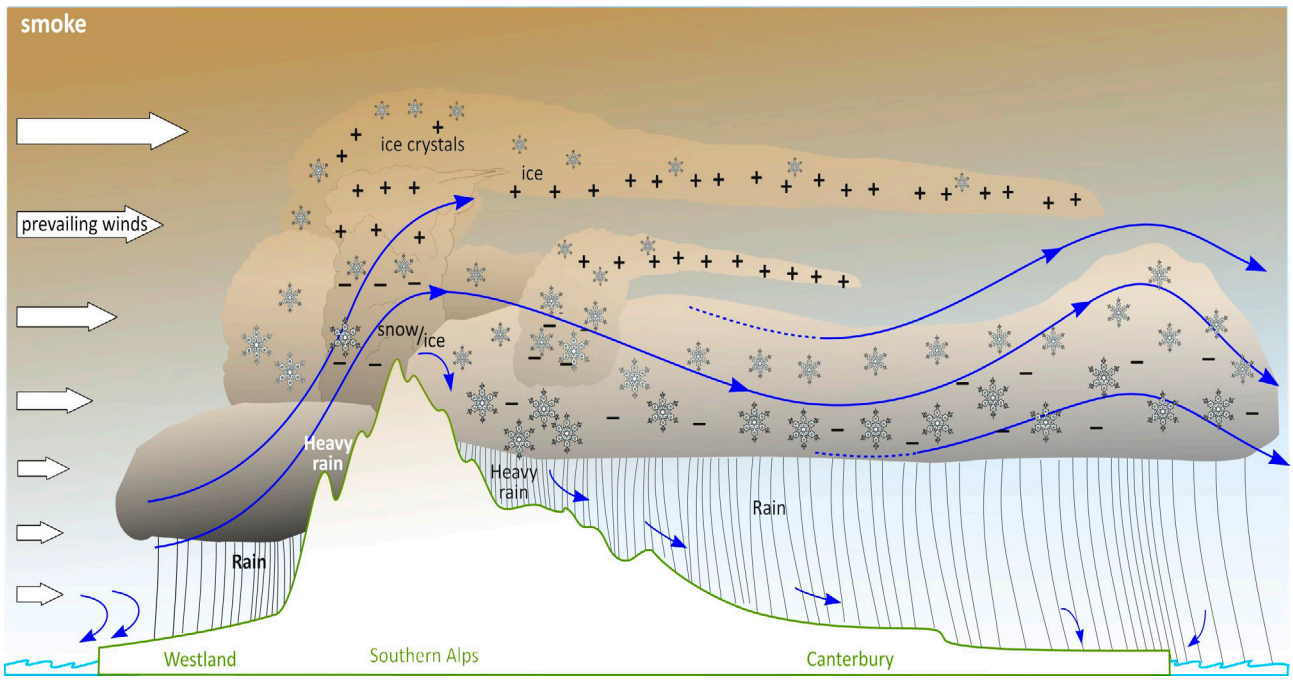

Figure 16: A conceptual model for the 6-7 December 2019 storm.

the number of nuclei would have been much reduced; it is highly likely that thunderstorms to the west of the Southern Alps would have been less active. Rain in South Canterbury ahead of the front would have been lighter and confined to further west. Lightning strikes would similarly have been displaced westwards or much reduced as they spread east across Canterbury.

Due to climate change, spillover heavy rain events could occur more frequently (IPCC, 2022) and may well involve smoke from Australian bushfires. If smoke particles interact with a frontal system, meteorologists should consider the increased potential for heavy spillover rain. This is in terms of both rainfall accumulation and the eastward extent of spillover.

Further research is needed on cases using aerosol concentration data, including the aerosol optical depth (Dayeh et al., 2021; Grell et al., 2011). This should include a mesoscale model coupled with atmospheric chemistry to perform simulations with and without smoke particles in EWEs. This could investigate whether, or under which situations, the smoke particles cause a shift and /or intensification of spillover heavy rain and thunderstorm activity across the Southern Alps of NZ. Other work could look into the effect of varying the number of CCN in mesoscale models and evaluating model performance when smoke particles are present.

ACKNOWLEDGEMENTS

The authors thank John Crouch, MetService severe weather meteorologist, for his contributions to sections 2.2, 2.3 and 4.2, and Figure 16; Allister Gorman, MetService severe weather meteorologist, for providing lightning strike statistical data; Mark Schwarz, MetService senior consultant meteorologist, for his comments and suggestions, and MetService Forecasting Research and Development team scientists Sijin Zhang for providing information on WRF implementation and Sapna Rana for drafting Figure 9; Leigh Matheson, MetService severe weather meteorologist, for her suggestions; and Chris Knoche, MetService system engineer, for providing lightning data.

REFERENCES

Andreae, M.O., Rosenfeld, D., Artaxo, P., Costa, A.A., Frank, G.P., Longo, K.M. and Silva-Dias, M.D., 2004. Smoking rain clouds over the Amazon. *Science*, 303(5662), pp.1337-1342.

Browning, K.A., Hill, F.F. and Pardoe, C.W., 1974. Structure and mechanism of precipitation and the effect of orography in a wintertime warm sector. *Quarterly Journal of the Royal Meteorological Society*, 100(425), pp.309-330.

Chater, A.M., Sturman, A.P., 1998. Atmospheric conditions influencing the spillover of rainfall to lee of the Southern Alps, NZ. *International Journal of Climatology: A Journal of the Royal Meteorological Society*, 18(1), pp.77-92.

Choudhury, G., Tyagi, B., Singh, J., Sarangi, C. and Tripathi, S.N., 2019. Aerosol-orography-precipitation–A critical assessment. *Atmospheric Environment*, 214, p.116831.

Collier, C.G., 1975. A representation of the effects of topography on surface rainfall within moving baroclinic disturbances. *Quarterly Journal of the Royal Meteorological Society*, 101(429), pp.407-422.

Dayeh, M.A., Farahat, A., Ismail-Aldayeh, H. and Abuelgasim, A., 2021. Effects of aerosols on lightning activity over the Arabian Peninsula. *Atmospheric Research*, 261, p.105723.

Grell, G., Freitas, S.R., Stuefer, M. and Fast, J., 2011. Inclusion of biomass burning in WRF-Chem: impact of wildfires on weather forecasts. *Atmospheric Chemistry and Physics*, 11(11), pp.5289-5303.

Henderson, R.D., 1993. Extreme storm rainfalls in the Southern Alps, New Zealand. *IAHS PUBLICATION*, pp.113-113.

IPCC, 2022: Climate Change 2022 - *Mitigation of Climate Change: The Intergovernmental Panel on Climate*, Skea J., Shukla P. R, Reisinger A., et al., https://report.ipcc.ch/ar6/wg3/IPCC_AR6_WGIII_Full_Report.pdf.

Kingston D.G., Lavers, D.A. and Hannah, D.M., 2016. Floods in the Southern Alps of NZ: the importance of atmospheric rivers. *Hydrological Processes*, 30(26): 5063–5070.

Little, K., Kingston, D.G., Cullen, N.J. and Gibson, P.B., 2019. The role of atmospheric rivers for extreme ablation and snowfall events in the Southern Alps of NZ. *Geophysical Research Letters*, 46(5), pp.2761-2771.

Marwitz, J.D., 1980. Winter storms over the San Juan Mountains. Part I: dynamical processes. *Journal of Applied Meteorology and Climatology*, 19(8), pp.913-926.

NIWA, December 2019 New Zealand Storm. *New Zealand Historic Weather Events Catalogue*. https://hwe.niwa.co.nz/event/December_2019_New_Zealand_Storm.

Reid, K.J., Rosier, S.M., Harrington, L.J., King, A.D. and Lane, T.P., 2021. Extreme rainfall in NZ and its association with Atmospheric Rivers. *Environmental Research Letters*, 16(4), p.044012.

Ryan, B.F., Wishart, E.R. and Shaw, D.E., 1976. The growth rates and densities of ice crystals between −3°C and −21°C. *Journal of Atmospheric Sciences*, 33(5), pp.842-850.

Schwarz M., 2004. NTT: Normalising the Total Totals Stability Index, Internal Memo of MetService, NZ (copy available on request to the authors).

Shi, Z., Wang, H., Tan, Y., Li, L. and Li, C., 2020. Influence of aerosols on lightning activities in central eastern parts of China. *Atmospheric Science Letters*, 21(2), p.e957.

Sinclair, M.R., Wratt, D.S., Henderson, R.D. and Gray, W.R., 1997. Factors affecting the distribution and spillover of precipitation in the Southern Alps of NZ—A case study. *Journal of Applied Meteorology*, 36(5), pp.428-442.

Singh, P., Ramasastri, K.S. and Kumar, N., 1995. Topographical influence on precipitation distribution in different ranges of western Himalayas. *Hydrology Research*, 26(4-5), pp.259-284.

Wratt, D.S., Ridley, R.N., Sinclair, M.R., Larsen, H., Thompson, S.M., Henderson, R., Austin, G.L., Bradley, S.G., Auer, A., Sturman, A.P. and Owens, I., 1996. The NZ southern alps experiment. *Bulletin of the American Meteorological Society*, 77(4), pp.683-692.

Wratt, D.S., Revell, M.J., Sinclair, M.R., Gray, W.R., Henderson, R.D. and Chater, A.M., 2000. Relationships between air mass properties and mesoscale rainfall in NZ's Southern Alps. *Atmospheric Research*, 52(4), pp.261-282.

Yuan, T., Remer, L.A., Pickering, K.E., and Yu, H., 2011. Observational evidence of aerosol enhancement of lightning activity and convective invigoration. *Geophysical Research Letters*, 38(4).

Coupled ocean-atmosphere summer heatwaves in the New Zealand region: an update

M James Salinger[1], Howard J Diamond[2], James Bell[3], Erik Behrens[4], B Blair Fitzharris[5], Nicholas Herod[6], Melissa McLuskie[7], Amber K Parker[8], Hiltrun Ratz[9], James Renwick[1], Claire Scofield[10], Nick T Shears[11], Robert O Smith[12], Phil J Sutton[4] and Michael C T Trought[13]

[1] Department of Geography, Environment and Earth Sciences, Victoria University of Wellington, Wellington, New Zealand
[2] NOAA/Air Resources Laboratory, College Park, Maryland 20740, USA
[3] School of Biological Sciences, Victoria University of Wellington, New Zealand
[4] National Institute of Water and Atmospheric Research (NIWA), Wellington, New Zealand
[5] Department of Geography, University of Otago, Dunedin, New Zealand
[6] Applied Science Pty Ltd., Adelaide, Australia
[7] Western Bay Wildlife Trust, Tauranga, New Zealand
[8] Department of Wine, Food and Molecular Biosciences, Lincoln University, New Zealand
[9] Penguin Rescue, Moeraki Lighthouse, RD2 Palmerston, Otago, New Zealand
[10] New Zealand Institute for Plant and Food Research Limited, New Zealand
[11] Leigh Marine Laboratory, Institute of Marine Science, University of Auckland, New Zealand
[12] Department of Marine Science, University of Otago, Dunedin, New Zealand
[13] Innovative Winegrowing, Blenheim, New Zealand
Corresponding author: M. James Salinger, jimbosalinger09@gmail.com

KEY WORDS
Anthropogenic global warming, marine heatwave, atmospheric heatwave, terrestrial ecosystems, marine ecosystems, grapes

ABSTRACT

During austral warm seasons (November - March, NDJFM) of 1934/35, 2017/18, 2018/19 and 2021/22 the New Zealand (NZ) region experienced the most intense coupled ocean/atmosphere (MHW/AHW) heatwaves on record. Average temperature anomalies over land and sea were +1.2 to 1.4°C above average. Common to all four events were maximum sea surface temperature (SST) anomalies to the west of the South Island of NZ. Atmospheric circulation anomalies showed a pattern of blocking high pressure over the Tasman Sea and Pacific Ocean to the south, and southeast of NZ, and reduced trough activity over and to the east of NZ, accompanied by strongly positive Southern Annular Mode conditions.

Hindcasts for 2017/18, 2018/19 and 2021/22 NDJFM indicate that positive temperature anomalies around 1°C occurred in the Tasman Sea, and near 1.5°C for the Chatham Rise. The temperature anomalies in the upper 50m of the ocean are consistent with the 500hPa atmospheric height anomalies. The temperature anomalies in the upper 50m of the ocean are consistent with the 500hPa atmospheric height anomalies and associated winds. The eastern Tasman Sea during August 2021 to July 2022 experienced the highest annual number of MHW days during the satellite-era (1981-present) from OISSTv2.1 data. Under 1.5°C of global warming the four events would have ERIs of 2-3 years, and with 2°C of warming all would be considered cool years relative to the +2°C climate. For the 1957-2022 period, the two most intense heatwaves have ERIs of between 30 to 150 years.

Major loss of glacial ice occurred from Southern Alps glaciers with rapid melt of seasonal snow in all cases. Slow advances in grape phenology since 1948 may be associated with increases in temperature over the same period. Cherries and apricot harvest dates advanced by one to two weeks. Marine impacts may be linked to starvation of kororā/Little Penguin (*Eudyptula minor*) chicks in the Bay of Plenty. Chicks weighed less and had a lower body condition score in 2020 and 2021 compared to 2019 and rescue calls in 2021 reached the highest volumes since 2015. The first record of warm-water prey species in the diet of yellow-eyed penguins at Moeraki occurred, as well as widespread sea-sponge bleaching around northern and southern NZ.

1. INTRODUCTION

Yet another unparalleled heatwave occurred during the austral summer of 2021/22 in the New Zealand region. This followed a very warm summer in 2018/19, although not as intense as the 1934/35 or 2017/18 events. Salinger et al (2020) reviewed the characteristics of the three warmest austral summers (DJF) in the NZ region (approximately 4 million km^2) of 1934/35, 2017/18 and 2018/19. These summers experienced the most intense coupled ocean-atmosphere heatwaves on record.

Kidson (1935) described the first documented austral summer (DJF) heatwave covering the New Zealand (NZ) area in 1934/35, with regional temperatures anomalies over land averaging +1.7°C compared to the 1981-2010 normal. At the time this event was so unusual, almost 3°C warmer than other 1930s summers, it was described as "remarkably warm". Salinger et al (2019a) documented the unprecedented austral summer (DJF) 2017/18 heatwave covering the NZ region. Regional average air (over land) and sea surface temperature (SST) anomalies were +2.2°C and +1.9°C, respectively. Terrestrial and marine impacts that may be linked to the coupled atmosphere/marine heatwave (AHW/MHW) persisted for the entire austral summer resulting in (1) the largest loss of glacier ice in the Southern Alps since 1962; (2) early Sauvignon blanc wine-grape maturation; and (3) species disruption in marine ecosystems. The effects on marine ecosystems considered here included mortality of inshore low trophic level species, and distribution of pelagic species.

Average air temperature anomalies over land were +1.7 to 2.1°C while SSTs were 1.2 to 1.9°C above average. All three earlier heatwaves exhibited maximum SST anomalies west of the South Island of NZ. Atmospheric circulation anomalies showed a pattern of blocking high pressure centred over the Tasman Sea extending southeast of NZ, accompanied by strongly positive Southern Annular Mode conditions, and reduced trough activity over NZ. Rapid melt of seasonal snow occurred in all three cases.

For the 2017/18 and 2018/19 events, combined ice loss in the Southern Alps was estimated at 7.0km^3 water equivalents (22% of the 2017 volume). Sauvignon blanc and Pinot noir wine grapes had above average berry number and bunch mass in 2018 but were below average in 2019. Summer fruit harvest (cherries and apricots) were 14 and 2 days ahead of normal respectively. Spring wheat simulations suggested earlier flowering and lower grain yields compared to average, and below-average yield and tuber quality in potatoes crops occurred. Major species disruption occurred in marine ecosystems. Hindcasts indicate the heatwaves were either atmospherically driven or arose from combinations of atmospheric surface warming and oceanic heat advection.

Using the Hobday et al (2016) definition of MHW[1], Oliver et al (2018) found a 54% increase in the number of MHW days globally since the early 20th century with an increase of 3-9 days per decade in the NZ region. From two General Circulation Model (GCM) ensembles, Perkins-Kirkpatrick et al (2019) and Oliver et al (2017) concluded that a Tasman Sea MHW with the intensity of the 2017/18 event would have been virtually impossible without anthropogenic warming. However, the 1934/35 AHW/MHW stands out as an exception to this conclusion. The atmospheric blocking that was responsible for the prolonged period of high mean sea level pressure (MSLP) also displayed some anthropogenic influence, although Perkins-Kirkpatrick et al (2018) note that this detected influence was less than that on the sea surface temperature.

[1] A MHW is defined as a prolonged discrete anomalously warm water event that can be described by its duration, intensity, rate of evolution, and spatial extent. Specifically, an anomalously warm event is considered to be a MHW if it lasts for five or more days, with temperatures warmer than the 90th percentile based on a 30-year historical baseline period.

MHWs are caused by a range of processes at different spatial and temporal scales, from localised air–sea heat flux to large-scale climate drivers such as the El Niño/Southern Oscillation (ENSO; Heidemann and Ribbe, 2019) and Southern Annular Mode (SAM; Thompson et al., 2011). Behrens et al (2019) investigated mechanisms of MHWs in the Tasman Sea using a forced global ocean sea-ice model and Argo[2] observations, concluding that they are largely modulated by meridional heat transport from the subtropics through the interchange between the East Australian Current and the Tasman Front. One contributor to the increased frequency of MHWs (Oliver et al., 2018) has been regional warming trends. Sutton and Bowen (2019) documented a 0.1 to 0.3°C per decade increase in ocean temperatures since 1981 with warming penetrating from the surface to 200m depth around coastal NZ and to at least 850m in the eastern Tasman Sea. Ocean/atmosphere diagnostics from SSTs, mean sea level pressure (MSLP) and 500hPa geopotential height anomalies shows that these are coupled over the NZ region (Salinger et al., 2020).

Previous MHWs in the NZ region have been reported to have a number of impacts on marine organisms and primary production (Chiswell et al., 2020; Thomsen et al., 2019; Thoral et al., 2022; Tait et al., 2021). For example, Tait et al (2021) report loss of giant kelp *Macrocystis pyrifera*, in response to the earlier marine heatwaves, although this impact may have been exacerbated by poor water clarity. Currently, New Zealand has no national marine environmental monitoring plan in place that would be able to detect changes resulting from MHWs (Ministry for the Environment, 2019) and there is limited long term temporal data for most coastal areas/ecosystems, although the Department of Conservation has just released its Marine Monitoring and Reporting Framework to guide how marine reserves in NZ are monitored in the future.

This study examines the most recent intense atmospheric heatwave (AHW) and associated MHW for the NZ region covering the austral warm season (November - March) for 2021/22, and compares this with the warm seasons of 1934/35, 2017/18 and 2018/19. It reports the atmospheric and oceanic drivers, describes impacts on selected marine and terrestrial ecosystems, including viticulture. Monthly to decadal atmospheric and oceanic mechanisms were investigated, along with an assessment of future likelihood of similar events.

2. METHODS

Many of the methods used here were described in Salinger et al (2019a) and Salinger et al (2021a). They are outlined briefly here, with new approaches described in more detail.

2.1 Observations of atmosphere and ocean temperature

The 22-station NZ air temperature (NZ22T) series (Salinger et al., 1992) was used to calculate monthly mean air temperature anomalies for 1934-2022, relative to the 1981-2010 normal. These were combined with SSTs for the NZ region of 4 million square kilometres (NZSST) to form combined NZ temperatures for the entire NZ area (NZEEZT) described by Salinger et al (2020). From the daily time series, extreme statistics TX90p (percentage of days when the daily maximum temperature is above the 90th percentile), TN90p (Percentage of days when the daily minimum temperature is above the 90th percentile), and number of days ≥25°C averaged over NZ during 1940-2022 were calculated as in Salinger et al (2019a) for NDJFM. Eight stations were analysed for the 1934/35 event. Monthly SST observations were obtained from Extended Reconstructed Sea Surface Temperature version 5 (ERSST; Huang et al., 2017).

Daily SST estimates came from the NOAA 0.25° daily Optimum Interpolation SST version 2.1 analysis (OISSTv2.1) (Huang et al., 2020) on a 0.25° latitude/longitude grid spanning September 1981-July 2022. These were area-averaged over the eastern Tasman Sea 160-172°E and 35-45°S as in Salinger et al (2019a). A subset of SST estimates from ERSSTv5 for 1934/35 and OISSTv2.1 for the remainder for NDJFMA was also extracted for all 0.25° grid cells that lay within the Exclusive Economic Zone (EEZ) of NZ, corresponding to an area 200 nautical miles in width seaward of the coastline.

The Hobday et al (2016; 2018) MHW definitions were applied to identify and characterise MHWs based on daily (i) area-averaged and (ii) EEZ grid cell SST estimates from OISSTv2.1 as in Salinger et al (2019a) using a MatLab implementation (Zhao and Marin, 2019) of the Hobday et al. (2016) MHW definition. Ocean sub-surface temperature from NOAA's Global Ocean Data Assimilation System (GODAS) data (Saha et al., 2006) were averaged between

[2] Argo is an international program of drifting buoys that collect information from inside the ocean using a fleet of robotic instruments that drift with the ocean currents and move up and down between the surface and a mid-water level. Each instrument (float) spends almost all its life below the surface.

40°S and 45°S, 140°E and 150°W, over the depth range 25 to 600m, and Argo profiles (Jayne et al., 2017) were extracted for the eastern Tasman Sea (160-172°E, 35-45°S).

2.2 Atmospheric circulation

For atmospheric circulation, monthly mean sea level pressures (MSLP) for NDJFM and 500hPa geopotential heights for NDJFM were obtained from the NCEP/NCAR Reanalysis (Kistler et al., 2001) and the ERA-Interim reanalysis (Dee et al., 2011). Several indices were used to characterize the circulation: Trenberth (1976) Z1 and M1 indices and weather regimes over NZ (Kidson, 2000) for the 2017/18, 2018/19 and 2021/22 heatwaves. Z1 measures west-east (zonal) flow and M1 south-north (meridional) flow in the NZ region: negative Z1 is typical in blocking situations when the prevailing westerly to southwesterly flow is absent in the region, especially with negative M1 (northerly flow anomaly). For large-scale circulation and monthly to decadal modes of variability the following were used: the Fogt et al (2009) Southern Annular Mode (SAM) reconstructed index, combined with the Marshall (2003) SAM index, the Southern Oscillation Index (SOI) of Troup (1965), and for the Interdecadal Pacific Oscillation (IPO) Tripole Index (Henley et al., 2015).

2.3 Ocean hindcasts

The ocean hindcast model is based on a global 0.25° configuration (Behrens et al., 2021; Madec et al., 2017; Storkey et al., 2018) and forced with JRA-55-DO v.1.5 (Tsujino et al., 2018) over the period 1958-2022. For this study the period 2000-2022 has been analysed and top 50m anomalies computed by subtracting the climatological mean over the period 2000-2022.

2.4 Recurrence interval of heatwaves

The extremes in a given year can be compared to the estimated distribution of temperatures for the period before that occurrence. A generalised extreme value distribution was fitted to the annual anomalies from the 66-year period 1871-1935, for the 1934/35 extreme, and the 66-year period 1957-2022 for the three more recent events. Expected probability of occurrence and the estimated recurrence interval (ERI) of the heatwaves were made based on the two distributions.

The probability of occurrence and recurrence intervals for a range of warming scenarios was estimated, with warmings of 1.5, 2, 3, and 4°C added to the early part of the record (the fifty years 1871-1920), which is considered close to the "preindustrial" temperature distribution. This was achieved by fitting generalised extreme value distributions to the observed temperature record for 1871-1920, plus the relevant warming offset. Such an approach was taken as it may capture the full distribution of temperature expected in future better than it would be by using climate model estimates.

2.5 Glaciers and seasonal snow

The end of summer snowline (EOSS) time series (Chinn et al., 2012) was used to estimate Southern Alps glacier mass balance from 1977 to 2021 for $EOSS_{Alps}$ (Salinger et al., 2019a). Regression relationships were employed to calculate $EOSS_{Alps}$ for 1935 and 2022, using Hermitage Mt Cook glacier season annual mean temperature, the SAM index, and Kidson (2000) Trough and Block regimes frequencies (Salinger et al., 2019b). The methods of Chinn et al (2012) were used to estimate downwasting and proglacial lake growth.

Estimates of water stored as seasonal snow in the South Island for 2021/22 were provided by the model "SnowSim", available through Meridian Energy Ltd (https://www.meridianenergy.co.nz/who-we-are/our-power-stations/snow-storage/; Garr and Fitzharris, 1996). SnowSim calculates water stored as seasonal snow for key hydro-generating river catchments and is tuned to their long-term water balance.

2.6 Agriculture

Grapes

Daily maximum and minimum temperatures (March 1947 to July 2022) were sourced from the regional meteorological station at the Marlborough Regional Station (41.48°S; 173.95°E). A temperature of 0°C was considered to be a damaging frost.

Grapevine phenology was estimated using a budburst model (García De Cortázar Atauri et al., 2009) and estimated to occur when the accumulated growing degree days (base 5°C) and starting on July 1 (mid-winter in the Southern Hemisphere) had reached 294.4. The dates of flowering and véraison were estimated using the GFV model (Parker et al., 2013) and harvest defined as the date when fruit reaches a soluble solid concentration 20 °Brix (Parker, 2012).

Regional Marlborough yields and areas were sourced from annual New Zealand Winegrowers Vintage survey and Vineyard reports respectively and yield component data from New Zealand Winegrowers Vinefacts[3].

Summer Fruit

Harvest dates were gathered for three varieties of cherries and two varieties of apricots (Table 3) at the Plant and Food Research orchard in Clyde, Central Otago (45.20°S 169.32°E) for 2016-2022, where meteorological data were also obtained.

2.7 Marine ecosystems

Surveys in Northland and Fiordland were conducted in 2022. During the period of the MHWs in this region many sponges showed changes consistent with temperature stress (López-Legentil, 2008; McMurray et al., 2011; Hill et al., 2016; Marlow et al., 2018) and see Bell et al (2022) for full details of survey methods. These changes included the bleaching of sponges with photosynthetic symbionts and tissue necrosis. In Fiordland only *Cymbastela lamellata* was surveyed in Breaksea and Dusky sounds between 21 April and 3 June 2022 since this species was reported to have 'bleached'. Sponge bleaching results from the loss of symbionts from the sponge tissue, making the sponge turn from a dark brown to white colour. The proportion of healthy, partially bleached, and fully bleached sponges was estimated from photoquadrats surveys (10 x 1m^2 at each depth) by SCUBA Diving between 5, 10 and 25m.

Tissue necrosis of sponges was also reported from the north of New Zealand during the 2022 MHW period. The presence and severity of tissue necrosis affecting the massive sponges *Ecionemia alata* and *Stelletta conulosa* were made using existing photographic datasets, videos and in-situ observations at 1 - 20m depth throughout northeastern New Zealand (for full site locations see Bell et al. 2022). Data was collected between February and July 2022. The presence and condition of other sponge species were also noted but not quantified. *Ecionemia alata* and *Stelletta conulosa* were assessed as either healthy, partially sick (<20% visible necrosis) or sick (>20% visible necrosis) (Marlow et al., 2018) and see Bell et al (2022) for full details of survey methods.

Regular monitoring of kororā/Little Penguin (*Eudyptula minor*) nesting sites determined burrow occupancy, reproductive success (number of clutches laid and chicks fledged per pair), chick weights prior to fledging and chick body condition scores. These scores aimed to quantify the condition of the chicks by assessing pectoral muscle coverage over the keel; where a score of one is poor muscle coverage, two is moderate muscle coverage and three is good muscle coverage. Chick development was assessed by overall growth rate and feather development. Deceased kororā were either found washed ashore on Bay of Plenty coastlines (see Figure 13) and were deceased upon arrival or died shortly after and/or collected from Animal Rescue & Rehabilitation Centre Wildlife Trust (ARRC) and externally examined. Hotline calls received during spring/summer periods (September-February) from 2015-2022 were collated and assessed for trends related to SST, Mean Wind Speed, Mean Air Temperature and Total Rainfall. During 2021/2022 a total of 21 kororā were collected for mortality research from Bay of Plenty coastlines.

The diet of yellow-eyed penguins (*Megadyptes antipodes*) at Moeraki, North Otago, was investigated through eight years from 638 casts (vomited remains of indigestible hard parts of prey) and 126 spills (vomited remains of undigested or partially digested prey sometimes spilt during food transfers from adults to chicks) collected from June 2014 to May 2022.

3. RESULTS

3.1 Observations of atmosphere and oceans

3.1.1 Surface temperatures

The coupled ocean-atmosphere heatwaves in the NZ region during the four warm seasons (NDJFM) studied here were the most intense recorded in the NZ and Tasman Sea regions in 150 years of land-surface air temperature records, and ~40 years of satellite-derived SST records (Sutton 2019), as shown in Fig. 1a-f.

For all four heatwaves, both land air and sea temperatures combined were 1.1° to 1.4°C above the NDJFM 1981-2010 averages over the entire region (Salinger et al, 2020) (latitude 32° to 52°S, and longitude150°E to 180°) (Table 1 and Fig. 1.). NZ22T anomalies (Table 1) were 1.4°C, 1.7°C, 1.2°C and 1.2°C respectively (Fig. 1a and Table 1), by far the four warmest on record (Salinger 1979, Mullan et al.,

[3] https://www.nzwine.com/members/sustainability/vine-facts/20212022-season/

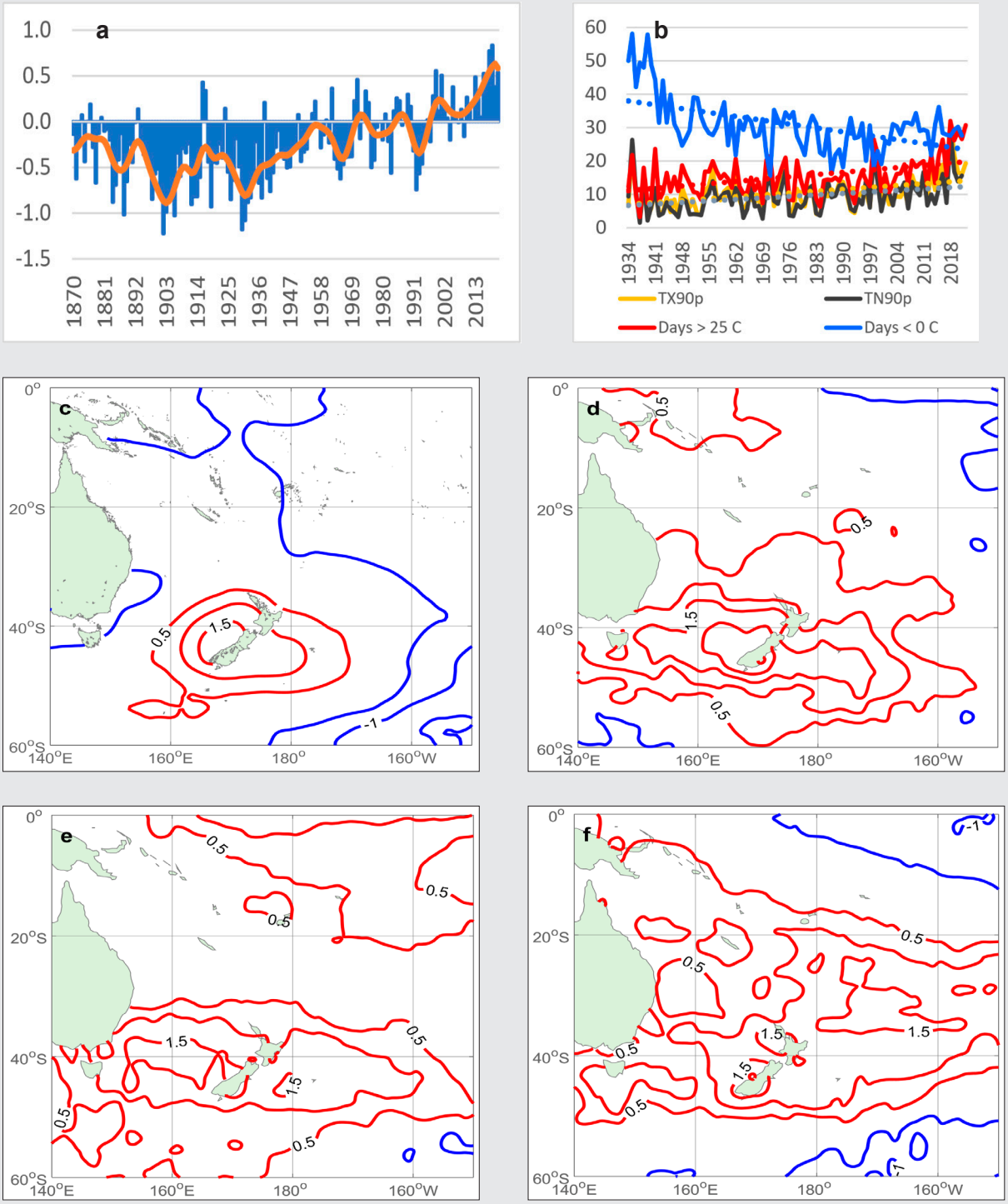

Figure 1: a. New Zealand 22 station air temperature anomalies (°C) (NZ22T) series (red smoothed) 1870-2022; **b.** Extremes – TX90p, TN90p and days >25°C and <0°C averaged over New Zealand 1934-2022; **c.** ERSSTv5 1934/35; **d.** OISSTv2 2017/18; **e.** OISSTv2 2018/19; and **f.** OISSTv2 2021/22. For panel c the climatology period is 1981-2010; and for panels d-f, the climatology period is 1982-2011 and all for the period of NDJFM.

2010). Indices of temperature extremes for NZ (Table 1 and Fig. 1b) show that the percentages of annual warm days above the 90th percentile were 26%, 33%, 22% and 19% respectively. Counts of summer days ≥25°C averaged 22, 32, 26 and 31 days nationwide for the four warm seasons respectively. All these values were statistically significant (Table 1).

For the Tasman Sea and east of NZ (32°–52°S, 150°–

METRIC	1934/35	2017/18	2018/19	2021/22
NZ22T	**+1.37**	**+1.72**	**+1.17**	**+1.19**
ERSSTv5	**+1.07**	**+1.37**	**+1.10**	**+1.10**
NZEEZ	**+1.09**	**+1.39**	**+1.10**	**+1.01**
SAM	**+1.37**	**+1.33**	**+1.66**	**+2.16**
NINO3.4	+0.10	-0.90	+0.79	-0.97
SOI	**+5.0**	**+4.8**	-2.2	**+10.5**
IPO	-0.021	**-0.925**	-0.146	**-1.328**
Z1	**-23**	**-17**	-11	**-33**
M1	**-52**	**-27**	**-35**	-3
Trough	NA	-6.7	**+7.7**	**-10.7**
Zonal	NA	-15.5	**-3.8**	**-15.1**
Block	NA	+22.6	**+6.4**	**+26.0**
Warm days TX90p	**26**	**33**	**22**	**19**
Warm nights TN90p	**26**	**29**	**17**	**16**
Days ≥25°C	**22**	**32**	**26**	**31**

Table 1: Indices for the four heatwaves for NDJFM. NZ22T is the 22 station NZT series for surface temperature over the land area of New Zealand, ERSST is the ERSST version 5 for the New Zealand (NZ) Exclusive Economic Zone, 34 to 48°S, and 165° to 179°E, and NZEEZT are NZ22T and ERSST combined and weighted for the entire NZ region with anomalies in °C. All temperature departures are anomalies from the 1981-2010 climatology period for the months of November – March. NZ22T mean 0.02°C, standard deviation (s.d.) of ±0.42°C, ERSST mean 0.0, s.d ±0.29°C, and NZEEZT mean -0.2 s.d ±0.54 °C. SAM the Southern Annular Mode (Fogt et al 2009) mean 0.06, s.d 1.08, Nino3.4 the Index mean 0.0, s.d 1.3, the Troup Southern Oscillation Index (SOI, Troup 1965) mean 0.0, s.d. 1.0 and the Interdecadal Pacific Oscillation (IPO) the tripolar index (Henley et al., 2015) mean -0.9, s.d. 0.83. Z1 (mean +0.3 s.d. 14.5) and M1 (mean +1.2, s.d, 19.6) are Trenberth (1976) zonal and meridional indices. Kidson regimes are Trough, Zonal and Block anomalies (Kidson 2000). TX90p and TN90p are the percentages of days above the maximum (TX) and minimum (TN) daily 90 percentile (mean is 10% 1981-2010 climatology period, with Days ≥25°C counts, all averaged for 26 NZ climate stations. Mean counts days ≥25°C 15.0, d ±5.2 days. Bolded values significant at $p<0.05$.

180°E) the four periods were characterised by SSTs 1.1°C, 1.4°C, 1.3°C and 1.2°C above average (Figs. 1c-f), the largest anomalies on record. The three earlier periods also showed a similar spatial pattern with highest anomalies to the west of the South Island of NZ, whilst the last was broader in extent.

Applying a MHW definition (Hobday et al., 2016) to daily area-averaged SST from OISSTv2.1 for the eastern Tasman Sea (Fig. 2) showed that the region experienced MHW conditions for 292 days (d) August 2021 to July 2022 (Fig. 2a-b), the highest annual number of MHW days observed for this area over all corresponding annual periods during the satellite-era (1981-present). The majority (79%) of these days during the 2021/22 period were ranked as a Category I (Moderate) event from an areal average (Hobday et al., 2018), with the remainder (21%) as a Category II (Strong) event. The longest continuous MHW occurred during austral autumn and lasted 158 days (Feb 24 2022 – Jul 31 2022) peaking as a Category II (Strong) MHW with a mean intensity of 1.3°C (Fig. 2a,c). This is the second longest individual MHW detected in the eastern Tasman Sea, having a similar duration but reduced intensity and later onset and decay period compared to the summer 2017/18 and 2018/19 events. In comparison, the 2017/18 MHW lasted for 153 days, peaking as a Category IV (Extreme) MHW, with a maximum (mean) intensity of 3.8°C (2.0°C), whilst the 2018/19 MHW lasted for 173 days, peaking as a category II (Strong) MHW with a maximum (mean) intensity of 2.7°C (1.6°C).

Applying a MHW definition to daily SST from OISSTv2.1

grid cells within the New Zealand EEZ (200 nautical miles in width seaward of the coast; Fig. 2d-g) reveals marked spatial variation in the duration and severity of MHWs in coastal waters between August 2021 and July 2022. The most prolonged MHW conditions were experienced along the western coast of the North Island and southeast coast of the South Island (>200 days), with the majority (>70%) of these days ranked as a Category I (moderate) conditions (Fig. 2d). Category II (strong) conditions were largely restricted to the western coast of the North and South Islands, where they were established for a total of 40-60 days depending on location (Fig. 2e). Similarly, Category III (severe) and IV (extreme) conditions were also mostly limited to the northwest and southwest coastlines of New Zealand and were present for a total of 10 - 20 days (Fig. 2f-g). MHW conditions were generally most short lived (50-100 days; Fig. 2d-e) adjacent to the southeast coastlines of the North Island (e.g. east of 176°E) and within the Subantarctic Zone (e.g. south of latitude 48°S).

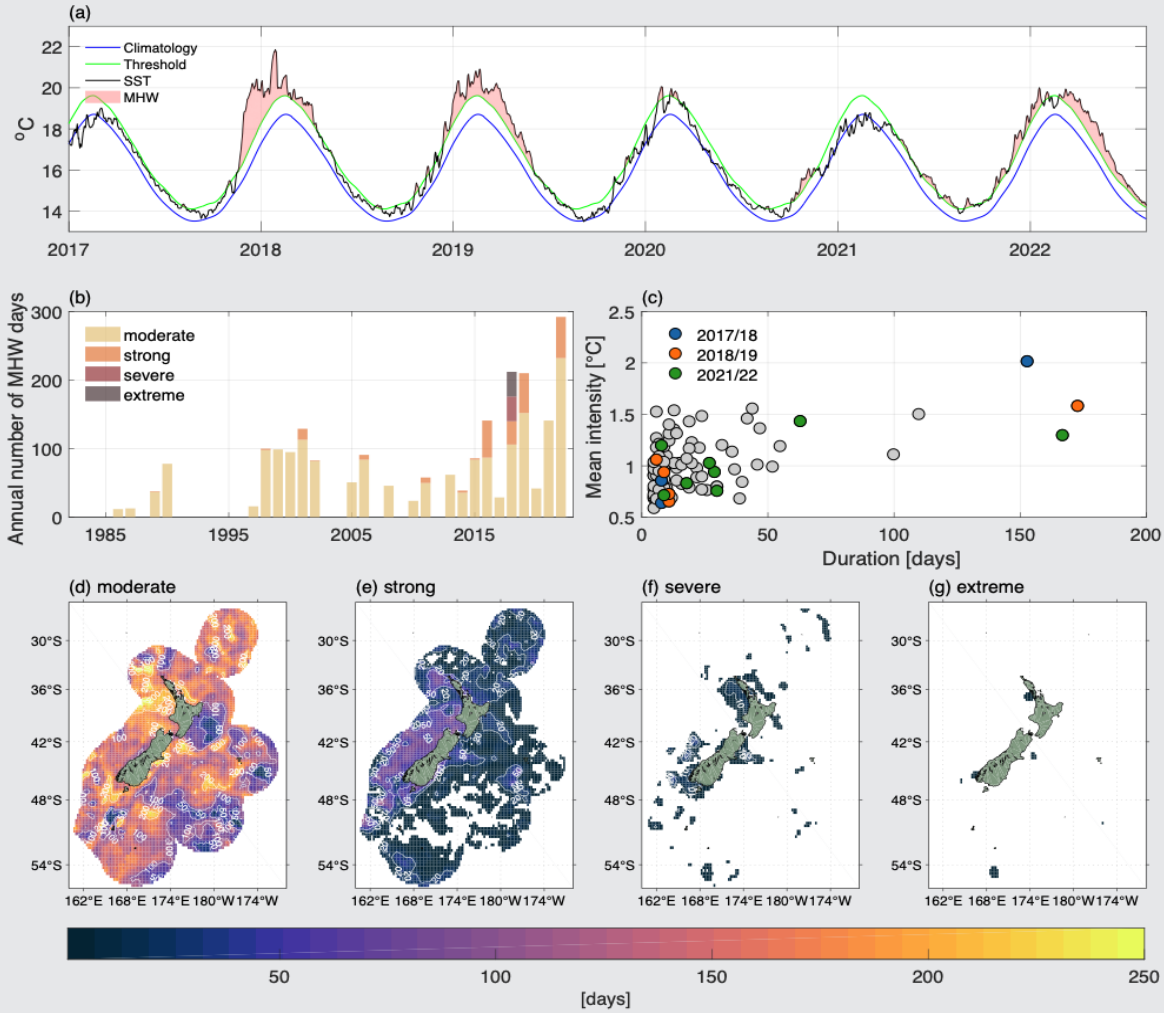

Figure 2: a. Time series of area-averaged sea surface temperature (SST) climatology (1981-2011; blue), 90th percentile MHW threshold (green) and January 2017 to July 2022 SSTs (black) for the eastern Tasman Sea (160-172°E, 35-45°S). The red shaded regions identify periods associated with MHWs using the Hobday et al. (2016) definition. **b.** Annual number of days that the eastern Tasman Sea was in a MHW. The shaded regions identify the number of days spent in one of the four MHW categories based on the Hobday et al. (2018) MHW categorization scheme. The summation in (b) has been performed over 12 month periods of August to July in consecutive years. **c.** The duration and mean intensity of each MHW detected in the area-averaged SST time series for the eastern Tasman Sea. Individual MHWs detected in the 12-month periods of August to July of 2017/18, 2018/19 and 2021/22 are shaded. **d-g.** The number of days each 0.25° lat-lon OISSTv2.1 grid cell within the New Zealand EEZ spent in one of the four MHW categories based on the Hobday et al. (2018) MHW categorization scheme between August 2021 and July 2022.

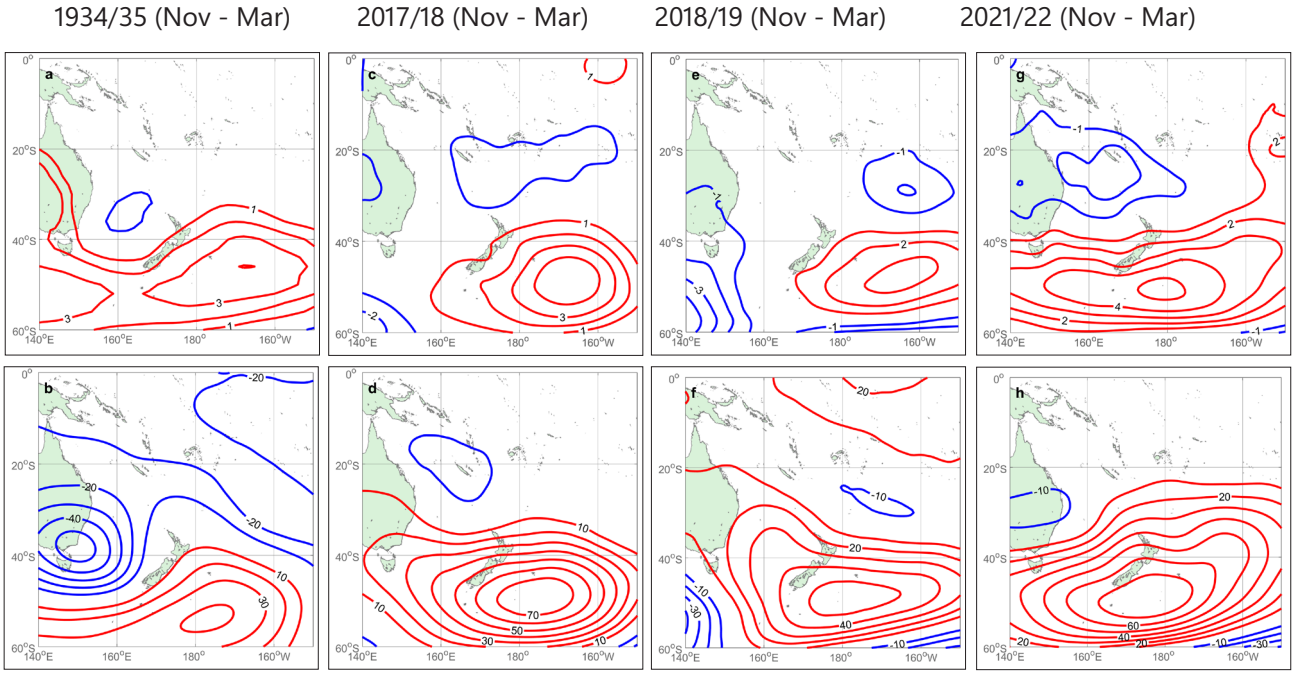

Figure 3: Atmospheric circulation patterns. NDJFM mean sea level pressure anomalies (1981-2010 climatology): **a.** 1934/35, **c.** 2017/18, **e.** 2018/19 and **g.** 2022. NDJFM 500hPa Geopotential Height anomalies (1981-2010 climatology): **b.** 1934/35 **d.** 2017/18, **f.** 2018/19 and **h.** 2021/22. Please note that 1934/35 data are based on the 20th Century Reanalysis dataset (Compo et al., 2011); for the other time periods, the NCEP-DOE AMIP-II Reanalysis dataset was employed (Kanamitsu et al., 2002).

3.1.2 Atmospheric circulation

The four NDJFM seasons (Fig. 3a, 3c, 3e and 3g) show a pattern of blocking (persistent higher than normal pressures): in 1934/35 to the south and southeast of NZ, with negative pressure anomalies northwest of NZ, and the other three very strong blocking to the southeast of NZ and negative pressure anomalies to the north. The M1 and Z1 circulation indices showed northeasterly airflow for 1934/35, 2017/18 and 2018/19. Airflow was easterly for 2021/22. Kidson weather regimes showed a lack of zonal regime for the recent three warm seasons (NDJFM) and more blocking throughout the season especially for 2021/22, where troughing was also absent.

The 500-hPa geopotential height anomalies were extremely consistent (Fig. 3b, 3d, 3f and 3h) with very strong blocking to the southeast of NZ, with average positive height anomalies of 50 geopotential metres or more in the most recent three. The 1934/35 had positive height anomalies extending west of the North Island over the north Tasman Sea. The 2017/18 and 2021/22 anomalies were the most intense, reaching 70 geopotential metres (gpm) to the southeast of the South Island.

Over the austral warm season 1934/35 and 2021/22 the SAM was very positive, although no records were set (Table 1). The SAM was also positive during 2017/18 and 2018/19. The Oceanic Niño Index (ONI) showed weak activity in 1934/35 (Niño 3.4 +0.1) but stronger in 2018/19 (+0.8). The 2017/18 and 2021/22 were in the La Niña phase (+0.9 and +1.0 respectively) for the ONI moderately so, and the IPO strongly negative with very high Southern Oscillation Index (SOI) values (Table 1).

3.1.3 Ocean Sub-Surface Temperature

GODAS sub-surface ocean temperature patterns for (November - April) NDJFMA 2017/18, 2018/19 and 2021/22 for the latitudes 40-45°S (Fig. 4a-c) indicate very shallow positive anomalies west of the South Island, with a narrow band down to about 50m east of the South Island.

Positive SST anomalies also existed in the western Tasman Sea and into the South Pacific east of NZ. The Argo measurements (Fig. 4d) averaged over the eastern Tasman Sea confirmed surface warming from November to February, peaking at 3°C mean anomaly in 2017/18 and 1.5°C in 2018/19, both with shallow anomalies to the upper 20m. A different signal occurred for 2021/22, much weaker, but much more persistent from October to April, and extending all the way down to 150m in 2022.

3.1.4 Ocean hindcasts

The top 50m November - March modelled temperature anomalies for 2018/19 and 2019/20 are spatially very

coherent (Figs. 5a-b). Positive temperature anomalies in the order of 1°C were found over the Tasman Sea and anomalies near the Chatham Rise in both years reached 1.5°C for this five-month period. The anomaly pattern for 2021/2022 differed in the shape (Fig. 5c) compared to the other two periods. The western part of the Tasman Sea, near Australia, did not exhibit positive temperature anomalies over this depth range, while the positive temperate anomalies extended further north and east of New Zealand compared to the other two periods. Conversely, anomalies over the Campbell Plateau and southeast of the Chatham Rise were lower in 2021/22. The difference in the top 50m temperature anomaly pattern between these three periods matches the atmospheric anomalies (500hPa Figs. 3-d, f, and h) and associated wind anomalies. Area averaged top 50m temperature anomalies around New Zealand (Fig. 5d) reveal how different these three periods were compared to previous years. November-March 2017/18 showed the largest peak anomalies for this region and reaching 0.9°C in February. Nevertheless, positive temperature anomalies for 2018/19 and 2021/22 for these two periods persisted into early winter (June), which has not been observed previously. However, climate projections with New Zealand's Earth System Model suggest that this might become the new normal, where positive anomalies disproportional extend into autumn as the ocean warms under climate change (Behrens et al., 2022).

3.1.5 Recurrence interval of heatwaves

Based on the temperature distribution up to 1934/35 (Fig. 6a) the 1934/35 summer was very rare with a

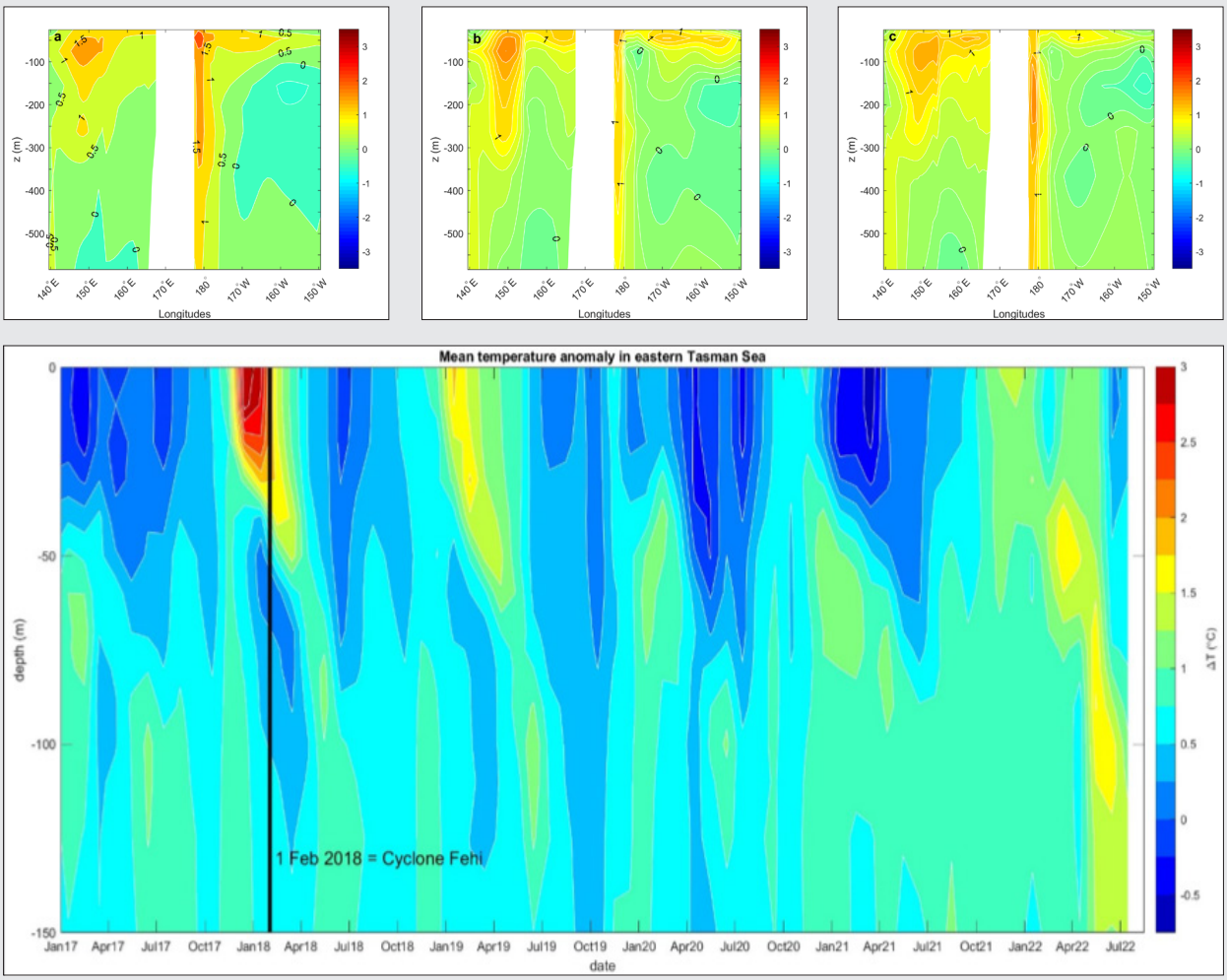

Figure 4: Subsurface temperature anomalies. **a, b, c** and **d.** GODAS subsurface Tasman Sea, 40°S and 45°S, 140°E and 150°W, over the depth range 25 to 600m. **a.** NDJFM 2017/18 **b.** NDJFM 2018/19 and **c.** NDJFM 2021/22 and **d**. Eastern Tasman Sea from Argo floats January 2017 – 4 April 2022.

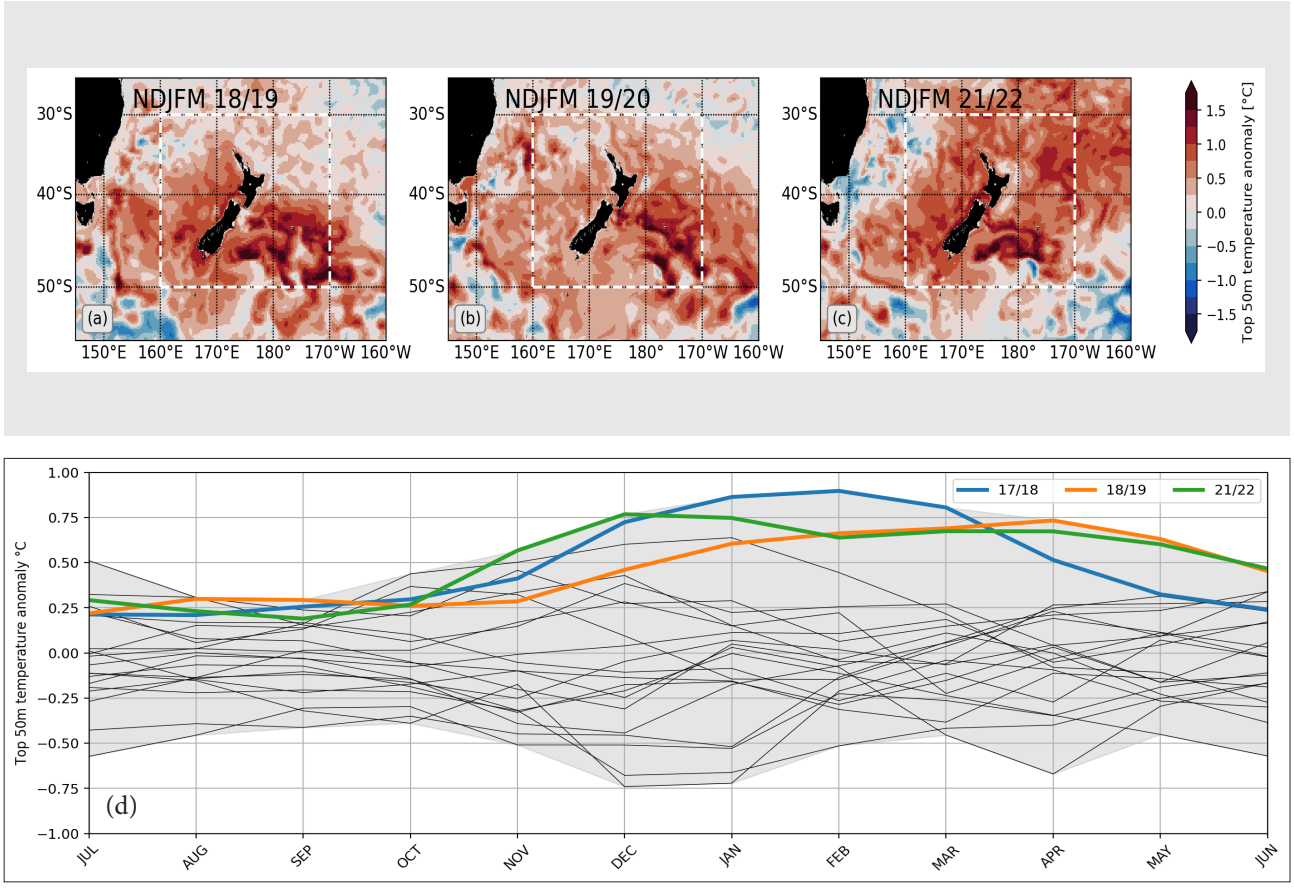

Figure 5: Modelled top 50m temperature anomalies relative to the climatological mean over the period 2000-2022. **(a)** November-March 2018/19, **(b)** November - March 2019-2020 and November - March 2021/22. **(d)** Top 50m area-averaged temperature anomalies over the region 160°E-170°W and 50°S-30°S (white dashed box in a-c) for individual years from 2000-2022 (black lines). The three warmest summers (a-c) are colour coded.

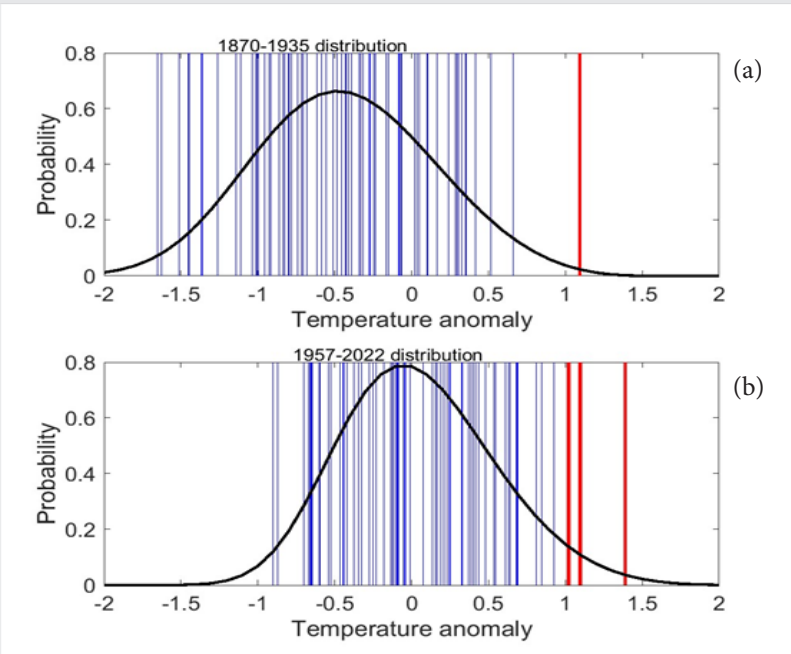

Figure 6: Probability of extreme warm season periods (November – March) for the period before that occurrence. (a) 1870 – 1935, and (b) 1857 – 2022. Heatwave seasons marked in red (see Table 1) and all other seasons in blue. The black lines show fitted GEV distributions.

probability of occurrence of 0.003, or an ERI of around 320 years. Using the 1957-2022 distribution, the 1934/35 event is still relatively uncommon, with an estimated ERI of around 40 years (Fig. 6b). For the recent extreme warm summers, compared to the temperature distribution from 1957 to 2022 (Fig. 6b), we find the two most recent have ERIs of around 30 years while 2017/18 has an ERI of around 150 years.

In the estimated future distributions with 1.5° or 2°C warming (added to the 1870-1920 distribution), such a summer would be common even under 1.5°C warming with ERIs of 2-3 years. Under 2°C warming, those years would all be cooler than average and would be occurring, as cool years, approximately one to two times per decade. Under the current climate warming trajectory this would be reached around the 2060s (Mullan et al 2016).

It is notable that with three or more degrees of warming (from the 1871-1920 period), all four of the heatwaves discussed here would count as unusually cold summers, with ERIs (for cold summers) of 40 years or more for 3 degrees of warming, and in the thousands of years for 4 degrees of warming.

3.2 Glaciers and seasonal snow

3.2.1 Glaciers

Ice volume loss in the Southern Alps for the small and medium glaciers was estimated to be 0.4km^3 volume in 1934/35, 2.1km^3 in 2017/18, 2.0km^3 in 2018/19 and 1.7km^3 for 2021/22.This totals 5.9km^3 for the three recent heatwave warm seasons, 22% of the total ice volume of the Southern Alps in the 1977 inventory (Chinn 2001). For the three recent heatwave summers, total losses from all glaciers amounted to 9.3km^3, 17% of the 1977 total (Fig. 7a). The 2018 – 2022 period represents the largest ice loss in any 5-year period since 1949 (Salinger, et al 2021).

3.2.2 Seasonal snow

The 1934-1935 snow year was likely remarkable. Water stored as seasonal snow reached a maximum that was just below average at 402mm water equivalents (w.e.) in mid-October, based on SnowSim model estimates. Rapid snowmelt began in mid-November and all snow had disappeared by 11 January, the third earliest date for the 1930-2019 period (Fitzharris and Garr, 1995; de Latour, 1999). Melt rate over this period was 6.5mm/d

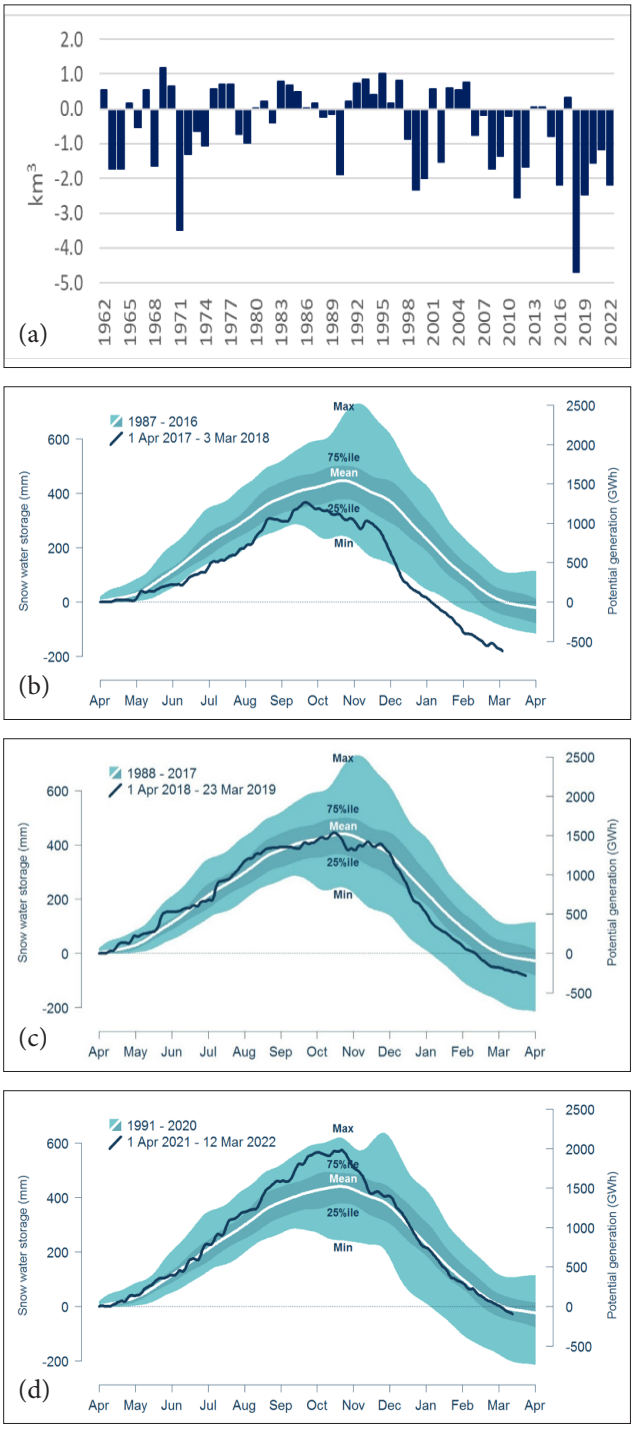

Figure 7: Southern Alps ice volume and seasonal snow. **a.** Southern Alps ice volume change (km^3 of water equivalent), between years, for all glaciers of the Southern Alps from 1962 to 2022. **b-d**. Estimated water stored as seasonal snow (mm) from SnowSim for the period 2017 – 2022.

w.e., the highest of the four summers. The earliest date for disappearance of all seasonal snow is 28 December for the 1974-75 snow year, but this was from a maximum of only 198mm w.e., amongst the lowest since 1930.

During the 2017-18 snow year, the estimated water

stored as seasonal snow leading up to August (Fig. 7b) was very low. It reached a maximum of 30% of average at 350 mm w.e. in late September, much earlier than usual. Rapid melt began on 18 November and from mid-December 2018 the snowpack was the lowest on record. By 10 January all the seasonal snow had melted, the second earliest date since 1930, with extraordinary loss of permanent glacier snow and ice. Melt rate over this period was 5.7mm/d w.e. SnowSim estimated that maximum accumulation for the 2018-19 snow year was close to average at 420mm w.e. and occurred in late October (Fig. 7c), slightly later than normal. There was rapid melt from late November, but it took until 12 February for all the seasonal snow to disappear. Melt rate over this period was 5.0mm/d w.e.

For the 2021-22 snow year, the estimated water stored as seasonal snow leading up to the peak (Fig. 7d) was very high. It reached a maximum of 135% of the normal. There was rapid melt from late November, but it took until 12 February for all the seasonal snow to disappear. Melt rate over this period was 5.0mm/d w.e. 410mm w.e. in late October, at the usual time. Rapid melt began at the beginning of November and by 1 March 2022 the snowpack was totally depleted, and reached the 25 percentile by the end of March, representing the loss of 50mm. By early March all the seasonal snow had melted, with a loss of permanent glacier snow and ice. Melt rate over this period was 1.7mm/d w.e.

3.3 Agriculture

Grapes

The mean daily temperature during the flowering, the period defining fruitset and berry number per bunch periods of 2021 and 2022 was 16.8 and 18.9°C respectively. The seasonal differences were largely the result of a cold six-day period in the middle of flowering in the 2021 vintage where daily temperatures did not exceed 15°C.

Seasonal differences in grapevine yield ranged from a high of 15.2 and 7.56 Tonnes/hectare (T/ha) for the 2022 Sauvignon blanc and 2020 Pinot noir harvests respectively, to a low of 10.3 and 3.59T/ha in 2021 (Fig. 8), likely reflecting these seasonal differences driving bunch mass differences (Table 2). However, for Sauvignon blanc, bunch mass differences largely reflect differences in berry number per bunch rather than berry mass, but the reverse was true in Pinot noir, where berry number per bunch were more similar and berry mass varied, particularly between 2021 and 2022 (Table 2). The difference between the varieties is

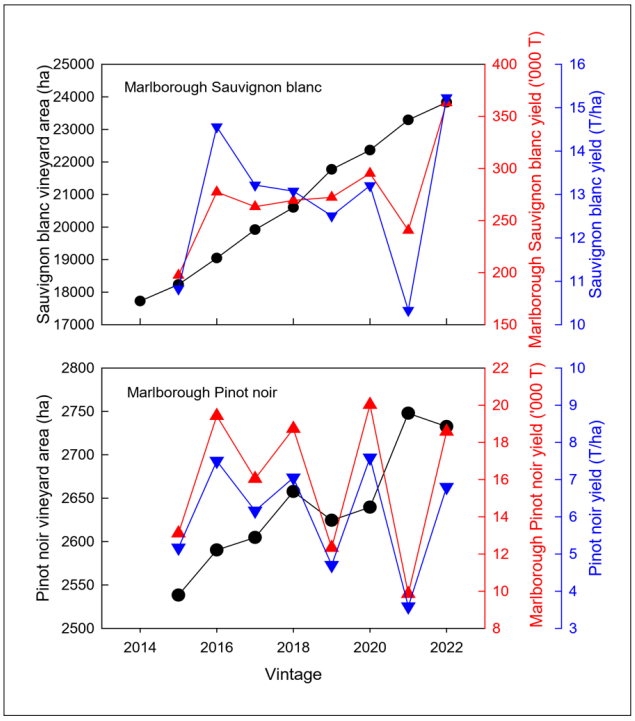

Figure 8: Seasonal variation in Marlborough Sauvignon blanc and Pinot noir vineyard areas and grapevine yields. ● Vineyard area, ▲ Marlborough grape yield, ▼ Marlborough grape yield per ha.

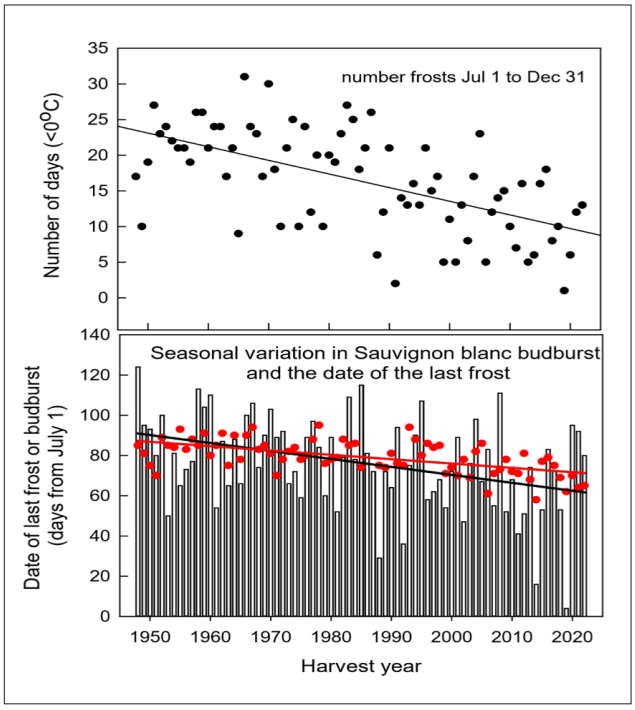

Figure 9: Number of Marlborough spring frosts (<0°C) (1 July to 31 December) (upper) and the date of the last frost and estimated date of Sauvignon blanc budburst (lower).

Bars = date of last frost and ● = date of budburst.
Date (days from July 1) of last frost =861-0.40x; date of budburst = 507-0.216x.

	AVERAGE		VINTAGE				
		Cv*	2018	2019	2020	2021	2022
PINOT NOIR	**2015 - 2022**	**2015 - 2022**					
Average bunch mass (g)	68.0	29.0	109.7	48.4	70.9	43.4	68.14
Average berry mass (g)	1.2	18.9	1.62	0.90	1.11	0.92	1.26
Average berry number per bunch	58.2	11.7	67.9	53.8	63.7	47.2	54.1
Inflorescence number per m row	24.4	14.4	23.7	32.0	21.2	27.3	20.2
SAUVIGNON BLANC	**2017 - 2022**	**2017 - 2022**					
Average bunch mass (g)	128.5	18.5	156.6	126.7	144.7	90.3	145.1
Average berry mass (g)	2.0	10.3	2.2	1.7	1.8	1.8	2.1
Average berry number per bunch	64.1	16.3	73.2	73.7	78.4	49.3	69.1
Inflorescence number per m row	23	12.9	24	23	20	26	25
	1948 - 2021	**1948 - 2021**					
Initiation temperature (°C)	17.4	6.1	17.9	18.7	19.2	15.9	17.4
Flowering temperature (°C)	17.1	6.3	18.8	19.1	16.4	16.9	19.0

Table 2: Sauvignon blanc and Pinot noir yield components.
*cv = coefficient of variation

		2016	2017	2018	2019	2020	2021	2022
Cherry	'Lapins'	12/1	18/1	31/12	9/1	10/1	4/1	5/1
	'Sweetheart'	25/1	18/1	8/1	12/1	15/1	5/1	10/1
	Staccato®	29/1	3/2	15/1	22/1	25/1	21/1	12/1
Apricot	'Nzsummer2'	3/2	6/2	19/1	30/1	31/1	26/1	31/1
	'Nzsummer3'	9/2	20/2	26/1	9/2	7/2	9/2	1/2

Table 3: Harvest dates of summerfruit in Central Otago.

largely a reflection of the ability of Pinot noir to set seedless berries (resulting in millerandage - a potential viticultural hazard problem in which grape bunches contain berries that differ greatly in size and, most importantly, maturity), whereas few seedless berries are observed in Sauvignon blanc.

The number of days with minimum temperatures between 1 July and 31 December less than 0°C has consistently reduced between 1948 and 2022 (Fig. 9) and the date of the last frost has advanced by 0.40 days per year over the same period (Fig. 9). However, warming of mean daily temperature 0.019°C /day between 1 July and 31 August (Fig. 9) has also advanced the date of budburst

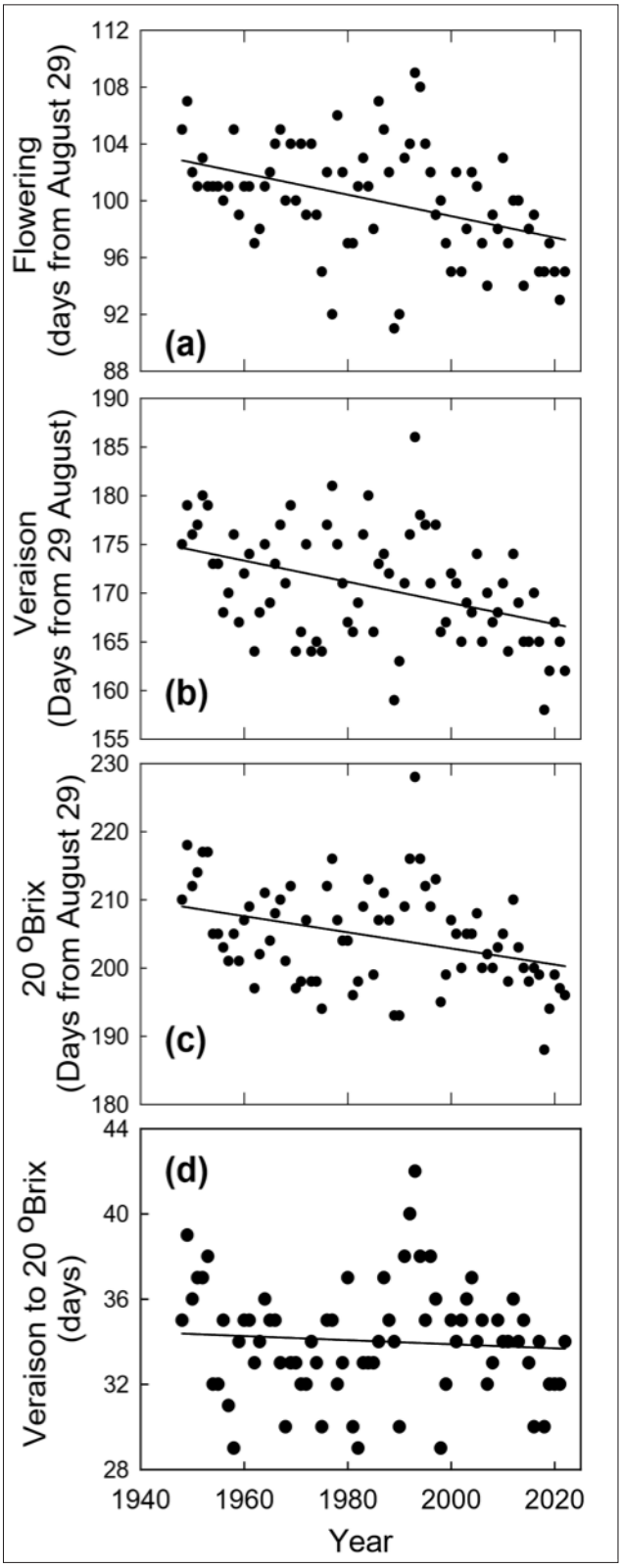

Figure 10: Seasonal changes in grapevine phenology estimated using GFV model (Parker et al., 2013) (Parker, 2012).

by 0.26 days per year, with the result seasonal frost risk has changed little over the past 74 years.

The GFV model simulations of flowering, véraison, and harvest dates advanced since 1948 (Fig. 10) and reflect an average increase in temperature of 0.013°C / day in the spring period (1 September to 30 November). Similar, but smaller temperature increases occur between 1 December and 15 February (0.011°C /day) but this advance had little effect on the average temperature over the flowering period, which has increased on average by 0.01°C per year. Similarly, there was little increase during ripening between 16 February and 15 April (0.001°C /day).

Summer Fruit

Of the AHW season's data available, September to January temperature departures from normal for 2018, 2019 and 2022 were +2.2, +0.6 and +1.0°C. For the three cherry varieties, 2018, 2019 and 2022 harvest dates averaged 13, 8 and 13 days respectively ahead of 2016 (a normal season). For apricots, the three AHW summers were 15, 3 and 6 days ahead of normal.

3.4 Marine ecosystems and impacts

In northeastern New Zealand, sponge necrosis was recorded at depths between 1–20m across including *Ecionemia alata* and *Stelleta conulosa*, with other unquantified reports of tissue loss/regression of *Stelletta maori*, *Cliona celata*, *Dendrilla rosea*, T*ethya* spp. and detached *Polymastia* spp. being washed up on the shore. Up to 45% of sponges observed in this region showed signs of necrosis. The greatest impacts appeared to occur on *Ecionemia alata* and *Stelleta conulosa*, where many sponges detached or had the appearance of "melting" off the reef. These species are two of the most common and important habitat-forming species across New Zealand's subtidal rocky ecosystems (although not found as far south as Fiordland). The densities of these two species are conservatively around 1 per 10m^2 (noting a single sponge can occupy up to 1m^2 of reef), with a distribution extends from approximately 5 to >100m depth. Given that necrotic sponges were reported at sites across > 500km of coastline, down to 20m, conservatively hundreds of thousands of sponges are likely to have been impacted (see Bell et al. in press for further information).

In May 2022, correlating with the maximum intensity of the MHW impacting the Fiordland region, widespread sponge 'bleaching' of *Cymbastella lamellata* was reported. Subsequently necrotic and dying sponges across several species were reported in northeastern New Zealand. Greater

Figure 11: Detached and rotting Anchorinidae sponge, Northland, April 2022.

than 90% of *Cymbastella lamellata* observed showing signs of either partial or complete bleaching in Dusky and Breaksea Sounds (Figure 11); There was no difference in the level of bleaching between depth and Remotely Operated Vehicle observations found bleached sponges to 50-60m (max depth sponges were found). While *C. lamellata* was the only species that appeared to be impacted in Fiordland, its high abundance across the region (average 1-10 per m^2 and a coastline of >600km) and depth distribution ranging from 5–60m, indicates that tens of millions of sponges could have been bleached. Some sponges, like *C. lamellata*, contain photosynthetic symbionts, and under temperature stress can expel these symbionts (López-Legentil, 2008).

Large marine impacts may be linked to starvation of kororā in the Bay of Plenty, with reduced chick body mass and condition in 2020 and 2021 compared to 2019, emaciated deceased chicks found in burrows and the highest volume of rescue calls received in 2021, since 2015 (McLuskie, 2023). Regular monitoring of kororā nest sites determined burrow occupancy, reproductive success (number of clutches laid and chicks fledged per pair), chick weights prior to fledging and chick body condition scores (McLuskie, 2023). Mean body mass and body condition of six-week-old kororā chicks in Mount Maunganui (Bay of Plenty) decreased by 19% during the 2020 and 2021 breeding seasons compared to 2019, which coincided with La Niña conditions and increased SST (Table 4). Chick development in 2020 and 2021 was slower than observed in 2019, with a delay in feather development and overall body size of chicks appeared smaller. Chick productivity was slightly lower in 2021 (1.22 chicks per pair), compared to previous seasons (Table 4). Six deceased emaciated chicks were also found within breeding burrows in the 2021 season, that most likely died of starvation. The proportion of burrows occupied by non-breeding birds during the day increased from 5% (2/38) in 2019 to 24% (15/63) in 2021 (Table 4).

The number of kororā rescue calls received by Western Bay Wildlife Trust (WBWT) for the Bay of Plenty region, increased significantly during the 2021/2022 Spring/Summer period (Sep-Feb) when mean Northern North Island SST were warmest (Fig. 12)(McLuskie, in press). Higher than usual call volumes in 2020/2021 and 2017/2018 were also consistent with increased SST. Rescuers observed and received multiple reports of deceased kororā washed ashore across the entire Western Bay of Plenty coastline (see Figure 13) over the 2017/2018 summer period (Graham, pers. comm). Increased call volumes in 2016 were inconsistent with SST trends, however had the highest mean wind speed (4.5m/s) between 2015-2021 spring/summer seasons. In spring/summer of 2021, 13 kororā rescues were attended and 77% (10/13) were found in a weak/exhausted state. Over half of deceased kororā specimens (57%) collected between 2021-2022 spring/summer (n=21) were found in an emaciated condition upon external examination and suspected to have died of starvation, however further research is needed to confirm cause of death.

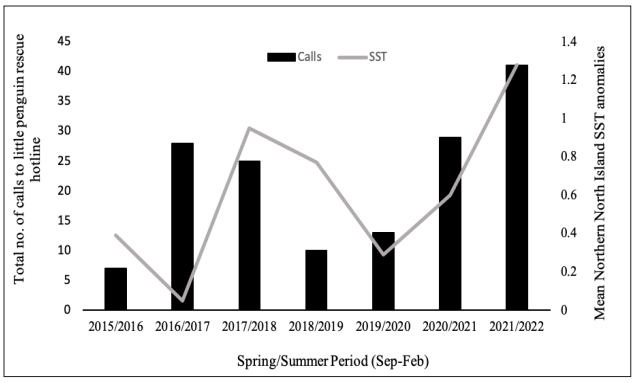

Figure 12: Calls to Western Bay Wildlife Trust kororā rescue hotline. Bay of Plenty, NZ, for 2015-2022 spring/summers (Sep-Feb).

Pilchard *Sardinops sagax* and anchovy *Engraulis australis*, two species of small pelagic nearshore fishes common around most of New Zealand, are absent from Otago, southeast South Island (Roberts et al. 2015, McMillan et al, 2019), where the relatively cool waters of the Southland current flow northward over the continental shelf (Sutton 2003, Stevens et al. 2021). A recent exception to this absence was a mass stranding of pilchard near Oamaru, North Otago in December 2019 (MacLean 2019). Through the eight years of sampling yellow-eyed penguin

Breeding Season (Jul-Feb) * La Niña	Ocean Conditions		Productivity			Chick Health			Burrow Occupancy	
Year	SOI-RM Rolling 3 month average	Mean SST (Nthn North Island)	n	Chicks per pair	Replacement clutches (Second clutch following first clutch failure)	n	Mean Mass (g)	Body Condition Score (1-3)	n	Non-breeding bird occupancy rate %
2019	-0.41	0.34	20	1.30	7	10	951	2.4	38	5
*2020	0.76	0.59	32	1.31	4	14	768	1.93	51	8
*2021	0.94	1.13	36	1.22	1	19	768	1.95	63	24

Table 4: Burrow occupancy, chick production and health in kororā based in Mount Maunganui, North Island, NZ, and associated ocean conditions (Southern Oscillation Index and Sea Surface Temperature) 2019-2021 (McLuskie, 2023).

prey remains at Moeraki from June 2014 to May 2022, pilchard and anchovy were each recorded only once. In both cases they were recorded in the most recent year, with two pilchard in a cast on 27 July 2021 and one anchovy in a spill on 14 August 2021. Both records coincided with a marine heat wave and may signal a future change in diet of yellow-eyed penguins with warmer ocean temperatures at Moeraki. If this is the case, then there would be an expectation of future increasing occurrences of pilchard and anchovy in the ongoing study of diet of yellow-eyed penguins at Moeraki.

4. DISCUSSION AND CONCLUSIONS

Heatwaves are becoming a major impact of global warming with the Intergovernmental Panel on Climate Change 6th Assessment Report (Seneviratne et al., 2021) indicating likely increases in unusually warm days and nights across most continents, and several occurrences of MHWs in 2020 (Blunden and Boyer, 2020). The unprecedented heatwave in the 2017/18 austral summer, coupled with a combined AHW/MHW event (Salinger et al., 2019a) was one example.

Although Perkins-Kirkpatrick et al (2018) suggests that the 2017/18 MHW would have been "virtually impossible" without an anthropogenic influence, the 1934/35 event indicates a similar episode has occurred in the past which was only 0.3°C cooler, without any allowance for anthropogenic global warming. Hence, it is important to examine similar AHW/MHWs in the NZ region in the climate record to document drivers and impacts. Srinivasan et al (2021) found that in the last decade monthly temperature extremes are increasing 4-5 times faster than expected in a climate with long term warming, and that the increase in extremes is faster than the rate of increase in mean temperature.

Four such austral warm season events occurred – in decreasing order of magnitude 2017/18, 1934/35, 2021/22 and 2018/19. The heatwaves had very similar atmospheric and oceanic footprints, covering all the land area, the entire central and south Tasman Sea and across to 180°E in the southwest Pacific. The recent three MHWs recorded highest annual number of days in the NZ region for all corresponding annual periods during the satellite-era (1981 - present). Mid-tropospheric (500hPa) atmospheric circulation anomalies were extremely similar with strong blocking to the southeast of NZ. Climate projections with New Zealand's Earth System Model suggest that above average temperature anomalies extending into autumn may become the new normal, as the ocean warms under climate change (Behrens et al., 2022), and the patterns are driven by atmospheric circulation interacting with the oceanic circulation.

Projected circulation changes for the late 21st century (Mullan et al., 2016) show MSLP increases during DJF, especially to the southeast of NZ. The airflow over the country becomes more northeasterly, and at the same time associated with more (possibly blocking) anticyclones and lacking in troughs. There is also a trend towards the positive SAM resulting in higher MSLPs in the NZ region, but this depends on interplay with stratospheric ozone recovery (Arblaster et al., 2011). These are all features displayed in the 2017/18, 2018/19 and 2021/22 heatwaves, with circulation regimes and their analogues exhibiting a lack of the troughing regime. Given that the Tasman Sea mixed layer heat content anomalies are in recent years have been above average, it appears likely that human-induced warming has played a significant role in the three recent

coupled ocean-atmospheric heatwaves.

Record-breaking MHWs have been globally documented MHWs (Oliver et al 2021) where the atmospheric state played a central role in their development and maintenance, from the Mediterranean, off the northeast United States and other oceanic areas. In these cases, the anomalously warm ocean temperatures were related to abnormally high air–sea heat fluxes into the ocean, which was the case for the three Tasman Sea/NZ recent MHWs.

Analysis shows that the 1934/35 event was highly unusual with an ERI of over 300 years based on the climate of the time, and of around 40 years even in the climate of the last six decades. However, with 2°C of regional temperature increase all four would be cooler than normal November – March seasons in the future.

All three recent heatwaves produced significant impacts on glaciers and seasonal snow and ice, and on terrestrial and marine ecosystems. Ice loss in small and medium glaciers has been estimated to range from 1.7 to 2.1km^3 w.e. in each event. Across all three heatwave summers, there was an accumulated ice volume loss of 22% of the 2017 volume. In all four cases, SnowSim showed swift snowmelt commencing in mid-November with rapid melt thereafter.

Potential grapevine yield is determined by the number of inflorescence primordia that develop in buds during flowering in the season before harvest, and then the number of berries that set during flowering in the current season (Trought, 2005). Following pollination of the stigma, which occurs shortly after sunrise (Staudt, 1999), pollen tube growth ceases after approximately 18 hours (Staudt, 1982) with the result that the maximum growth of the pollen tube reflects temperatures after pollination, with an estimated mean temperature of 18°C required for fertilization to be successful (Trought, 2005). The low Sauvignon blanc and Pinot noir yields at the 2021 harvest were associated with below average initiation and flowering temperatures of 16.0 and 17.4 respectively, in particular a cold period at the height of flowering in late December. While higher yields in 2022 can be attributed to the initiation and flowering temperatures of 16.8 and 18.9°C respectively.

While the number of spring frosts has declined nationwide since 1948, by approximately 0.19 events per year, and date of the last frost has come forward by a month since 1948, the increase in temperature has advanced the date of budburst and flowering, with the result spring frost risk, the temperature during flowering or ripening has changed little since 1948. Similar changes in frost risk have been observed in Europe (Sgubin et al., 2018). Likewise, mean temperatures during the ripening period did not increase, unlike increases observed elsewhere (Molitor and Junk, 2019). This possibly reflects the temperate climate of Marlborough and the abrupt changes in temperature that may occur between concurrent phenophases of vine development during the season (Salinger et al., 2020).

The slow advances in grapevine phenology since 1948 may be associated with increases in temperature over the same period, marked inter-seasonal variation in temperature, particularly in relation to spring frost, inflorescence initiation and flowering, key stages of yield development, result in marked fluctuation in seasonal yield. Cherries and apricots showed an advancement date for the three AHW warm seasons harvest dates by 12 and 8 days respectively.

The observed impacts of the 2022 marine heatwave on marine sponges in northern NZ and Fiordland are unprecedented and raise concerns for the future of sponge communities which are an important component of temperate reef ecosystems. The contrasting impacts of the marine heatwave on sponges between northern NZ and Fiordland highlight there are multiple mechanisms at play and further research is needed to better understand the actual mechanisms and species-specific vulnerabilities of sponges to marine heatwaves. The longer-term impacts for the sponges that have lost tissue is currently unknown and further monitoring will be needed to assess if they survive or not around northern and southern NZ.

Reduced breeding attempts of kororā, lower chick masses and fewer chicks per pair may be related to increased SST (Cannel et al., 2012; Johnson & Colombelli-Négrel, 2021), but the difference between chicks per pair in this study is marginal and could not be attributed to

Figure 13: One of twelve emaciated kororā found over the 2021/2022 spring/summer period in the Bay of Plenty. A recent fledgling weighing 335g washed ashore weak and dehydrated, on Waihi Beach during the marine heatwave, January 2022.

Figure 14: A group of bleached *Cymbastella lamellata* from Dusky Sound, Fiordland. These sponges contain photosynthetic symbionts and are normally brown in colour. During the 2022 marine heat wave these symbionts were lost from these sponges. Over 90% of sponges across the entire Fiorldand Marine Area were bleached.

ocean conditions. An increase in non-breeding birds could indicate adults sheltering during the day, birds pairing and/or lack of food availability resulting in reduced breeding attempts. Similarly, developmental delays in kororā chicks have also been observed in malnourished chicks going into rehabilitation in Tasmania (Grieveson, pers. comm). Starvation could likely be linked to reduced prey capture success during periods of increased SST (Carroll et al., 2016) that occurred in the Northern North Island resulting in increased hotline call volumes and emaciated kororā washing ashore in the Bay of Plenty, however due to limitations of methodology it cannot be accurately concluded that starvation was the primary cause of death. Disruption to marine ecosystems during 2010/2011 has been previously linked to a significant marine heatwave in Western Australia (Salinger et al., 2016) including an increased number of dead kororā found washed ashore that had died of starvation (Caputi et al., 2014). Hocken (2000) found starvation as the leading cause of mortality in kororā washed ashore in Otago during 1994 to 1998. One of the primary concerns of increased ocean temperatures is the decrease in adult survival, particularly if high numbers of emaciated fledglings are seen and low juvenile recruitment continues. A population model demonstrated a 9% decrease in survival of adult king penguins for a 0.26°C warming in the Southern Ocean (Le Bohec et al., 2008). It is likely that other environmental variables, such as increased wind speeds and high land temperatures (Johnson and Colombelli-Négrel, 2021; Stahel and Gales, 1987) were also contributing factors in reduced breeding success and starvation and requires further investigation. Little is known about the prey species of the Mount Maunganui kororā colony. Further research is needed to investigate the diet of kororā in the Bay of Plenty to find out whether not just sea temperature but also dredging and fishing activities impact breeding success and survival.

The only records of pilchard and/or anchovy in the diet of yellow-eyed penguin at Moeraki through eight years beginning in 2014 was during the last year. Monitoring of the diet of this penguin is ongoing and will document whether or not pilchard and/or anchovy gradually become important in the diet indicating prey switching attributable a southward spread of these small pelagic fishes in response to warming sea temperatures.

ACKNOWLEDGEMENTS

Updates of the Tasman Glacier end of summer snow line data to 1976 were provided by the late Dr Trevor Chinn. Other files from Trevor were used to update the proglacial lake and downwasting of volume for the 12 large glaciers. Pascal Sirguey provided mass balance information from the Brewster Glacier. The Argo data were collected and made freely available by the International Argo Program and the national programs that contribute to it (http://www.argo.ucsd.edu, http://argo.jcommops.org).

The Argo Program is part of the Global Ocean Observing System. The sub-surface temperature and SST data was collected as part of the MBIE funded Coastal Acidification: Rate, Impacts and Management (CARIM) project, provided by Kim Currie. This project obtained support through the Deep South National Science Challenge. This paper was supported through funding from the Ministry of Business, Innovation and Employment via the Deep South National Science Challenge (C01X1902). MST was funded by the Brian Mason Trust (Impact of an unprecedented marine heatwave). PMS was funded by MBIE contract CAWX1801. Bay of Plenty kororā research was obtained under wildlife authorities (48462-FAU & 81642-DOA), thanks to the Department of Conservation, local iwi (Ngai Te Rangi, Ngati Ranginui and Ngati Pukenga) and Tauranga City Council for granting permissions and land use access.

REFERENCES

Arblaster, J.M., Meehl, G.A., & Karoly, D.J. 2011. Future climate change in the Southern Hemisphere: Competing effects of ozone and greenhouse gases. *Geophysical Research Letters*, 38(2). https://doi.org/10.1029/2010GL045384

Bell, J.J., Smith, R.O., Micaroni, V., Strano F., Balemi, C.A., Caiger, P.E., Miller, K.I., Spyksma, A.J.P., & Shears, N.T. 2022. Marine heat waves drives bleaching and necrosis of temperate sponges. *Current Biology,* https://doi.org/10.1016/j.cub.2022.11.013

Behrens, E., Fernandez, D., & Sutton, P 2019. Meridional Oceanic Heat Transport Influences Marine Heatwaves in the Tasman Sea on Interannual to Decadal Timescales. *Frontiers Marine Science*, 6: 228. https://doi.org/10.3389/fmars.2019.00228

Behrens, E., Hogg, A. M., England, M. H., & Bostock, H. 2021. Seasonal and interannual variability of the subtropical front in the New Zealand Region. *Journal of Geophysical Research: Oceans*, 126, e2020JC016412. https://doi.org/10.1029/2020JC016412.

Behrens, E., Rickard, G., Rosier, S., Williams, J., Morgenstern, O., & Stone, D. 2022. Projections of future marine heatwaves for the Oceans Around New Zealand Using New Zealand's Earth System Model. *Frontiers in Climate*, 4: 798287. https://doi.org/10.3389/fclim.2022.798287.

Blunden, J. & T. Boyer, Eds. 2020. State of the Climate in 2020. *Bulletin of the American Meteorological Society*, 102 (8): Si–S475, https://doi:10.1175/2021BAMSStateoftheClimate.1.

Cannell, B., Chambers, L., Bunce, M. & Murray, D. 2012. *Little Penguins (Eudyptula minor) breeding and survival in Western Australia compromised by a "marine heat wave" in 2011*. In: Abstracts of the Australian Marine Sciences Association and New Zealand Marine Sciences Society Joint Conference, 1 - 5 July, Hobart, Tasmania.

Caputi, N, Jackson, G, and Pearce, A. (2014). *The marine heat wave off Western Australia during the summer of 2010/11 – 2 years on*. Government of Western Australia Department of Fisheries, Perth. Report Fisheries Research Report No. 250.

Carroll, G., Everett, J. D., Harcourt, R., Slip, D., & Jonsen, I. 2016. High sea surface temperatures driven by a strengthening current reduce foraging success by penguins. *Scientific Reports*, 6(1). https://doi.org/10.1038/srep22236.

Chinn, T.J. 2001. Distribution of the glacial water resources of New Zealand. *Journal of Hydrology New Zealand*, 40 (2): 139–187. https://www.jstor.org/stable/43922047.

Chinn, T.J., Fitzharris, B.B., Salinger, M.J, & Willsman, A. 2012. Annual ice volume changes 1976–2008 for the New Zealand Southern Alps. *Global and Planetary Change*, 92-93: 105-118. https://doi.org/10.1016/j.gloplacha.2012.04.002.

Chiswell, S.M. & Sutton, P.J. 2020. Relationships between long-term ocean warming, marine heat waves and primary production in the New Zealand region. *New Zealand Journal of Marine and Freshwater Research*, 54(4): 614-635.

Compo, G. P., J. S. Whitaker, P. D. Sardeshmukh, N. Matsui, R. J. Allan, X. Yin, B. E. Gleason, R. S. Vose, G. Rutledge, P. Bessemoulin, S. Brönnimann, M. Brunet, R. I. Crouthamel, A. N. Grant, P. D. Jones, M. C. Kruk, A. C. Kruger, G. J. Marshall, M. Maugeri, H. Y. Mok, Ø. Nordli, T. F. Ross, R. M. Trigo, X. L. Wang, S. D. Woodruff, and S. J. Worley, 2011. The Twentieth Century Reanalysis Project, *Quarterly Journal of the Royal Meteorological Society*, 137 (654), 1-28, doi: https://doi.org/10.1002/qj.776

Dee, D.P., Uppala, S.M., Simmons, A.J., Berrisford, P., Poli, P., Kobayashi, S., et al & Vitart, F. 2011. The ERA-Interim reanalysis: configuration and performance of the data assimilation system. *Quarterly Journal of the Royal Meteorological Society*, 137(656): 553-597. https://doi.org/10.1002/qj.828.

de Lautour, S. 1999. *The climatology of seasonal snow*. MSc Thesis, Department of Geography, University of Otago.

Department of Conservation 2022. *Marine Monitoring and Reporting Framework*. ISBN: 978-1-99-116198-7.

Fitzharris, B., & Garr, G.E. 1995. Simulation of past variability in seasonal snow in the Southern Alps, New Zealand. *Annals of Glaciology*, 21: 377-382. https://doi.org/10.3189/S0260305500016098.

Fogt, R.L., Perlwitz, J., Monaghan, A.J., Bromwich, D.H., Jones, J.M., & Marshall, G.J. 2009. Historical SAM variability. Part II: Twentieth-century variability

and trends from reconstructions, observations, and the IPCC AR4 models. *Journal of Climate*, 22, 5346-5365. https://doi.org/10.1175/2009JCLI2786.1.

García De Cortázar-Atauri, I., Brisson, N. & Gaudillere, J. P. 2009. Performance of several models for predicting budburst date of grapevine (Vitis vinifera L.). *International Journal of Biometeorology*, 53(4): 317-326.

Garr, C.E., & Fitzharris, B.B. 1996. Using seasonal snow to forecast inflows into South Island hydro lakes. In: *Prospects and Needs for Climate Forecasting*, The Royal Society of New Zealand Miscellaneous Series 34: 63-67 [ISBN 0-908654-61-8].

Heidemann, H., & Ribbe, J. (2019). Marine Heat Waves and the Influence of El Niño off Southeast Queensland, Australia, *Frontiers of Marine Science*, 20 February 2019. https://doi.org/10.3389/fmars.2019.0005.

Henley, B.J., Gergis, J., Karoly, D.J., Power, S.B., Kennedy, J., & Folland, C.K. 2015. A Tripole Index for the Interdecadal Pacific Oscillation. *Climate Dynamics*, 45 (11-12): 3077-3090. http://dx.doi.org/10.1007/s00382-015-2525-1. Accessed on 05 27 2019 at https://www.esrl.noaa.gov/psd/data/timeseries/IPOTPI.

Hill, M., Walter, C. & Bartels, E. 2016. A mass bleaching event involving clionaid sponges. *Coral Reefs*, 35 (1): 153-153.

Hobday, A., Alexander, L.V., Perkins, S.E., Smale, D.A., Straub, S.C., Oliver, E.C.J., Benthuysen, J.A., Burrows, M.T., Donat, M.G., Feng, M., Holbrook, N.J., Moore, P.J., Scannell, H.A., Sen Gupta, A., & Wernberg, T. 2016. A hierarchical approach to defining marine heatwaves. *Progress in Oceanography* 141: 227–238. https://doi.org/10.1016/j.pocean.2015.1012.1014. Outcome of Workshop #1.

Hobday, A.J., E.C.J. Oliver, A. Sen Gupta, J.A. Benthuysen, M.T. Burrows, M.G. Donat, N.J. Holbrook, P.J. Moore, M.S. Thomsen, T. Wernberg, & Smale., D.A. 2018. Categorizing and naming marine heatwaves. *Oceanography,* 31(2): 162–173, https://doi.org/10.5670/oceanog.2018.205.

Hocken, A. G. 2000. Cause of death in blue penguins (Eudyptula m. minor) in North Otago, New Zealand. *New Zealand Journal of Zoology*, 27(4): 305–309. https://doi.org/10.1080/03014223.2000.9518239.

Huang, B., Thorne, P. W., Banzon, V. F., Boyer, T., Chepurin, G., Lawrimore, J. H., & Zhang, H.-M. 2017. Extended Reconstructed Sea Surface Temperature, Version 5 (ERSSTv5): Upgrades, Validations, and Intercomparisons. *Journal of Climate*, 30 (20): 8179-8205. https://doi.org/10.1175/jcli-d-16-0836.1.

Huang, B., Liu, C., Banzon, V., Freeman, E., Graham, G., Hankins, B., Smith, T., & H.-M. 2020. Improvements of the Daily Optimum Interpolation Sea Surface Temperature (DOISST) Version 2.1, *Journal of Climate*, 34: 2923-2939. https://doi.org/10.1175/JCLI-D-20-0166.1.

Jayne, S.R., Roemmich, D., Zilberman, N., Riser, S.C., Johnson, K.S., Johnson, K.C., & Piotrowicz, S.R. 2017. The Argo Program: present and future, *Oceanography,* 30: 18–28. https://doi.org/10.5670/oceanog.2017.213

Johnson, B., & Colombelli-Négrel, D. 2021. Breeding success in Southern Australian Little Penguins is negatively correlated with high wind speeds and sea surface temperatures. *Ornithological Applications,* 123(2021): 1-15. https://doi.org/10.1093/ornithapp/duaa062.

Kanamitsu, M., W. Ebisuzaki, J. Woollen, S-K Yang, J.J. Hnilo, M. Fiorino, and G. L. Potter, 2002. NCEP-DOE AMIP-II Reanalysis (R-2): *Bulletin of the American Meteorological Society*, 83(11), 1631-1643, doi: https://doi.org/10.1175/BAMS-83-11-1631 .

Kidson, E. 1935. The summer of 1934/35 in *New Zealand. New Zealand Meteorological Office Note*, 16: 1- 12.

Kidson, J.W. 2000. An analysis of New Zealand synoptic types and their use in defining weather regimes. *International Journal of Climatology*, 20 (3): 299-315. https://doi.org/10.1002/(SICI)1097-0088(20000315)20:3<299::AID-JOC474>3.0.CO;2-B

Kistler, R., Collins, W., Saha, S., White, G., Woollen, J., Kalnay, E., . . . & Fiorino M. 2001. The NCEP–NCAR 50–year reanalysis: Monthly means CD–ROM and documentation. *Bulletin of the American Meteorological Society,* 82(2): 247–268. https://doi.org/10.1175/1520-0477(2001)082<0247:TNNYRM>2.3.CO;2.

Le Bohec, C., Durant, J. M., Gauthier-Clerc, M., Stenseth, N. C., Park, Y. H., Pradel, R.,Grémillet, D., Gendner, J. P., & le Maho, Y. 2008. King penguin population

threatened by Southern Ocean warming. *Proceedings of the National Academy of Sciences*, 105(7): 2493–2497. https://doi.org/10.1073/pnas.0712031105.

López-Legentil, S., Song, B., Mcmurray, S.E. & Pawlik, J.R., 2008. Bleaching and stress in coral reef ecosystems: hsp70 expression by the giant barrel sponge *Xestospongia muta*. *Molecular Ecology*, 17(7): 1840-1849.

MacLean, H. 2019. Seabirds swarm as shoals of fish beach. *Otago Daily Times* 12 December 2019. https://www.odt.co.nz/regions/north-otago/seabirds-swarm-shoals-fish-beach.

McLuskie, M. (2023). *Kororā/Little Blue Penguin Project: Current Trends and Key Threats*. Western Bay Wildlife Trust (Mount Maunganui Little Blue Penguin (*Eudyptula minor*) Colony (westernbaywildlife.nz)).

McMillan, P.J, Francis, M.P, James, G.D, Paul, L.J, Marriott, P, Mackay, E, Wood, B.A, Stevens, D.W, Griggs, L.H, Baird, S.J, Roberts, C.D, Stewart, A.L, Struthers, C.D & Robbins, J.E. 2019. *New Zealand fishes. A field guide to common species caught by bottom, midwater, and surface fishing*. New Zealand Aquatic Environment and Biodiversity Report No. 208.

McMurray, S.E., Blum, J.E., Leichter, J.J. & Pawlik, J.R., 2011. Bleaching of the giant barrel sponge *Xestospongia muta* in the Florida Keys. *Limnology and Oceanography*, 56(6): 2243-2250.

Madec, G., Bourdallé-Badie, R., Bouttier, P. A., Bricaud, C., Bruciaferri, D., Calvert, D., et al. 2017. *NEMO Ocean Engine.*

Marlow, J., Davy, S.K., Shaffer, M., Haris, A. & Bell, J.J., 2018. Bleaching and recovery of a phototrophic bioeroding sponge. *Coral Reefs,* 37(2): 565-570.

Marshall, G.J. 2003. Trends in the southern annular mode from observations and reanalyses. *Journal of Climate*, 16: 4134–4143. https://doi.org/10.1175/1520-0442(2003)016<4134:TITSAM>2.0.CO;2.

Ministry for the Environment & Stats NZ 2019. New Zealand's Environmental Reporting Series: *Environment Aotearoa 2019*. https://environment.govt.nz/assets/Publications/Files/environment-aotearoa-2019.pdf.

Molitor, D., & Junk, J. 2019. Climate change is implicating a two-fold impact on air temperature increase in the ripening period under the conditions of the Luxembourgish grapegrowing region. *Oeno-one*. 3: 409-422. https://doi.org/10.20870/oeno-one.2019.53.3.2329.

Mullan, A.B., Stuart, S.J., Hadfield. M.G., Smith, M.J. 2010. *Report on the Review of NIWA's 'Seven-Station' Temperature Series* NIWA Information Series No. 78. 175 pp. https://www.niwa.co.nz/sites/niwa.co.nz/files/import/attachments/Report-on-the-Review-of-NIWAas-Seven-Station-Temperature-Series_v3.pdf.

Mullan, A.B., Sood, A., Stuart, S. 2016. *Climate Change Projections for New Zealand: Atmosphere Projections Based on Simulations from the IPCC Fifth Assessment*, Wellington: Ministry for the Environment. https://www.mfe.govt.nz/sites/default/files/media/Climate%20Change/Climate-change-projections-2nd-edition-final.pdf.

Oliver, E.C.J., Benthuysen, J.A., Bindoff, N.L., Hobday, A.J., Holbrook, N.J., Mundy, C.N., & Perkins-Kirkpatrick, S.E. 2017. The unprecedented 2015/16 Tasman Sea marine heatwave. *Nature Communications*, 8: 16101 https://doi.org/10.1038/ncomms16101.

Oliver, E. C., Benthuysen, J. A., Darmaraki, S., Donat, M. G., Hobday, A. J., Holbrook, N. J., et al. 2021. Marine heatwaves. *Annual Review of Marine Science*. 13: 313–342. https://doi.org/10.1146/annurev-marine-032720-095144.

Oliver, E.C.J., Donat, M.G., Moore, P.J., Smale, D.A., Alexander, L.V., Benthuysen, J.A., Feng, M., Gupta, A.S., Hobday, A.J., Holbrook, N.J., PerkinsKirkpatrick, S.E., Straub, S.C., & Wernberg, T. 2018. Longer and more frequent marine heatwaves over the past century. *Nature Communications,* 9: 1324 https://doi.org/10.1038/s41467-018-03732-9.

Parker, A., Garcia de Cortazar-Atauri, I., Chuine, I., Barbeau, G., Bois, B., Boursiquot, J-M., Cahurel, J-Y., Claverie, M., Dufourcq, T., Geny, L., Guimberteau, G., Hofmann, R.W., Jacquet, O., Lacombe, T., Monamy, C., Ojeda, H., Panigai, L., Payan, J-C., Lovelle, B.R., Rouchaud, E., Schneider, C., Spring, J-L., Storchi, P., Tomasi, D., Trambouze, W., Trought, M. & van Leeuwen, C. 2013. Classification of varieties for their timing of flowering and véraison using a modelling approach: A case study for the grapevine species *Vitis vinifera L. Agricultural and*

Forest Meteorology, 180: 249-264. http://dx.doi.org/10.1016/j.agrformet.2013.06.005.

Parker, A.K. 2012. Modelling phenology and maturation of the grapevine *Vitis vinifera* L.: *Varietal differences and the role of leaf area to fruit weight ratio manipulations* Lincoln University PhD thesis, Lincoln University.

Parliamentary Commission for the Environment 2019. *Focusing Aotearoa New Zealand's environmental reporting system*. ISBN 978-0-947517-17-5

Perkins, N.R., Monk, J., Soler, G., Gallagher, P. & Barrett, N.S 2022. Bleaching in sponges on temperate mesophotic reefs observed following marine heatwave events. Climate Change Ecology, 3: 100046.

Perkins-Kirkpatrick, S.E., King, S.E., Cougnon, A.D., Grosese, E.A., Oliver, M.R., Holbrook, N.J., Lewis, S.C., & Pourasghar, F 2019. The role of natural variability and anthropogenic climate change in the 2017/18 Tasman Sea marine heatwave. *Bulletin of American Meteorological Society,* 100: S105-110 http://doi.org/10.1175/BAMS-D-18-0116.1.

Ratz, H. (2022). Pers. comm.

Roberts, C., Stewart, A.L., & Struthers, C. D. 2015. *The fishes of New Zealand*. Wellington, Te Papa Press, 2008 pp.

Saha, S. et al 2006. The NCEP climate forecast system. *Journal of Climate* 19: 3483–3517. https://doi.org/10.1175/JCLI-D-12-00823.1.

Salinger, M. J. 1979. New Zealand climate: the temperature record, historical data and some agricultural implications. *Climatic Change*, 2: 109-126. https://doi.org/10.1007/BF00133218.

Salinger, M.J., Diamond, H.J., & Renwick, J.A. 2020. Surface temperature trends in New Zealand and surrounding oceans 1870 – 2019. *Weather and Climate*, 40: 32-50.

Salinger, M.J., McGann, R.P., Coutts, L., Collen, B., & Fouhy, E. (1992). *South Pacific historical climate network. Temperature trends in New Zealand and outlying islands*, 1920-1990. New Zealand Meteorological Service, 46pp, Wellington. ISBN 0-477-01598-0.

Salinger, M.J., Diamond, H.J., Behrens, E., Fernandez, D., Fitzharris, B.B., Herold, N., Johnstone, P., Kerckhoffs, H., Mullan, A.B., Parker, A.K., Renwick, J.A., Schofield, C., Siano, A., Smith, R.O., South, P., Sutton, P.J. Teixeira E., Thomsen, M.S, & Trought, M.C.T. 2020. Unparalleled coupled ocean/atmosphere summer heatwaves in the New Zealand region: Drivers, mechanisms and impacts. *Climatic Change*, 162: 485–506. https://doi.org/10.1007/s10584-020-02730-5.

Salinger, J., Hobday, A.J., Matear, R.J., O'Kane, T.J., Risbey, J.S., Dunstan, P., Eveson, J.P., Fulton, E.A., Feng, M., Plagányi, É.E., Poloczanska, E.S., Marshall, A.G. and Thompson, P.A. 2016. Decadal-Scale Forecasting of Climate Drivers for Marine Applications. *Advances in Marine Biology* 74: 1-68. https://doi.org/10.1016/bs.amb.2016.04.002

Salinger, M.J., Renwick, J.A., Behrens, E., Mullan, A.B., Diamond, H.J., Sirguey, P., Smith, R.O., Trought, M.C.T., Alexander, L.V., Cullen, N.C., Fitzharris, B.B., Hepburn, C.D., Parker, A.K., & Sutton, P.J. 2019a. The unprecedented coupled ocean-atmosphere summer heatwave in the New Zealand region 2017/18: Drivers, mechanisms and impacts. *Environmental Research Letters*, 14 (4). https://doi.org/10.1088/1748-9326/ab012a.

Salinger, M.J., Fitzharris, B., Chinn, T., & Willsman, A. 2019b. Climate forcing of glacier volume change in the Southern Alps of New Zealand, *International Journal of Climatology*, 39(11): 4274-4287. https://doi.org/10.1002/joc.6072.

Salinger, M. J., Fitzharris, B. B., & Chinn, T. 2021. Extending end-of-summer-snowlines for the Southern Alps glaciers of New Zealand back to 1949 (2021). *International Journal of Climatology*, 41 (13):, 6122-6132. https://doi.org/10.1002/joc.7177.

Seneviratne, S.I., Zhang, Adnan, M., Baldi, W., Dereczynski, C., Di Luca, A., Ghosh, S., Iskandar, I., Kossin, J., Lewis, S., Otto, F., Pinto, I., Satoh, M., Vicente-Serrano, S.M., Wehner, M., & B. Zhou, 2021: Weather and Climate Extreme Events in a Changing Climate. In *Climate Change 2021: The Physical Science Basis. Contribution of Working Group I to the Sixth Assessment Report of the Intergovernmental Panel on Climate Change*, edited by Masson-Delmotte, V., P. Zhai, A. Pirani, S.L. Connors, C. Péan, S. Berger, N. Caud, Y. Chen, L. Goldfarb, M.I. Gomis, M. Huang, K. Leitzell, E. Lonnoy, J.B.R. Matthews, T.K. Maycock, T. Waterfield, O. Yelekçi, R. Yu, & B. Zhou. Cambridge, United Kingdom and New York, Cambridge University Press: 1513–1766, https://doi.org/10.1017/9781009157896.013.

Smale, D.A., Wernberg, T., Oliver, E.C.J., Thomsen, M., Harvey, B.P., Straub, S.C., Burrows, M.T., Alexander, L.V., Benthusen, J.A., Donat, M, Feng M, PerkinsKirkpatrick, S.E., Scannell, H.A., Sen Gupta, A., Payne, B.L., & Moore, P.J. 2019. Marine heatwaves threaten global biodiversity and the provision of ecosystem services. *Nature Climate Change*, 9: 306–312 https://doi.org/10.1038/s41558-019-0412-1.

Srinivasan, R., Carey-Smith, T., & Macara, G. 2021. Trend analysis on frequency of New Zealand climate extremes. *Weather and Climate*, 41 (1): 18-29.

Stahel, C & Gales, R. 1991. *Little penguins: fairy penguins in Australia*. University if New South Wales, Kensington, NSW: 115 pp.

Staudt, G. 199). Opening of flowers and time of anthesis in grapevines, *Vitis vinifera*, L. Vitis 38(1): 15-20.

Storkey, D., Blaker, A. T., Mathiot, P., Megann, A., Aksenov, Y., Blockley, E. W., Calvert, D., Graham, T., Hewitt, H. T., Hyder, P., Kuhlbrodt, T., Rae, J. G. L., & Sinha, B. 2018. UK Global Ocean GO6 and GO7: a traceable hierarchy of model resolutions, *Geoscientific Model Development*, 11: 3187–3213, https://doi.org/10.5194/gmd-11-3187-2018, 2018.

Stevens, C. L., O'Callaghan, J. M., Chiswell, S. M. & Hadfield, M. G. 2021. Physiological oceanography of New Zealand/Aotearoa shelf seas – a review. *New Zealand Journal of Marine and Freshwater Research* 55 (1): 6-45. https://doi.org/10.1080/00288330.2019.1588746.

Sutton, P. J. H. 2003. The Southland Current: a subantarctic current. *New Zealand Journal of Marine and Freshwater Research* 37: 645-652.

Sutton, P.J., Bowen, M. 2019. Ocean temperature change around New Zealand othe last 36 years. *New Zealand Journal of Marine and Freshwater Research* 53 (3): 305-326. https://doi.org/10.1080/00288330.2018.1562945.

Tait, L.W., Thoral, F., Pinkerton, M.H., Thomsen, M.S. and Schiel, D.R., 2021. Loss of giant kelp, Macrocystis pyrifera, driven by marine heatwaves and exacerbated by poor water clarity in New Zealand. *Frontiers in Marine Science*, 8: 1-15. https://doi.org/10.3389/fmars.2021.721087

Thompson, D. W. J., Solomon, S., Kushner, P. J., England, M. H., Grise, K. M., & Karoly, D. J. (2011). Signatures of the Antarctic ozone hole in Southern Hemisphere surface climate change. *Nature Geoscience* 4(11), 741-749. https://doi.org/10.1038/NGEO1296.

Thomsen, M.S., Mondardini, L., Alestra, T., Gerrity, S., Tait, L., South, P.M., Lilley, S.A. and Schiel, D.R., 2019. Local extinction of bull kelp (Durvillaea spp.) due to a marine heatwave. *Frontiers in Marine Science*, 6, p.84. https://doi.org/10.3389/fmars.2019.00084.

Thoral, F., Montie, S., Thomsen, M.S., Tait, L.W., Pinkerton, M.H. and Schiel, D.R., 2022. Unravelling seasonal trends in coastal marine heatwave metrics across global biogeographical realms. *Scientific reports*, 12: 7740. https://doi.org/10.1038/s41598-022-11908-z

Trenberth, K.E. 1976. Fluctuations and trends in indices of the southern hemispheric circulation. *Quarterly Journal of the Royal Meteorological Society*, 102 (431): 65-75. https://doi.org/10.1002/qj.4971024310.

Trenberth, K.E., Zhang, Y., Fasullo, J.T., Cheng, L. 2019. Observation-Based Estimates of Global and Basin Ocean Meridional Heat Transport Time Series. *Journal of Climate*, 32: 4567-4583. https://doi.org/10.1175/JCLI-D-18-0872.1.

Trought, M.C.T. 2005. Fruitset - possible implications on wine quality. In: *Transforming flowers to fruit. Mildura, Australia: Australian Society of Viticulture and Oenology*, edited by Garis, K. D., Dundon, C., Johnstone, R. & Partridge, S., Australian Society of Viticulture and Oenology, Mildura, Australia: 32-36.

Troup, A.J. 1965. The 'southern oscillation'. *Quarterly Journal of the Royal Meteorological Society*, 91 (390): 490-506 https://doi.org/10.1002/qj.49709139009.

Tsujino, H., et al. 2018. JRA-55 based surface dataset for driving ocean–sea-ice models (JRA55-do). *Ocean Modelling*, 130 (October 2018): 79-149. https://doi.org/10.1016/j.ocemod.2018.07.002.

Zhao, Z., & Marim, M. 2019. A MATLAB toolbox to detect and analyze marine heatwaves. *Journal of Open Source Software* 4(33): pp.1124, https://doi.org/10.21105/joss.01124.

Time series of relative humidity, wet-bulb temperature, and dewpoint temperature at Kelburn and Masterton over the last 90 years

Richard Turner[1], Katie Baddock[2], John-Mark Wooley[2], Petra Pearce[2], Alex Pezza[3,4], Amir Pirooz[2]

[1] National Institute of Water and Atmospheric Research (NIWA), Wellington, New Zealand
[2] NIWA, Auckland, New Zealand
[3] Greater Wellington Regional Council; Te Pane Matua Taiao, Wellington, New Zealand
[4] Adjunct Research Associate, School of Geography, Environment and Earth Sciences, Victoria University of Wellington, New Zealand
Corresponding author: Richard Turner, richard.turner@niwa.co.nz

ABSTRACT

NIWA has recently digitised daily wet- and dry-bulb temperature records for both Kelburn, Wellington and Masterton, Wairarapa sites back to 1929 and undertaken an analysis of these records and comparison with reanalysis products. This article presents key results of the analysis in the context of climate change and also the steps taken to account for site moves, complications around a plethora of daylight savings changes, and observing methods.

Overall, there was a 0.7°C increase in dewpoint temperature (T_d) averaged over all seasons with the strongest trend being an increase in winter, amounting to +1.7°C over 90 years at Kelburn, and +1.8°C at Masterton for the same period. Autumn also saw increasing trends at both locations whereas summer and spring saw smaller increases.

Other points of interest were that January 2018 had the highest average T_d values of any month in both the Kelburn and Wairarapa records while February 1998 was ranked third in the Kelburn record. Both 1998 and 2018 are tied for third-warmest years on record for Aotearoa New Zealand (dry-bulb air temperature).

Despite the long-term upward trend, average T_d values for February 1938 and February 1935 were ranked second- and tenth-highest respectively in the Kelburn record. February 1935 is also ranked eighth-highest in the Wairarapa record.

Extreme high summer and autumn values of T_d occurred in the 1930s where there was considerable year-to-year variability.

Of the ten months with lowest average T_d values, seven occurred in the 1930s and 1940s for Wellington. At Masterton, six were in the 1930s and all ten had occurred by 1972.

1. INTRODUCTION

Wet-bulb temperature, dewpoint temperature and relative humidity are all important measures of the moisture content of air-mass characteristics. In terms of applied meteorological and climate applications these are perhaps most meaningful when combined with other parameters such as dry-bulb temperature to provide apparent temperature (heat indices), e.g., where high humidity and high temperatures are uncomfortable for humans or livestock as it limits the ability to regulate the cooling of the body. Physically,

dewpoint temperature is, in the absence of a change of air-mass, often a useful indicator of what the overnight temperatures may drop to and when high in the summer is associated with sub-tropical air-masses and so can be used to assess climatic risk of spread of some potentially invasive insect pests from warmer climates, e.g., Red Imported Fire Ant (Turner et al., 2006). Extended periods of high relative humidity correlate well to leaf wetness and are used to assess the infection risk for plant diseases such as Myrtle Rust (Beresford et al., 2018). High duration humidity events are also associated with increased rates of corrosion (Schindelholz and Kelly, 2010). Low dewpoint temperatures near zero or below will also be associated with frost occurrence and extended periods of low-humidities in warmer months are associated with drought risk.

It is therefore of interest, especially in the light of the warming experienced under climate change, to investigate long-term trends in wet-bulb temperature, dewpoint temperatures and relative humidity in Aotearoa-New Zealand, where little if any work appears to have been done with surface records prior to 1972. Where most records are not available digitally, there also appears to be little done post-1972 with the moisture variables as well. In this paper, we present the results from an effort to reconstruct a 90-year record from two New Zealand climate stations; Kelburn, Wellington and Masterton, Wairarapa in the Greater Wellington Region of the lower North Island, see Figure 1.

2. DATA AND METHODS

2.1 Data

In New Zealand, historic climate records relating to moisture content of air masses (i.e., relative humidity (RH), dewpoint temperature (T_d), and wet-bulb Temperature (T_w)) are typically only available from daily 9am observations prior to 1972. Three hourly (or synop) records are commonly available from 1972 and hourly records of these variables are more commonplace from the early 1990s with the introduction of automated weather stations (AWS). Typically, only one of the three variables (RH, T_d, T_w) was reported. This is because when one of these is known along with the dry-bulb air temperature (T_a) (which is almost always reported), the other two variables can be reasonably determined. Abbot and Tabony (1985), Alduchov and Eskridge (1996), August (1828), Magnus (1844), and Stull (2011) provide background and various methods to do these calculations. Additionally, there are online calculators and resources which can be utilised to do these conversions. A listing of some of these sites is provided within the reference section, see Australian BOM, McNoldy, 2020 and Omni, 2020 websites.

A survey of NIWA station histories (Fouhy et al., 1992) and New Zealand's national climate database (CliDB) identified that for Wellington the Kelburn site could be used to derive moisture-related trends as 9am records there

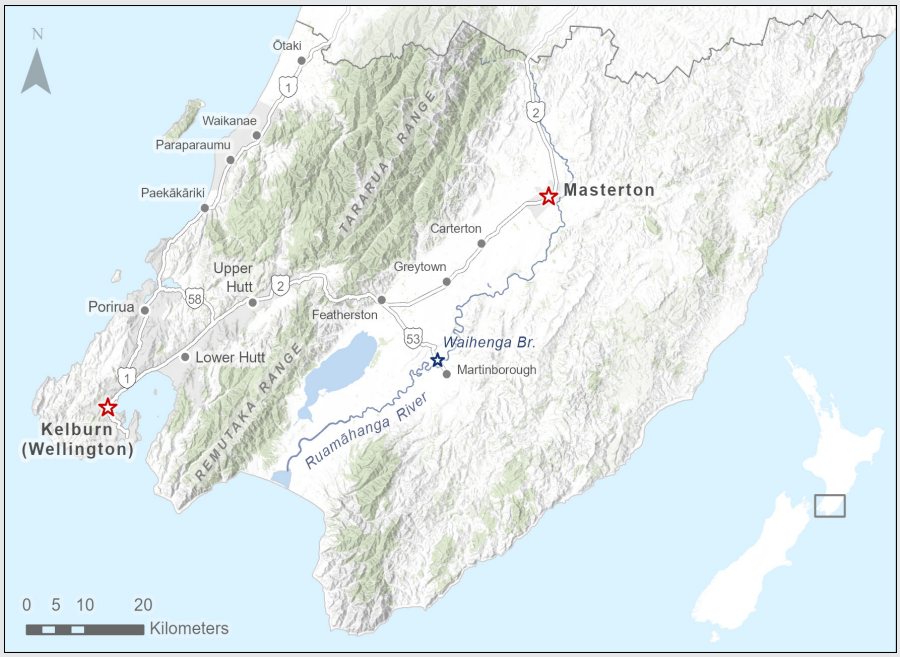

Figure 1: Map of the Wellington Region, Aotearoa-New Zealand, showing location (red stars) of Kelburn (in Wellington) and Masterton. The location of the Ruamāhanga River site at Waihenga Bridge (blue star) is also indicated.

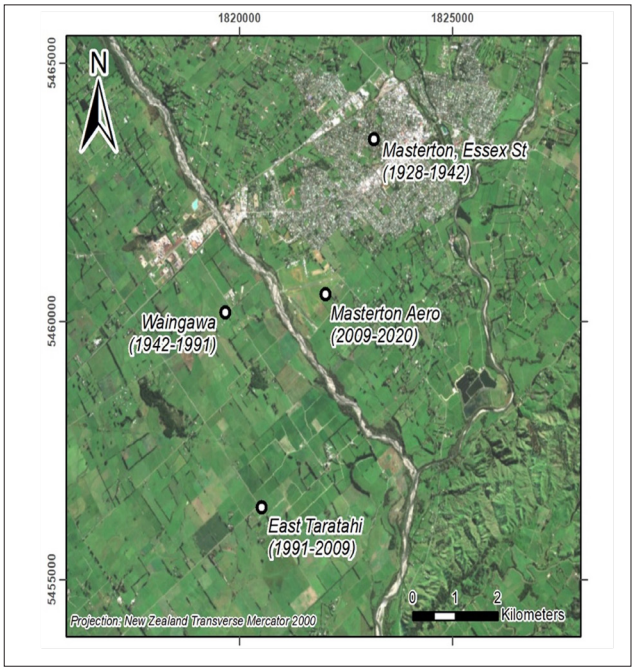

Figure 2: Map showing location of Masterton climate stations with records used in the dewpoint temperature analysis.

average (6.79g/kg) at Masterton where the average 9am value was 7.09g/kg.

Digitisation, and quality control of records prior to 1972 was also required and done for this analysis. The data rescue process involved studying original meteorological forms which keep track of manually transcribed weather observations. These observations were manually typed into Excel documents, focusing on one column of data at a time. Each observation's column of data concluded with a 'Sums' and 'Means' option which have also been manually recorded. To ensure accuracy in digitizing the records, each column was added up using the excel 'Sum' feature to make sure the column's total matched that of the original document. This ensured the observations had been recorded accurately, despite the handwriting of some of the numbers making it difficult to read.

Some numbers that were particularly difficult to make out were determined by looking at the numbers recorded before and after them, which gave an indication of the figure likely recorded in the space.

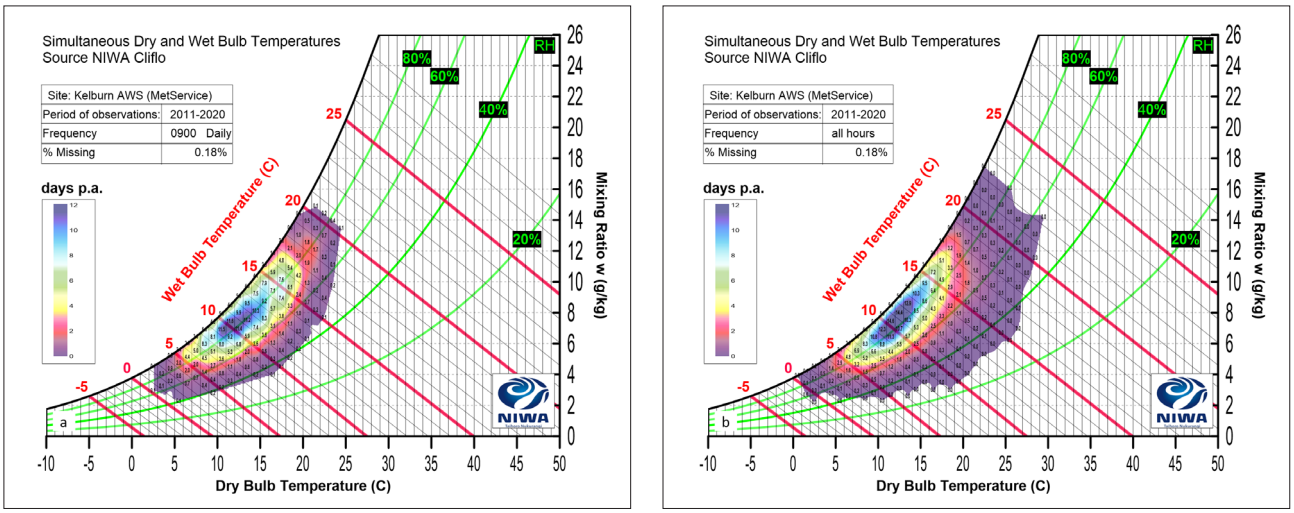

Figure 3: Distribution for period 2011-2020 at Kelburn for which various dry-bulb temperature and Mixing Ratio combinations for (left) 9am (expressed as days per year) and (right) for all hours.

go back to late-1928, and that a collection of sites could be used for Masterton (see Table 1 and Figure 2). The choice of 9am was primarily due to the fact that the longest available records are for this time. The 9am records still give a reasonable distribution of overall air-mass properties compared to distributions for all hours, see (Figure 3) which compares Kelburn "9am only" to "all-hours" psychrometric charts over the past decade. In terms of mixing ratios average diurnal variations, over the last decade, at Kelburn were within ±3% of the average (7.46g/kg) with the average 9am value being 7.53g/kg and were within ±9% of the

Most of the original meteorological forms however were able to be read with ease (see Figure 4), and the sums calculated by the recorder were an added benefit for the digitization process. Quality control also consisted of visual inspection of records checking for obviously spurious values, unphysical values, e.g., when dewpoint or wet-bulb temperatures exceeded dry-bulb air temperatures, and also the conversion from Fahrenheit to Celsius when required. Prior to automated stations the observing method typically involved the observer recording the dry-bulb temperature and wet-bulb temperature then using psychrometric tables

Station Name	Begin Date (analysis)	End Date (analysis)	Comment
Wairarapa			
Masterton, Essex St	2-Sep-1928	30-Nov-1942	Digitized from paper records
Masterton Waingawa	2-Jan-1943	31-Dec-1971	Digitized from paper records
Masterton Waingawa	1-Jan-1972	31-Mar-1991	8am records in NZDT 1974 – 1991
East Taratahi[1,2]	28-Oct-1991	4-Nov-2009	8am records in NZDT 1991 - 1995
Masterton Aero AWS	5-Nov-2009	25-Mar-2020	
Wellington			
Kelburn[3]	1-Dec-1928	30-Jan-1961	Digitized from paper records
Kelburn[4,5]	1-Dec-1961	1-Sep-2005	8am records in NZDT 1989 – 2004
Kelburn AWS	2-Sep-2005	25-Mar-2020	

Table 1: Listing of climate stations where 9am (NZST) temperature and humidity records were obtained for this section.

[1] Dec 1996: Stevenson Screen Replaced
[2] May 2001: Humidity Probe replaced due to overheating
[3] Jul 1949: Exposure increased and improved.
[4] Apr 1970: Equipment replaced due to vandalism
[5] Dec 1989: Thermometer replaced

(also known as hygrogmetric tables as published by the Smithsonian Institute (1939)) or charts (similar to that of Figure 3) to determine relative humidity and dewpoint temperature. Either aspirated thermometers or at times a sling psychrometer were used to determine the wet-bulb temperature by a trained observer.

2.2 Methods

One complication in creating a "9am" record is that local time records were the only ones available, a complicated sequence of daylight savings periods and changes had to be accounted for. This meant that there were periods when 8 am New Zealand Standard Time (NZST) records were only available. To account for this, regression relationships between 8am and 9am NZST observations were developed from nearby stations where, or from a later period, when hourly observations were available, and adjustments made. Key details about the regression relationships and the periods for which these were applied in the adjustments are provided in Table 2.

Another aspect related to daylight savings that had to be accounted for was that the current NZST was adopted in 1941. In the period 1927-1941 New Zealand did have daylight savings in the summer months and in 1941 this daylight savings time was adopted all-year round and became the current NZST. The old standard time (NZMT)

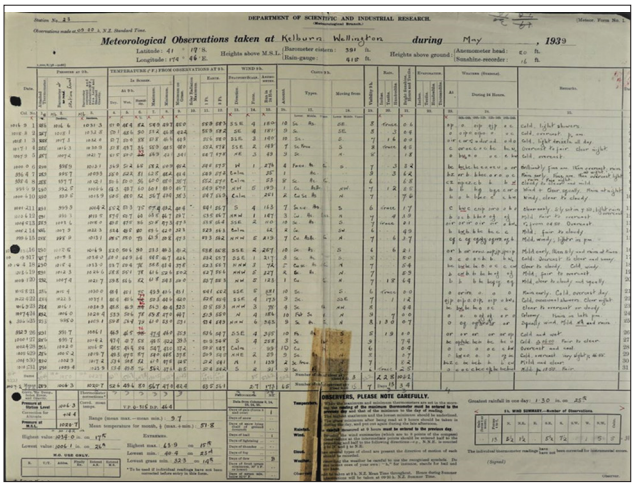

Figure 4: Capture of a typical observation chart with recordings taken at Kelburn, Wellington in May of 1939.

between 1927 and 1941 was 30 minutes behind our current NZST or +11:30 ahead of UTC. The period of daylight savings from 1928 to 1933 was from the 2nd Sunday in October to the 3rd Sunday in March and from 1933 to 1941 it was from the 1st Sunday in September until the last Sunday in April. Adjustments were thus also made to account for the half-hour shift during the period of NZMT. This adjustment resulted in a decrease of average summer dew-point temperatures in the 1930s of around 1°C at Masterton, but only a slight decrease of around 0.1°C at Kelburn. We suggest this difference could be due to maritime influences damping the diurnal cycle at Kelburn as it is much closer to the ocean.

Apart from the adjustments for time-of-observation, and applying corrections where there was some overlap of stations, little other effort was made to homogenise the data. No attempt was made to apply the methods of Rhoades and Salinger (1993) to account for site changes or detected breakpoint changes. This is because the Rhoades and Salinger method requires other coincident time-series of a parameter to be available at 'nearby' stations to check on consistency of trends when a site change occurs. The digitization of the Masterton and Kelburn records done here is to the author's knowledge the first to be done for New Zealand for dewpoint and wet-bulb temperatures, and relative humidity and so clearly application of the method is not possible currently, but clearly should be part of future work when other early station humidity records are digitized. Such work would help identify other causes of inhomogeneity such as screen and instrumentation maintenance which is important as the wick for wet-bulb temperatures needs to be well-maintained. The work on homogenisation was hampered by a lack of available detail in maintenance records prior to 1972.

Brown and DeGaetano (2009) describe a method to detect inhomogeneities in historical dewpoint temperature series, but their method relies on hourly records being available, which were not in this record prior to 1991.

Potential breakpoints were identified via a breakpoint detection algorithm similar to that used in Turner et. al., 2019. Only one significant breakpoint was detected for Kelburn and that was in 2012 and does not appear to be associated with any recorded issues with instrument or site maintenance. There were several statistically significant breakpoints detected for Masterton. These were in October 1937, May 1938, June 1975, June 1988, August 1990, December 1993, and August 2017 – some of which are close to breaks in the station records.

		T_a			T_w		
Station	**Years**	**slope**	**intercept**	**r 2**	**slope**	**intercept**	**r 2**
East Taratahi	1995-2009	0.9180	2.7207	0.926	0.8571	2.6097	0.929
Masterton AWS	2009-2020	0.9198	2.8088	0.925	0.8562	2.6016	0.938
Kelburn	1972-1988	1.0231	0.3251	0.943	0.9593	0.7802	0.958
Kelburn AWS	2004-2020	0.9839	1.0393	0.949	0.9578	0.9370	0.968
		RH			**T_d**		
		slope	**intercept**	**r 2**	**slope**	**intercept**	**r 2**
East Taratahi	1995-2009	1.0051	-5.1407	0.812	0.8295	2.1485	0.897
Masterton AWS	2009-2020	0.9753	-4.1650	0.811	0.8410	1.8891	0.907
Kelburn	1972-1988	0.8504	10.2570	0.591[1]	0.8991	1.0695	0.899
Kelburn AWS	2004-2020	1.0122	-4.2783	0.834	0.9671	0.4719	0.959

Table 2: Regression relationships and correlations between 8am and 9am temperature and humidity variables for stations where hourly records available. T_a = dry bulb air temperature, T_w = wet-bulb air temperature, RH = relative humidity, T_d = dewpoint temperature. The dependent variable is 9am NZST reading when the 9am NZDT (or 8am NZST) was available.

[1] The lower correlation between 8am and 9am RH at Kelburn is suspected to be due to different precisions in reported values at these times of the day.

Season	Change between 1929 and 2019			
	T_d (°C)	RH (%)	T_a (°C)	T_w (°C)
Summer	+0.4	+0.4	+0.3	+0.3
Autumn	+0.8	+2.1	+0.3	+0.6
Winter	+1.7	+3.6	+0.9	+1.2
Spring	+0.1	+0.1	+0.1	+0.1

Table 3: Change in average seasonal values in "9am" dewpoint temperature (T_d), Relative Humidity (RH), dry-bulb air temperature (T_a) and wet-bulb air-temperature (T_w) for the Kelburn, Wellington site between 2019 and 1929. This is regression based with starting and end years being 1929 and 2019. Note: summer averages start in 1928.

3. RESULTS

In this section key results and trends are presented for Kelburn and then for Masterton.

3.1 Wellington

Time series of average values for each season (summer, autumn, winter, and spring) for each year from 1929 to 2019 for Kelburn for RH, T_a, T_w, and T_d. are shown in Figure 5. Potential breakpoints in the time-series due to an exposure change in 1949 and the station change in 2004 and those indicated by the detection algorithm are indicated in these figures. Minor bias corrections downwards of around -0.2°C were made to the Kelburn AWS dewpoint temperature post 2005 based on the short period of overlap when the previous Kelburn station remained operating. While this section is focused on trends and extremes in dewpoint temperatures, the other variables are presented also as a check on consistency and to aid physical interpretation. The other point to note about the other variables is that the dry-bulb air temperatures (T_a) are 9am temperatures and so trends and rankings presented here will not precisely match those of daily maximum, minimum or average temperatures such as NIWA's Seven Station Series (Mullan et. al., 2012) derived elsewhere, but should be consistent.

From these seasonal plots, it is apparent that the year-to-year variation and longer-term trends (from simple linear regression relationships) in T_a, T_w, and T_d are all very similar between season and consistent among the variables (Table 3). Overall, the trend in winter is strongest with an approximate increase in 9am dewpoint temperatures of 1.7°C over the 90 years, and an increase in RH of around 3.6% over the period. For autumn there is also an increase of around 0.8°C in T_d and around 2.1% in RH, and for summer these increases are 0.4°C and 0.4%. Meanwhile, for spring the increases to T_d and RH are 0.1°C and 0.1% respectively. The increases in RH are interesting since RH decreases as dry-bulb temperature increases (if all other air-mass parameters remain unchanged) and so it appears that in this instance, increases to dewpoint temperature are more influential than the increases in dry-bulb air temperature in determining the trend in RH. It is noted that there is a sudden increase in RH during summer between 1990 and 2004 which does not occur for the other seasons (Figure 5), and this appears consistent with the observed temperature changes at the time (which show a drop in 9am temperatures). While no information in the station histories was found that indicated any technical issues with instruments during this period, it is noted that the end of the period aligns with a station change and it is therefore possible that there could still be some underlying data issues during this period.

The top-ten and bottom-ten ranked months for average dew-point temperatures were tabulated and these showed that January 2018 had the highest average T_d values of 16.6°C and February 1998 was ranked third, where these two years are tied for second-warmest years for Aotearoa-New Zealand (according to NIWA's Seven Station Series). Also interesting is that, in spite of the long-term upward trend, February 1938 (2nd) and February 1935 (10th) were ranked within the top ten. In terms of bottom ranked years, seven of the ten months occurred in the 1930s and 1940s. Another way to visualise the long-term trend is to contrast

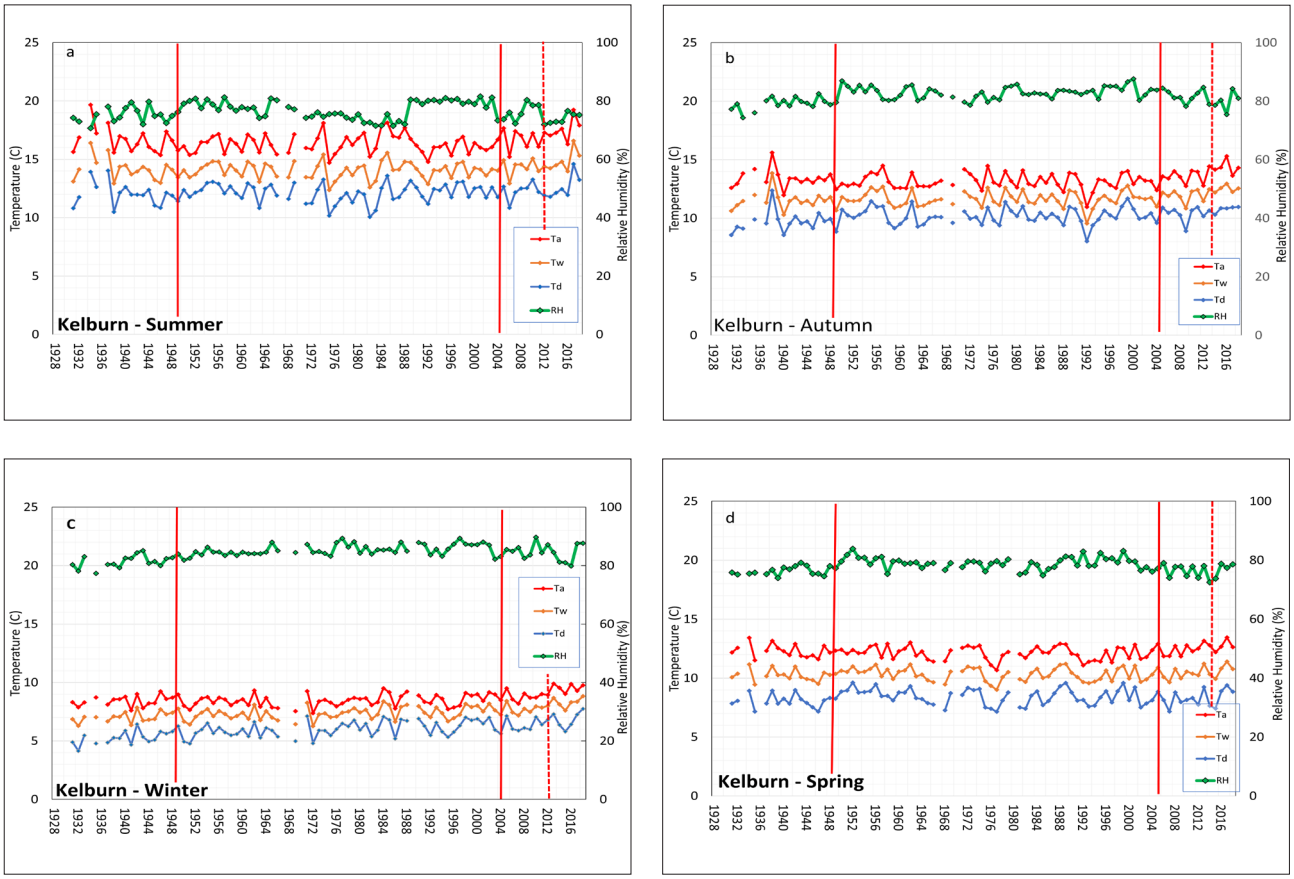

Figure 5: Time series for each season "9am" averages for dry-bulb air temperature (T_a; red-line), wet-bulb air-temperature (T_w; orange line), dewpoint temperature (T_d; blue line) and Relative Humidity (RH; green line) for the Kelburn, Wellington site for the period 1928 to 2020.The red vertical lines mark an exposure change in 1949 and the switch to records from Kelburn (CliDB agent no. 3385) to Kelburn AWS (25354) in 2004. The red-dashed line denotes the break-point as detected with the breakpoint detection algorithm.

the decades 2011-2020[1] and 1932-1940 as expressed in a psychrometric chart as in Figure 6 which shows a general warming/moistening pattern. As an example, to help interpret the plot, we see there were around three to four more days per year in 2011-2020 than 1931-1940 when 9am temperatures were around 18°C and mixing ratios around 10g/kg. Conversely, in the period 2011-2020 there were three to four fewer days where dry-bulb temperatures were around 7 °C and mixing ratios around 6g/kg.

Monthly averages, minimums, and maximum of dry-bulb air temperature (T_a), wet-bulb temperature (T_w), relative humidity (RH) and dewpoint temperature (T_d) for Kelburn are shown in Figure 7. The thick bold lines are running 12 month means of the average, minimum and maximum. Trends in the averages correspond to the overall annual trends in these values and are +0.8°C for T_a, T_w, and T_d and +1.3% for RH over the 90 years. It is gratifying to note, in Figure 7a, the consistency with the NIWA Seven Station Series average monthly temperature series with the dry-bulb temperature series given the simple nature of adjustments made here.

The ten most extreme maximum values of 9am dewpoint temperature and the dates on which these occurred are provided in Table 4 while the values of the extreme minimums and dates are provided in Table 5. The most extreme high 9am dewpoint temperature was 20.3°C on 10 March 1981. Interestingly, only the events of 18 February 1955 and 30 January 1956 occurred in months that had averages ranked in the top-ten. Extreme minimum events occurred in winter, with the record minimum of -6.8°C on 7 June 1944. Again seven of the 10 bottom ranked events occurred in the 1930s and 1940s.

It is noted that this analysis only captures extremes in "9am" dewpoint temperatures and therefore will have missed other significant observations that might have occurred at different times of the day. The maximum dewpoint temperature across the entire record for Kelburn

[1] The original time-series reconstruction was done in 2020, but the psychrometric analysis was done a year later so included the year 2020.

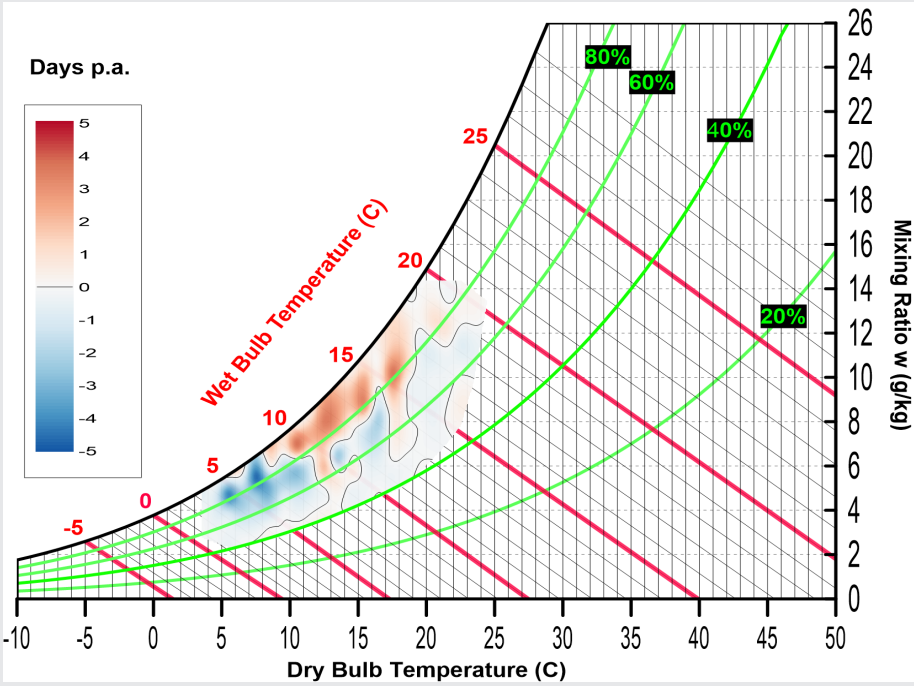

Figure 6: Colour-filled contour plot of difference (days per year) in distribution of 9am dry bulb temperatures-mixing ratio combinations for 2011-2020 versus 1931-1940 for Kelburn.

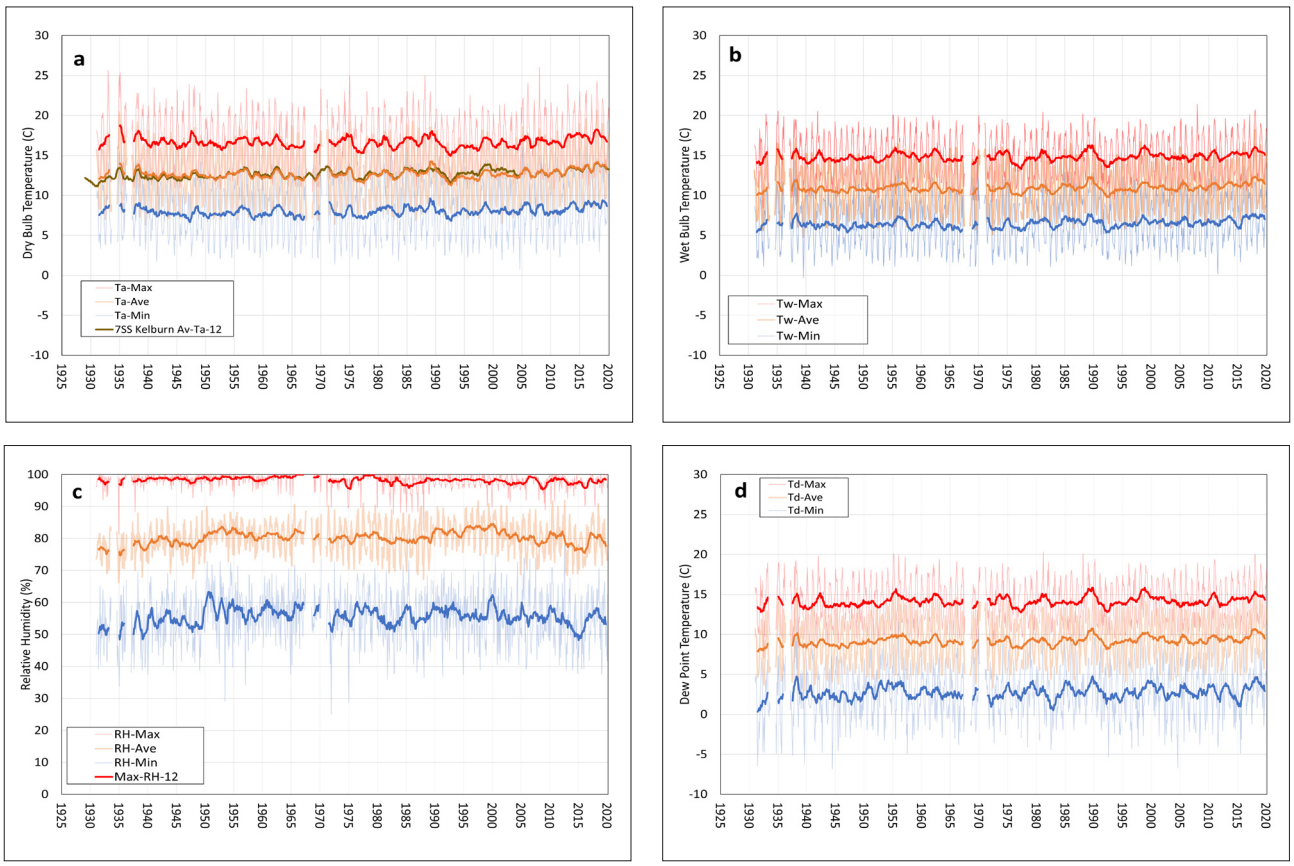

Figure 7: Monthly "9am" average (orange lines), minimum (blue), and maximum (red) time series (thin lines) of a) dry bulb air temperature (T_a) , b) wet-bulb temperature, c) relative humidity, and d) dewpoint temperature for Kelburn, Wellington for the period 1929 to 2019.The thick bold lines are running 12 month means of the average, minimum and maximum. The dark brown line in 7a is the 12-month running mean of Kelburn monthly average temperature as derived for NIWA's Seven Station Series.

Date	Rank	T_a	T_w	RH	T_d	DPP
10/3/1981	1	20.6	20.4	98.1	20.3	0.2
12/2/1988	2	20.4	20.2	98.1	20.1	0.2
18/2/1955	3	20.2	20.1	99.5	20.1	0.1
15/3/1955	4	19.9	19.9	100.0	19.9	0.0
30/1/1956	5	20.1	19.9	98.9	19.9	0.1
30/1/1942	6	21.7	20.5	89.4	19.9	1.2
4/2/1957	7	19.7	19.7	100.0	19.7	0.0
10/2/2022	-	*20.7*	*20.0*	*93.5*	*19.6*	*1.1*
10/3/1990	8	19.6	19.6	100.0	19.6	0.0
14/3/1955	9	20.2	19.8	96.3	19.6	0.4
17/2/1963	10	19.4	19.4	100.0	19.4	0.0

Table 4: Dates of extreme high values (top ten) of "9am" T_d (6th column) in the period 1928 to 2019 at Kelburn. Also listed are the values T_a, T_w, RH and dewpoint depression (DPP = T_a-T_d) on these dates.(Also listed in italics is the one occurrence since the time of analysis and submission that would be top ten).

Date	Rank	T_a	T_w	RH	T_d	DPP
7/6/1944	1	6.1	1.9	39.0	-6.8	12.9
24/8/2004	2	0.7	1.7	40.5	-6.7	7.4
5/6/1931	3	6.4	2.2	39.1	-6.5	12.1
13/8/1939	4	5.9	1.9	41.6	-6.1	12.0
27/7/1992	5	5.7	2.0	44.8	-5.4	11.1
19/7/2015	6	4.8	1.5	48.6	-5.1	9.9
7/7/1937	7	5.1	1.7	47.5	-5.1	10.2
25/8/1935	8	7.2	3.0	41.7	-4.9	12.1
2/9/1934	9	7.8	3.3	40.2	-4.9	12.7
28/7/1957	10	5.8	2.2	46.0	-4.9	10.7

Table 5: Dates of extreme low values (bottom ten) of "9am" T_d (6th column) in the period 1928 to 2019 at Kelburn. Also listed are the values T_a, T_w, RH and dewpoint depression (DPP = T_a-T_d) on these dates.

was 22.0 °C observed at 1800 NZST hours on 11 Feb 2018 (part of the notably hot and wet summer of 2018).

3.2 Wairarapa

Average values for each season (summer, autumn, winter, and spring) for each year from 1928 to 2019 for Masterton of RH, T_a, T_w, and T_d are provided in Figure 8 and changes summarised in Table 6. Potential breakpoints in the time-series due to station changes, and those identified with the breakpoint algorithm, are also indicated in these figures. Visually, there does seem to be a decline in spring and summertime relative humidity post the 1993 breakpoint and could be related to the station shift to East Taratahi. This does not appear related to changes in irrigation as acreage of land irrigation increased in the area after around 2003 (based on inspection of Google Earth aerial imagery). Unfortunately, there are no overlaps of the records when station moves occurred from which to make adjustments, so no attempts at adjustments for this period were made.

As was found for Wellington, it is apparent that the year-to-year variation and longer-term trends in T_a, T_w, and T_d are all very similar. Again, the trend in winter is strongest where there is an increase (linear regression) in 9am dewpoint temperatures of 1.8°C and an increase in winter relative humidity of around 7.2% for the 90-year period. For autumn there is also an increase of around 0.8°C in T_d and around 3.2% in RH, and for spring they are +0.4°C and +1.7% while for summer there is an increase of 0.5°C, and a small increase of 0.2% in RH. The smaller increases in summer RH are likely impacted by recent increases in T_a. It is noted, however, if records prior to 1942 are ignored due to a potential breakpoint related to the station move, the trends in T_d are +0.9°C for winter, +0.2°C for autumn, -0.4°C for summer (decrease), and -0.2°C (decrease) for spring. The trends in RH become +5.8% for winter, +2.0% for autumn, -3.9% (decrease) for summer, and -2.8% (decrease) for spring, and the trends in T_a become -0.02°C for winter, +0.05°C for spring, +0.58°C for summer, and -0.21°C for autumn.

The top-ten and bottom-ten ranked months for average dewpoint temperatures were again tabulated and as was the case for Wellington, January 2018 in Masterton had the highest average T_d values of 16.1°C. Four of the top 10 ranked months for average T_d occurred in the 1950s. Six of the bottom ranked months occurred in the 1930s and all occurred before 1972. Extreme high summer and autumn values of T_d occurred in the 1930s where there seems to be considerable year to year variability during those seasons.

Monthly averages, minimums, and maximum of dry-bulb air temperature (T_a), wet-bulb temperature (T_w), relative humidity (RH) and dewpoint temperature (T_d) for Masterton are shown in Figure 9, Figure 10, and Figure 11. Trends in the averages correspond to the overall annual trends in these values and are +0.2°C for T_a, +0.4°C T_w, and +0.7°C T_d and +3.3% for RH over the 90 years. The consistency with the Seven Station Masterton series in Figure 9a is again noted and gives confidence that the trends and variations in other variables is robust. A notable period, apparent, was the late 1970s where minimum RH (Figure 10) values below 60% were not observed and average RH was above 80%. This could be due to humid summers and autumns at this time although it is noted that this signal is not present in the Wellington record, and it corresponds with a period marked by station changes at the beginning and at the end. Additionally ERA5 reanalyses

	Change between 1928 and 2019			
Season	**T_d (°C)**	**RH (%)**	**T_a (°C)**	**T_w (°C)**
Summer	+0.5	+0.2	+0.5	+0.3
Autumn	+0.8	+3.2	-0.1	+0.3
Winter	+1.8	+7.2	0.0	+0.5
Spring	+0.4	+1.7	-0.2	+0.1

Table 6: Change in average seasonal values in "9am" dewpoint temperature (T_d), Relative Humidity (RH), dry bulb air temperature (T_a) and wet-bulb air-temperature (T_w) for the Masterton, Wairarapa site between 1928 and 2019.
Note: Autumn and winter averages started in 1929.

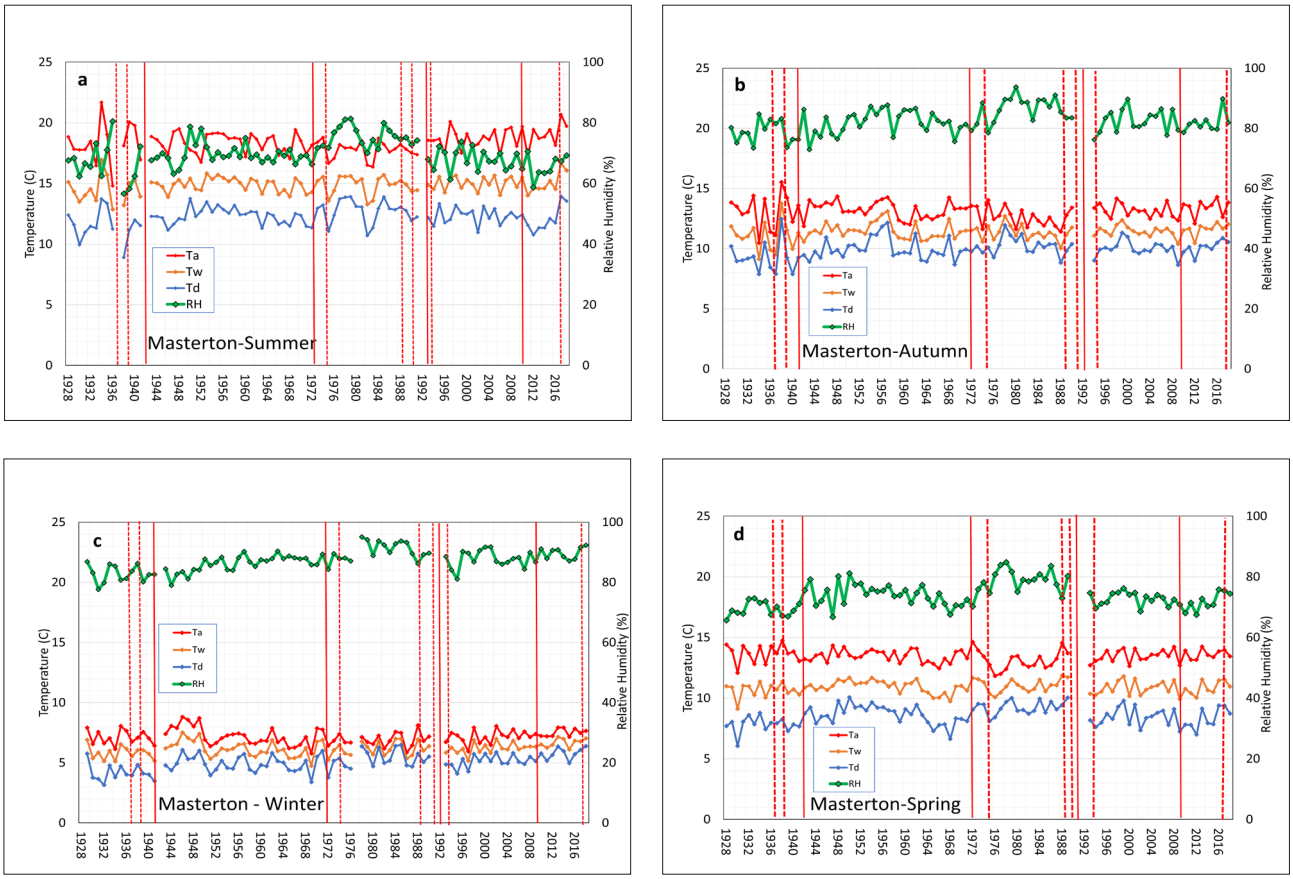

Figure 8: Time series for each season of "9am" averages for dry-bulb air temperature (T_a; red-line), wet-bulb air temperature (T_w; orange line), dewpoint temperature (T_d; blue line) and relative humidity (RH; green line) for the Masterton, Wairarapa site for the period 1928 to 2020.The red vertical lines mark station moves and red-dashed lines mark detected break points and the red line at 1972 marks the switch from earlier records recently digitized from meteorological charts to records retrieved from the national Climate Database (CliDB).

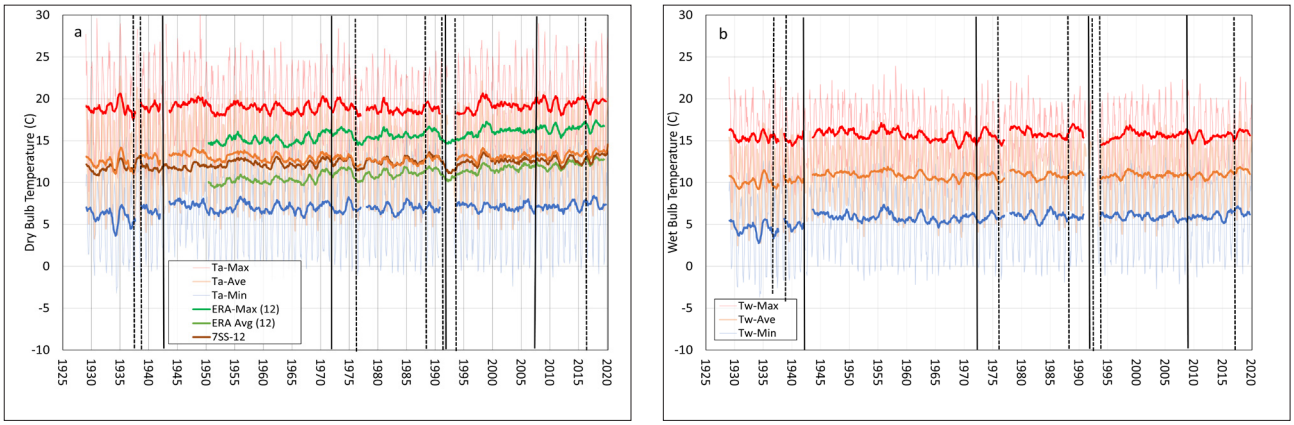

Figure 9: Monthly "9am" average (orange lines), minimum (blue lines), and maximum (red lines) time series (thin lines) of a) dry-bulb air temperature (T_a) and b) wet-bulb temperature for Masterton, Wairarapa for the period 1929 to 2019.The thick bold lines are running 12 month means of the average, minimum and maximum. Green lines are the ERA5 reanalysis for the nearest grid cell which has a higher mean orographic elevation so has a cold temperature bias. The dark brown line is the 12-month running mean of Masterton monthly average temperature as derived for NIWA's Seven-Station Series. Trendlines are represented by the faint dotted lines. Station moves and breakpoint lines are the vertical solid and dashed black lines respectively.

(https://www.ecmwf.int/en/forecasts/datasets/reanalysis-datasets/era5; accessed October 2020) for the nearest grid point (green lines Figure 10 and Figure 11) indicate nothing anomalous about this period. Further, an extended period of low flow in the Ruamahanga River (as measured at the Waihenga bridge) occurred in the summer of 1978 and

periods of high humidity would likely be associated with wet periods, thus we have lower confidence in the observed relative humidity record during this period at Masterton.

The ten most extreme maximum values of 9am dewpoint temperature and the dates on which these occurred are provided in Table 7 while the values of the extreme minimums and dates are provided in Table 8 The most extreme maximum T_d value appears to have been 23.7°C, on 23 January 1958. Extreme minimum events again occurred in winter, with the record minimum of -10.3°C of 3 August 1932. All the 10 bottom ranked events occurred prior to 1945.

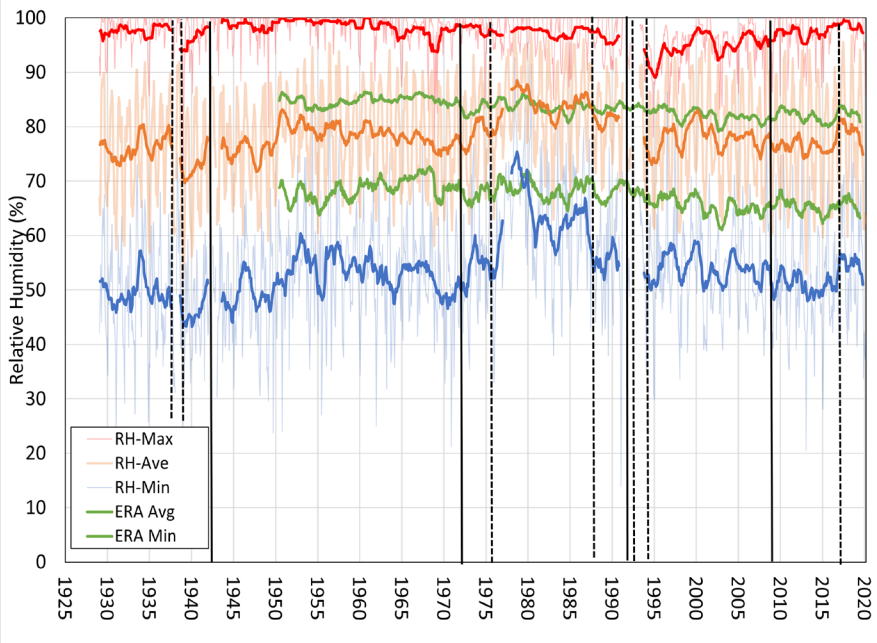

Figure 10: Monthly "9am" average (orange lines), minimum (blue lines), and maximum (red lines) time series (thin lines) of relative humidity (RH) for Masterton, Wairarapa for the period 1929 to 2019. The thick bold lines are running 12 month means of the average, minimum and maximum. Green lines are the ERA5 reanalysis for the nearest grid cell which has a higher mean orographic elevation so has a cold bias – hence the high humidity bias. Station moves and breakpoint lines are the vertical solid and dashed black lines respectively.

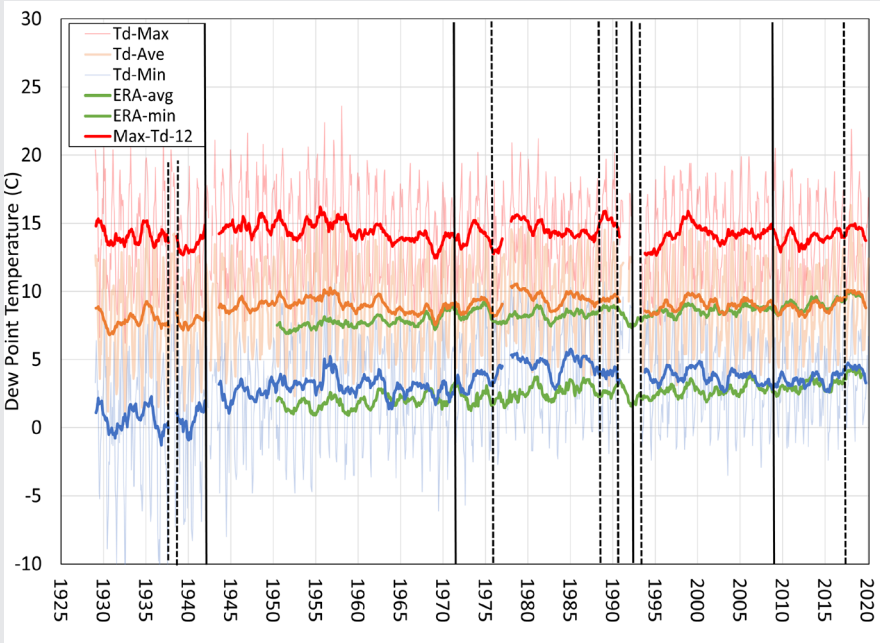

Figure 11: Monthly "9am" average (orange lines), minimum (blue lines), and maximum (red lines) time series (thin lines) of dewpoint temperature (T_d) for Masterton, Wairarapa for the period 1929 to 2019. The thick bold lines are running 12 month means of the average, minimum and maximum. Green lines are the ERA5 reanalysis for the nearest grid point

Date	Rank	T_a	T_w	RH	T_d	DPP
23/01/1958	1	24.4	23.9	95.4	23.7	0.7
27/01/1956	2	24.0	22.9	90.7	22.4	1.6
22/01/1937	3	22.7	22.2	96.1	22.0	0.7
12/02/2018	3	23.9	22.6	89.2	22.0	1.9
17/12/1946	5	23.3	22.2	90.6	21.7	1.6
14/02/1958	6	25.6	22.8	78.3	21.5	4.1
10/03/1981	7	26.0	22.8	75.4	21.3	4.7
7/02/1943	8	21.9	21.1	95.8	21.1	0.8
4/02/1957	8	21.1	21.1	100.0	21.1	0.0
30/01/1956	18	24.6	22.2	80.8	21.1	3.5

Table 7: Dates of extreme high values (top ten) of "9am" T_d (6th column) in the period 1928 to 2019 at Masterton. Also listed are the values T_a, T_w, RH and dewpoint depression (DPP = T_a-T_d) on these dates.

Date	Rank	T_a	T_w	RH	T_d	DPP
22/07/1932	1	4.2	0.0	33.8	-10.3	14.5
8/08/1936	2	5.2	0.5	30.2	-9.6	14.8
24/07/1937	3	5.3	0.7	30.7	-9.3	14.6
21/07/1931	4	2.8	-0.6	43.6	-8.4	11.2
6/06/1936	5	4.2	0.2	37.1	-8.2	12.4
10/07/1937	6	4.2	0.2	37.8	-8.0	12.2
8/06/1944	7	6.1	1.7	36.0	-8.0	14.1
27/06/1930	8	1.8	-1.0	50.4	-7.4	9.2
13/06/1936	9	3.3	0.1	46.7	-7.0	10.3
31/07/1937	10	5.3	1.2	37.7	-7.0	12.3

Table 8: Dates of extreme low (bottom ten) values of "9am" T_d (6th column) in the period 1928 to 2019 at Masterton. Also listed are the values T_a, T_w, RH and dewpoint depression (DPP = T_a-T_d) on these dates.

Finally, we present in Figure 12 the difference between the decades 2011-2020 and 1931-1940 in psychrometric chart for Masterton which shows a generally similar warming/moistening pattern as seen for Kelburn although it is somewhat "messier" than for Kelburn and reflective of the greater number of inhomogeneities at Masterton. This is displayed to demonstrate the kind of differences that could be seen in different decades.

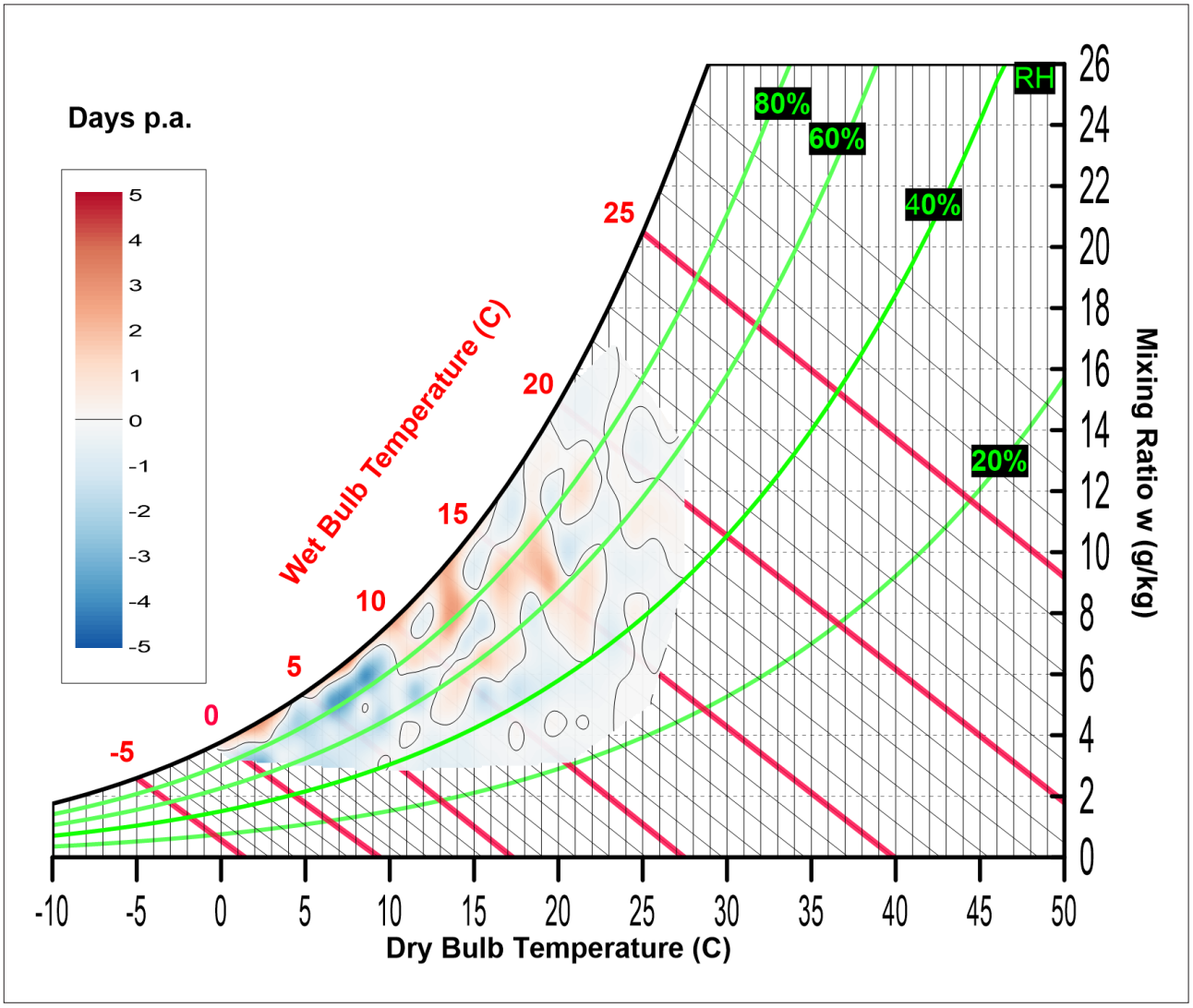

Figure 12: Colour-filled contour plot of difference (days per year)in distribution of 9 am dry bulb temperatures-mixing ratio combinations for 2011-2020 versus 1931-1940 for Masterton.

4. DISCUSSION

This article has presented the results of recent efforts to digitise daily wet- and dry-bulb temperature records for both Kelburn, Wellington and Masterton, Wairarapa sites back to 1929. The digitization of the Masterton and Kelburn records done here is to the author's knowledge the first to be done for New Zealand for dewpoint and wet-bulb temperatures, and RH. A number of breakpoints and station changes were noted for Masterton, while the Kelburn record had few. Only limited adjustments for time-of-observation changes were made and only one-period of station overlap was apparent. Unfortunately, due to the lack of other nearby digitized station records application of sophisticated homogenisation algorithms such as those of Rhodes and Salinger was not possible here. We recognise this as a gap in the work presented here. We recommend that this should be part of future work once other early station humidity records are digitized and become available.

Given the issues with homogenising the data; the trend analysis done here was kept simple and should not be over-interpreted and are presented as indicative. However, comparison with the NIWA Seven Station Series revealed broad consistency for running 12-month monthly average dry-bulb temperatures. Overall, both the Kelburn and Masterton series showed approximately a 0.7°C - 0.8°C increase in dewpoint temperature (T_d) averaged over all seasons with the strongest trend being an increase in winter, amounting to +1.7°C over 90 years at Kelburn, and +1.8°C at Masterton for the same period. Autumn also saw increasing trends at both locations whereas summer and spring saw smaller increases.

Other points of interest were that January 2018 had the highest average T_d values of any month in both the Kelburn and Wairarapa records while February 1998 was ranked third in the Kelburn record. Both 1998 and 2018 are tied for 3rd-warmest years on record for Aotearoa-New Zealand (dry bulb air temperature).

Despite the long-term upward trend, average T_d values for February 1938 and February 1935 were ranked second- and tenth-highest respectively in the Kelburn record. February 1935 is also ranked eighth-highest in the Wairarapa record.

Extreme high summer and autumn values of T_d occurred in the 1930s where there was considerable year to year variability.

Of the ten months with lowest average T_d values, seven occurred in the 1930s and 1940s for Wellington. At Masterton, six were in the 1930s and all ten had occurred by 1972.

Generally, there has been a trend to a warming and moistening for both stations examined and this is consistent with expectations, and other observed records and analyses of dry-bulb temperatures as with NIWA's Seven Station Series and with expectations around climate change such as an increased in days per year with higher temperatures and higher mixing ratios.

Finally, this effort was initially commissioned by the Greater Wellington Regional Council who were seeking to better understand climate trends in the Wellington and Wairarapa regions. It is recommended that the digitization efforts and long-term reconstruction analysis be extended to many more stations throughout Aotearoa New Zealand and include at a minimum all the stations that are part of NIWA's seven and/or eleven station long-term series and also those nearby stations used for the analysis of Mullan (2012) where the Rhoades and Salinger method was applied.

ACKNOWLEDGEMENTS

Trevor Carey-Smith (NIWA) is thanked for providing comment and feedback. Brett Mullan (RIP – NIWA) also provided very useful references and advice in the planning stages of the work. Neelesh Rampal (NIWA) provided the seven-station series mean temperatures. Tony Bromley provided old Metservice Hygrometric and psychrometric tables.

Support for the manuscript preparation was also provided by NIWA's Strategic Science Investment Fund for Climate and Hazards centre.

DATA AVAILABILITY STATEMENT

Climate Data is generally available from the NIWA's Climate Database (https://cliflo.niwa.co.nz). The digitized datasets (9am) can be made available upon request to the corresponding author. Finally, we thank the two anonymous reviewers who provided comprehensive and thoughtful reviews that have improved the original submission,

REFERENCES

Abbott, P.F., Tabony, R.C. 1985. The estimation of humidity parameters. Met. Mag., 114, 49-56. Bureau of Meteorology. 2003. *Equipment Specification A2669*. 215pp

Alduchov, O. A., Eskridge, R.E., 1996. Improved Magnus' form approximation of saturation vapor pressure. *J. Appl. Meteor.*, 35, 601–609.

August, E. F., 1828. Ueber die Berechnung der Expansivkraft des Wasserdunstes. *Ann. Phys. Chem.*, 13, 122–137.

Australian Bureau of Meteorology Official Website, 2020. http://www.bom.gov.au/climate/averages/climatology/relhum/calc-rh.pdf

Beresford, R., Turner, R., Tait, A., Paul, V., Macara, G., Yu, Z. Lima, L., Martin, R., 2018. Predicting the climatic risk of myrtle rust during its first year in New Zealand. *New Zealand Plant Protection* 71: 332-347 (2018). https://doi.org/10.30843/nzpp.2018.71.176

Brown, P. J., DeGaetano, A. T., 2009. A method to detect inhomogeneities in historical dewpoint temperature series. *J. Appl. Meteor. Climatol.*, 48, 2362-2376.

Fouhy, E., Coutts, L., McGann, R., Collen, B., Salinger, J,. 1992. South Pacific Historical Climate Network. Climate Station Histories. Part 2: New Zealand and Offshore Islands. 221 pp. ISBN 0-477-01583-2

Magnus, G., 1844. Versuche über die Spannkräfte des Wasserdampfs. *Ann. Phys. Chem.*, 61, 225–247.

McNoldy, B., 2019. Temperature Dewpoint, and Relative Humidity Calculator. https://bmcnoldy.rsmas.miami.edu/Humidity.html

Mullan, B. J., 2012. Applying the Rhoades and Salinger Method to New Zealand's "Seven-Station" Temperature Series. *Weather and Climate*, 32(1),24-38.

Omni, 2020. Wet Bulb Calculator, https://www.omnicalculator.com/physics/wet-bulb

Pearce, P., Fedaeff, N., Mullan, B., Rosier, S., Carey-Smith, T., Sood, A., 2019. Wellington Region climate change extremes and implications. NIWA client report 2019134AK prepared for Greater Wellington Regional Council. Available at: https://www.gw.govt.nz/assets/Climate-change/GWRC-NIWA-climate-extremes-FINAL3.pdf

Rhoades, D. A., Salinger, M.J., 1993. Adjustment of temperature and rainfall records fro site changes. *International Journal of Climatology*, 13, 899-913.

Salinger, M. J., Mullan, A. B., 1999. New Zealand climate: temperature and precipitation variations and their links with atmospheric circulation 1930–1994. *International Journal of Climatology*, 19, 1049-1071.

Salinger, M. J., Renwick, J. A., Mullan, A. B., 2001. Interdecadal Pacific oscillation and south Pacific climate. *International Journal of Climatology*, 21, 1705-1721.

Schindelholz, E.; Kelly, R. G., 2012. Wetting phenomena and time of wetness in atmospheric corrosion: a review. *Corros*. Rev. 30 (5-6), 135-207.

Smithsonian Institute, 1939. Smithsonian Meteorological Tables Fifth Revised Edition. Publication 3116 of the Smithsonian Institution, City of Washington, 282 pp.

Stull, R., 2011. Wet bulb temperature from relative humidity and air temperature. *J. Appl. Meteor. Climatol.*, 51, 2267-2269. https:/doi.org/10.1175/JAMC-D-11-0143.1

Turner, R., Pirooz, A. S., Flay, R. G. J., Moore, S., M. Revell, 2019. Use of High-Resolution Numerical Models and Statistical Approaches to Understand New Zealand Historical Wind Speed and Gust Climatologies. *J. Applied. Meteorology and Climatology*, 58, 1195-1218. https://doi.org/10.1175/JAMC-D-18-0347.1

Turner, R., Bromley, T., Tait, A., 2006, Potential aerial spread of Red Imported Fire Ant (RIFA) (Solenopsis Invicta) at Whirinaki Hawkes Bay. NIWA client report for MAF Biosecurity, WLG2006-68, 24 pp.

The New Zealand Reanalysis (NZRA): development and preliminary evaluation

Amir Pirooz[1], Stuart Moore[1], Trevor Carey-Smith[1], Richard Turner[1], Chun-Hsu Su[2]

[1] National Institute of Water and Atmospheric Research (NIWA), Wellington 6021, New Zealand
[2] Bureau of Meteorology, Docklands, Victoria 3008, Australia

ABSTRACT

The New Zealand Reanalysis (NZRA) is the first high-resolution convection-permitting atmospheric regional reanalysis model over Aotearoa New Zealand (NZ). NZRA has a spatial horizontal grid spacing of 1.5km and is forced using data from the Bureau of Meteorology Atmospheric high-resolution Regional Reanalysis for Australia (BARRA-R) with approximately 12km horizontal grid spacing. This paper outlines the development of NZRA, including the numerical weather forecast model and driving model. In addition, the performance of NZRA is compared against BARRA-R and global reanalysis products (ERA-Interim and ERA5) and validated against observational data collected during June-July 2014 as part of the Deep Propagating Gravity Wave Experiment (DEEPWAVE) field campaign. The results demonstrate that dynamically downscaling BARRA-R to NZRA considerably enhances the wind and temperature predictions, particularly capturing well the diurnal temperature cycle, wind speeds above 95th percentile, and gust wind speeds over the high elevation regions of NZ. In addition, NZRA provides better estimates of total precipitation over the North Island, Canterbury region, West Coast and the southern part of the South Island compared to the Virtual Climate Station Network (VCSN) gridded observation-based product, other reanalyses and NIWA's operational convective-scale forecast model, NZCSM, as was run in 2014.

1. INTRODUCTION

Atmospheric reanalyses provide physically coherent and long-term spatially complete records of various climate variables (Su et al., 2019; Minola et al., 2020) and are today among the most used datasets in climatological and geophysical research, due to the fact that they are able to generate consistent series of various climate variables (Dee et al., 2011). The key benefit is from being able to re-forecast historical periods using modern forecast models and data assimilation techniques, such as four-dimensional variational data assimilation (4D-Var) (Bannister, 2017), that make better use of observation data from various sources.

Although global-scale reanalyses have advanced significantly in quality and provide physically coherent and long-term spatially complete information for the whole globe, their spatial and temporal resolutions are still relatively coarse and it has been demonstrated that, with spatial resolutions typically greater than 30-50km, they may not be able to capture small-scale meteorological process and other sub-grid phenomena, particularly over complex terrain (Mesinger et al., 2006; Yoshimura and Kanamitsu, 2008; Su et al., 2019). The coarse resolution of global reanalyses has also implications on quality and impactfulness of subsequent studies, such as the hydrological response to climate change scenarios (Miller et al., 2003), wind speed over complex terrain (Minola et al., 2020), the impact of climate change on agriculture (Fuhrer et al., 2006), energy (Zhang et al., 2018; Frank et al., 2020), extreme winds (Steinheuer and Friederichs, 2020; Taszarek et al., 2020), and rainfall (Gleixner et al., 2020; Hu and Franzke, 2020).

Tetzner et al. (2019) conducted a regional evaluation of meteorological parameters in the southern Antarctic Peninsula and Ellsworth Land using two global reanalyses, namely ERA5 (Hersbach et al., 2020) and its predecessor ERA-Interim (Dee et al., 2011), from the European

Centre for Medium-Range Weather Forecasts (ECMWF). Although the higher resolution ERA5 outperformed ERA-Interim by reducing the cold coastal biases and had a better representation of near-surface air temperature and wind speed, both the reanalyses underestimated wind speed, which could be attributed to the effects of topographic features. Validating ERA5 and ERA-Interim against observations across Norway and Sweden, Minola et al. (2020) also showed that both reanalyses underestimate high wind speeds.

Dynamically downscaling global reanalyses to higher-resolution regional reanalyses could address the shortcomings of the global reanalysis datasets (Komurcu et al., 2018; Steinke, 2019; Su et al., 2019; Lu et al., 2021). Regional reanalyses can potentially provide more detailed meteorological information than global models, by leveraging recent advances in higher resolution regional numerical weather prediction (NWP) models and data assimilation systems (Frank et al., 2020; Lu et al., 2021). This is achieved by nesting a high-resolution NWP model within a global reanalysis (e.g., ERA5). Due to their higher spatial and temporal resolutions, these regional models can resolve small-scale forcing events, such as convection (Frank et al., 2020; Su et al., 2021), and represent extremes of variables more accurately (Komurcu et al., 2018; Steinheuer and Friederichs, 2020).

Comparison between 2 and 6km regional reanalyses against the ~80km resolution ERA-Interim, Steinke (2019) demonstrated that instantaneous, daily and monthly integrated water vapour are significantly better represented in the regional reanalyses. Due to their higher spatial and temporal resolutions, regional reanalyses can more accurately capture the timing, intensity, and spatial extent of climate and environmental variables (Leeper et al., 2017; Lu et al., 2019). For example, better representation of wind gust speeds in higher resolution regional reanalyses enabled Steinheuer and Friederichs (2020) to estimate the wind gust speeds at different vertical heights using 10-m gust wind outputs and other climate variables. The Indian Monsoon Data Assimilation and Analysis (IMDAA) dataset, a high-resolution reanalysis with 12km horizontal resolution, has been shown to outperform ERA-Interim over India (Ashrit et al., 2020). Acharya et al (2019) evaluated the performance of the Bureau of Meteorology Atmospheric high-resolution Regional Reanalysis for Australia (BARRA-R) (Su et al., 2019) in predicting spatio-temporal characteristics of precipitation fields across Australia. It was demonstrated that BARRA-R outperforms its driving model, ERA-Interim, and better represents the distribution of wet days and transition probabilities.

Frank et al. (2020) demonstrated that the recently developed convective-scale regional reanalysis system for Central Europe (COSMO-REA2) with a spatial horizontal resolution of 2km provides considerable improvement in predictions of wind field and precipitation on different time scales compared with coarser gridded global reanalyses. Having compared the performances of four global and three regional reanalyses in representing near-surface temperature and precipitation, Keller and Wahl (2021) showed that although regional reanalyses add value over global reanalyses, particularly for precipitation, the performance of reanalysis models varies considerably not only between the models, but also between variables and locations. Thus, the use of reanalyses strongly depends on the specific application and region. Safaei Pirooz et al. (2022) compared the performance of three global reanalyses and BARRA-R over New Zealand and concluded that BARRA-R generally outperforms the other reanalyses.

It is evident that high-resolution regional reanalyses significantly enhance the prediction of climate variables and their spatio-temporal variability. Gaining a better understanding of the past climate and the mechanisms leading to extremes and general climatology is essential for many environmental, engineering, and meteorological studies as well as for improving climate projection model estimates. Currently, the highest resolution regional reanalysis available for New Zealand is the BARRA-R model (Su et al., 2019), which utilises the UK Met Office Unified Model (UM) with a horizontal resolution of 12km and uses ERA-Interim as the driving model. Su et al. (2021) downscaled BARRA-R reanalysis to 1.5km horizontal resolution, called BARRA-C, over four major Australian cities. It was demonstrated that BARRA-C provides additional skill over BARRA-R, with wind and temperature performance, particularly over complex and coastal regions, enhanced compared with the 12km BARRA-R model. Improvements were also observed in BARRA-C predictions of the timing and intensity of precipitation during convective events as well as in the spatial distribution of sub-daily rainfall totals.

In this study, we describe the development of the New Zealand Reanalysis (NZRA) whereby BARRA-R is dynamically downscaled to a 1.5km horizontal grid spacing over New Zealand. NZRA uses the UM and after completion will cover the 1990-2018 period. The aim of our research is to demonstrate the added value of the NZRA over its

driving model (BARRA-R) and global reanalyses (ERA5 and ERA-Interim). The paper is structured as follows. In Section 2, we outline the NZRA setup and configuration as well as the other datasets used in the paper. The evaluation of NZRA over a trial period of June-July 2014 against point-based observations and an observation-based interpolated gridded dataset is presented in Section 3, focusing on precipitation, air temperature, mean and gust wind speeds. Lastly, Section 4 summarises our findings and discusses the added skills of NZRA over other reanalyses.

2. METHODOLOGY AND DATA

2.1 NZRA

The first high-resolution convection-permitting regional reanalysis model for New Zealand, the New Zealand Reanalysis (NZRA), has been developed at the National Institute for Water and Atmospheric Research (NIWA) and is based on the UK Met Office Unified Model (UM) (Davies et al., 2005). The UM is a non-hydrostatic, fully compressible, deep-atmosphere model whose dynamical core, ENDGame (Even Newer Dynamics for General atmospheric modelling of the environment), solves the equations of motion using mass-conservation, semi-implicit, semi-Lagrangian, time-integration methods (Wood et al., 2014). A comprehensive description of parameterisations and physics schemes included in UM can be found in Bush et al (2020).

The NZRA domain (Figure 1a) is the same as NIWA's operational convective-scale forecast model. The NZRA model has a horizontal grid spacing of 0.0135° × 0.0135° (approximately 1.5km) on a rotated pole coordinate system, comprising 1350 × 1200 grid points in the north-south (meridional) and west-east (zonal) directions respectively. The NZRA domain has 70 vertical levels extending from near the surface to 40km above sea level. Near the surface, vertical levels follow the modelled orography and then relax to a uniform radial height above about 18km (62 model levels). The model is run with an integration timestep of 60s. Figure 1b depicts the NZRA's model orography as well as the location of the point observations used in this study at Hokitika.

The development of NZRA is similar to NIWA's operational New Zealand Convective-Scale Model (NZCSM) but features some differences in the science configuration, driving model and forecast length. NZRA uses the same ancillary input data as NZCSM, including orography, land-sea mask, canopy heights and other land cover data. The model uses an underlying orography created at the model resolution of 1.5km from the 1 km horizontal resolution Global Land One-km Base Elevation (GLOBE) dataset (GLOBE Task Team, 1999). Land cover data are based on the Climate Change Initiative (CCI) (Hartley et al., 2017).

NZRA is a downscale-only system that takes its initial and lateral boundary conditions from BARRA-R (Su et al.,

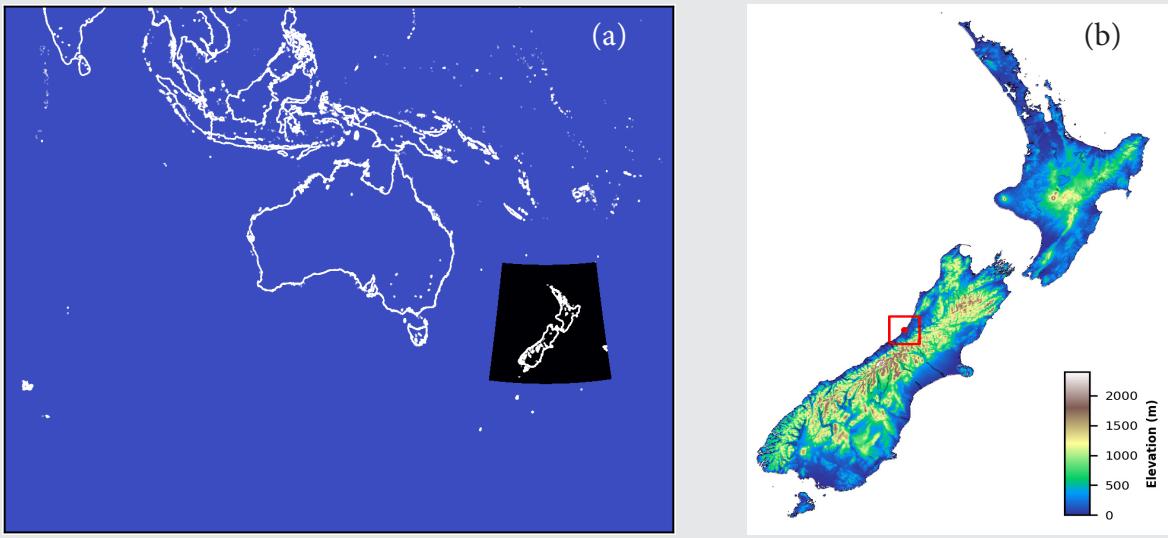

Figure 1: (a) BARRA-R 12km reanalysis (blue) and NZRA/NZCSM (black) domains. (b) NZRA model orography and the location of point observations used in this paper.

	Name	Reference	Spatial Resolution	Temporal Resolution	Model Cycle
Global	ERA-Interim	Dee et al. (2011)	80km	3-hourly	Cy31r2 (2006)
	ERA5	Hersbach et al. (2020)	31km	Hourly	Cy41r2 (2016)
Regional	BARRA-R	Su et al. (2019)	12km	Hourly	UM 10.2
	NZCSM (as run in 2014)	Carey-Smith and Andrews (2016) Turner and Moore (2017)	1.5km	30 mins	UM 8.4
	NZRA	Current paper	1.5km	30 mins	UM 11.4

Table 1: Global- and regional-scale reanalysis datasets used in this study.

2019). The NZRA model is re-initialised every six hours on the synoptic hours, 00:00, 06:00, 12:00 and 18:00 UTC. Lateral boundary conditions have a 30-minute temporal resolution. This setup allows for the development of larger-scale features within NZRA. Similar to BARRA-C (Su et al., 2021), each hindcast in NZRA is a nine-hour simulation, however, the first three hours are discarded due to model spin-up and only the last six hours saved. During the spin-up period the interior of the higher resolution model domain is establishing the finer atmospheric motions that may only partially be present in the coarser resolution initial conditions and we choose to ignore this period to ensure the continuous NZRA dataset is minimally impacted by this adjustment process.

The science configuration used in NZRA is the midlatitude version of the second Regional Atmosphere and Land configuration (RAL2–M) (Bush et al., 2020). Unlike its driving model BARRA-R, NZRA does not use a convection parametrisation scheme. Therefore, NZRA relies on the model dynamics to represent convective motion. As outlined in Su et al (2021), although at 1.5km resolution convection and other small-scale processes are not fully resolved, it is known that removal of the cumulus parametrisation provides more realistic behaviour (Clark et al., 2016) and an overrepresentation of low rainfall rates can be improved via the introduction of the Leonard term into the UM's sub-grid mixing scheme as described in Hanley et al (2019) and implemented in the RAL2-M science configuration used by NZRA.

2.2. Other Reanalysis and Point-Observation Data

For point-based assessment, observation data collected at Hokitika, New Zealand, during June-July 2014 as part of the Deep Propagating Gravity Wave Experiment (DEEPWAVE)[1] campaign over New Zealand (Fritts et al., 2016) were used. Considering that data from most meteorological stations across New Zealand have been incorporated into the BARRA-R's data assimilation system, the DEEPWAVE data provides a set of independent observations that can be used for this preliminary assessment of the NZRA.

DEEPWAVE studied the dynamics of gravity waves (GWs) from the surface of the Earth to the mesosphere and lower thermosphere. The project examined how tropospheric winds and storms modulate the generation of GWs. The project also examined how GWs propagate across the tropopause into the stratosphere including the polar night jet and tidal winds that influence GW propagation and breakdown in the middle atmosphere. The data collected during this period have been used for various scientific objectives, including investigation of orographically induced GW (Witschas et al., 2017), GW propagation (Ehard et al., 2016; Fritts et al., 2016), and moist biases in various configuration of the UM (Yang et al., 2017).

Here, high-temporal resolution (30-sec) point-based observation data of rain rate, surface temperature and wind speed are used to evaluate the NZRA performance for this trial period. The observed temporal resolution was down-sampled to match the reanalysis outputs, e.g., 30-min instantaneous winds and temperature and 30-min accumulated rainfall.

In addition to these observation data, two global reanalyses, ERA-Interim and ERA5, one regional reanalysis, BARRA-R, and one operational forecast model, NZCSM, were also compared against NZRA. Table 1 summarises the

[1] https://www.eol.ucar.edu/field_projects/deepwave

main specifications of the NWP models used in this study. It should be noted that for the verification period used in this study (June-July 2014), an older version of UM employing the New Dynamics dynamical core, was in use by the NZCSM. The ENDGame dynamical core used in current versions of the UM was introduced in the NZCSM in 2017. Therefore, the results of NZCSM in this study should not be interpreted as the current performance of NZCSM.

To spatially compare precipitation, a gridded precipitation dataset based on interpolated observation data, called the Augmented Virtual Climate Station Network (VCSN), is used. The Augmented VCSN, which contains daily precipitation data at 5km grid resolution, incorporates considerably more rain observations (around 1200) compared to the original version of the VCSN (Tait and Turner, 2005; Tait et al., 2006; Tait et al., 2012).

3. RESULTS AND DISCUSSION

3.1 Point-Based Observation at Hokitika

3.1.1 Wind speed

Figure 2 shows percentile (or Q-Q) plots comparing the reanalyses and observation 10m wind speed deviations from mean values. The percentile plots provide an indication of how the reanalysis resolves the extremes. In addition, differences between observed and reanalysed wind speed at several percentiles are tabulated in Table 2. As illustrated in Figure 2 and Table 2, NZRA more closely matches the observed wind speed even at higher percentile thresholds in comparison to other reanalysis products. In particular, the NZRA wind speed is closer to that of the observations above the 90th percentile and up to the 99.5th percentile, while the other reanalyses, particularly ERA-Interim and

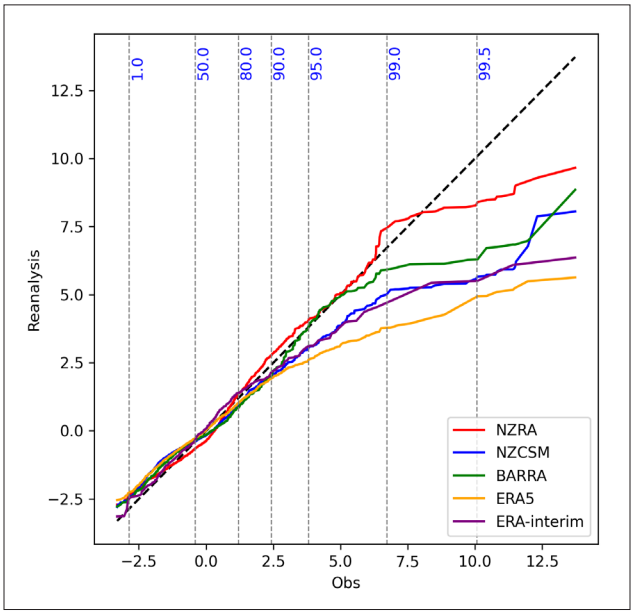

Figure 2: Comparisons of percentile values between observations at Hokitika and reanalyses for 10m wind speed. The vertical dash lines indicate the corresponding percentiles of the observations.

ERA5, strongly underestimate the wind speed. In addition, NZRA outperforms and adds significant value over its driving model, BARRA-R, in estimating strong winds. The underestimation of strong winds in reanalyses could be attributed to many potential reasons, such as the model's representation of orography, land cover data including vegetation types and roughness, poor modelling of wind speeds in unstable conditions, and gust parameterisation as elaborated on in (Rose and Apt, 2016; Su et al., 2019; Minola et al., 2020).

Correlation (R^2) values and slope (S) of the best fit line between reanalyses and observations for 10m wind speed are illustrated in Figure 3. Overall, NZRA has higher R^2 and S values against observations than the other datasets. Figure 4 compares the timeseries of wind speed from the

	10m wind speed (ms^{-1})				
Percentiles >	**1**	**90**	**95**	**99**	**99.5**
NZRA	0.458	0.348	0.240	0.732	–1.694
NZCSM	0.423	–0.423	–0.784	–1.707	–4.432
BARRA-R	0.362	–0.388	–0.004	–0.772	–3.798
ERA5	0.597	–0.518	–1.193	–2.922	–5.152
ERA-int	0.337	–0.297	–0.694	–1.944	–4.588

Table 2: Difference ($m\ s^{-1}$) between observed and reanalyses wind speeds at various percentiles.

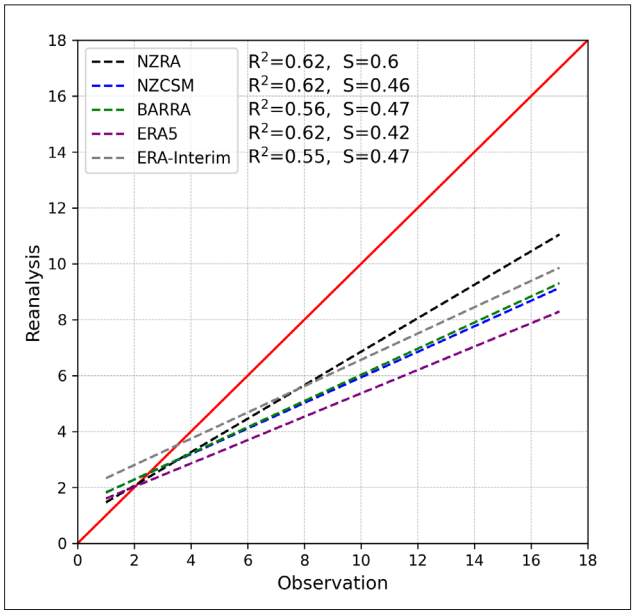

Figure 3 (above): Linear relationship between reanalysis and observed 10m wind speed. "S" and "R^2" are the slope and correlation of the best fit line, respectively.

reanalyses and point observation at the Hokitika location. NZRA predicts peak wind speeds and sudden increases/decreases in wind speed magnitudes more accurately compared to the other products.

3.1.2. Surface temperature

Similar to Figure 2, Figure 5 depicts percentile (or Q-Q) plots of 2m surface temperature from the reanalyses and observations and Table 3 shows the differences between these values at various percentiles. The NZCSM (as was run in 2014) and ERA5 overestimate and underestimate surface temperature in regimes below the 25th percentile and above the 50th percentile respectively. Although ERA-Interim also overestimates the low percentile temperatures, it provides better estimates of high percentile temperatures

Figure 4 (below): Comparison of 10m wind speed timeseries between each reanalysis dataset and observations at Hokitika. Time is in UTC.

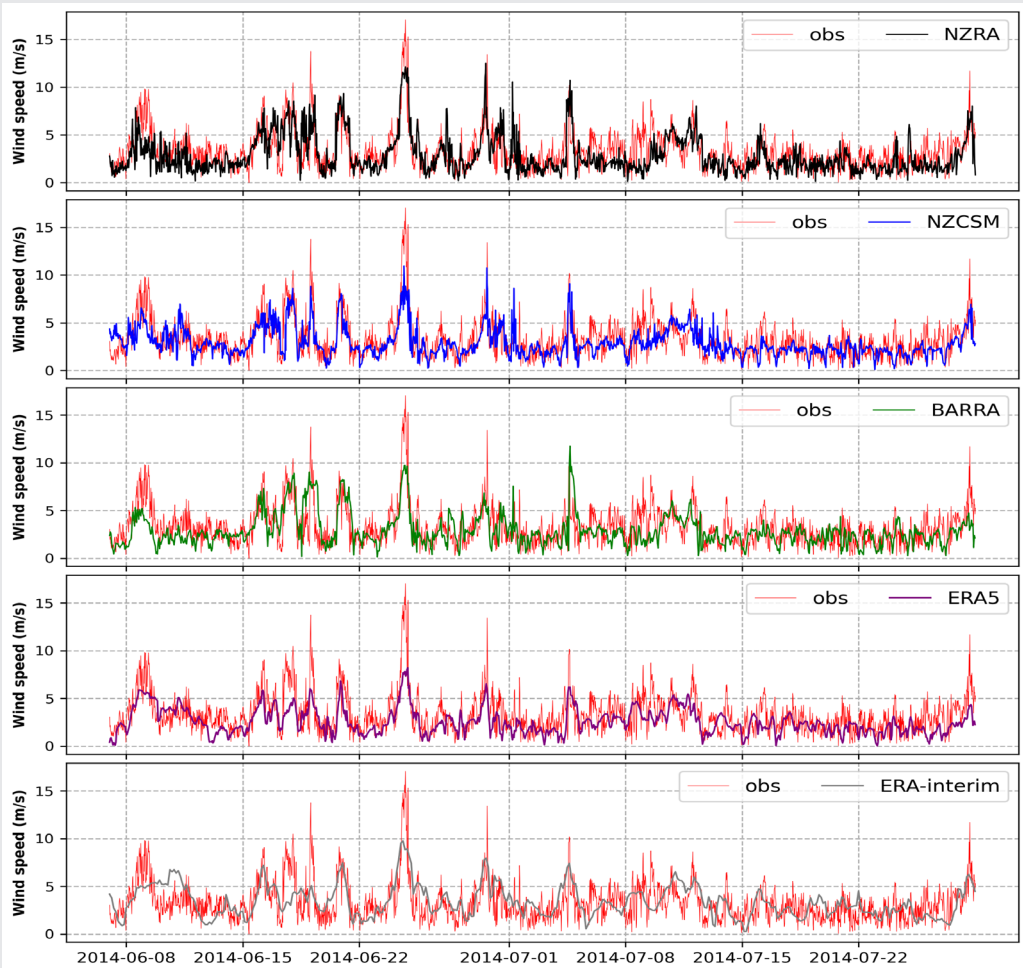

than that of ERA5 and NZCSM. NZRA and BARRA-R temperature show the best agreement with the observations for all percentiles, with NZRA marginally outperforming BARRA-R when compared across all percentiles. NZRA does tend to overestimate surface temperatures at the higher percentile range, while other datasets underestimate.

The average differences between the reanalysis datasets and the observed surface temperature, presented as a diurnal cycle during June-July 2014 are shown in Figure 6. ERA-Interim demonstrates a significant cold bias, considerably underestimating the temperature at all hours. Unlike other products, NZCSM shows a warm bias of about +1°C between 06:00 to 21:00 UTC. NZRA, BARRA-R and ERA5 have a similar bias and all depict a cold bias at all hours. NZRA does however have a smaller bias from 06:00 to 14:00 UTC compared to BARRA-R.

Figure 7 compares the timeseries of surface temperature from the reanalyses and point observations at the Hokitika location. NZRA performs considerably better than the ERA datasets and NZCSM, and marginally better than

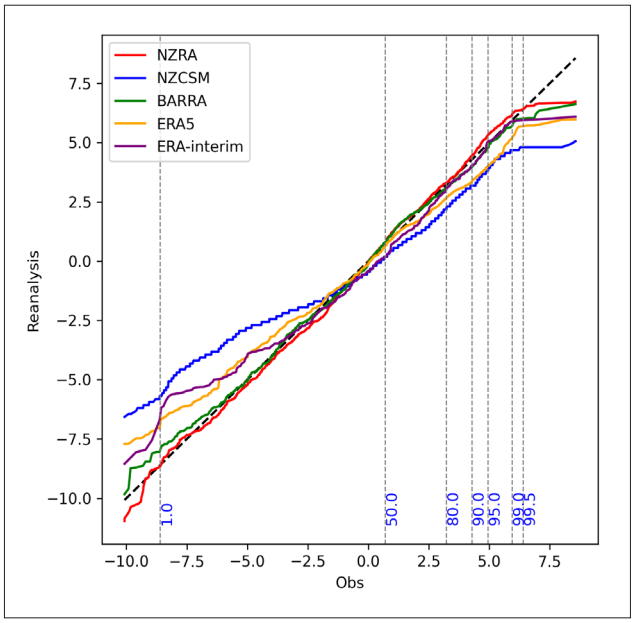

Figure 5: Comparisons of percentile values between observations at Hokitika and the reanalyses for 2m surface temperature. The vertical dash lines indicate the corresponding percentiles of the observations.

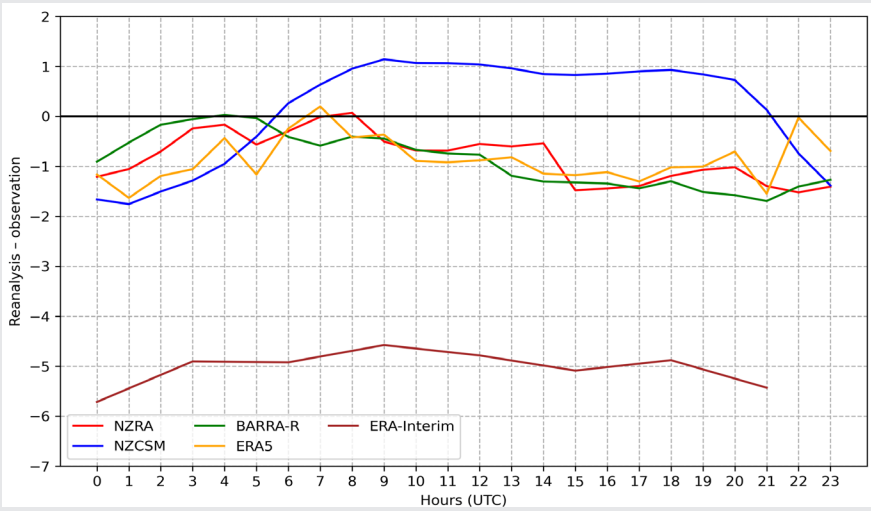

Figure 6: Hokitika diurnal surface temperature average difference between the reanalyses and observations.

	2m surface temperature				
Percentiles >	**1**	**90**	**95**	**99**	**99.5**
NZRA	–0.037	0.160	0.356	0.236	0.005
NZCSM	2.931	–1.106	–1.129	–1.264	–1.620
BARRA-R	0.577	–0.320	–0.154	–0.212	–0.411
ERA5	1.574	–0.929	–0.925	–0.727	–0.734
ERA-int	1.929	–0.247	0.086	–0.063	–0.481

Table 3: Difference between observed and reanalysed surface temperature at various percentiles.

BARRA-R in capturing high and low temperatures as well as daily cycles (see 2014-07-15 to 2014-07-31 UTC). Linear relationships along with correlation values (R^2) and slopes (S) of the best fit line between reanalyses and observations are illustrated in Figure 8. Overall, NZRA has higher R^2 and S values against observations than the other datasets.

To further investigate the performance of the reanalyses' predictions of extreme temperatures, Table 4 summarises the statistical scores, including Pearson's correlation, root-mean squared error (RMSE), bias and mean absolute error (MAE), for daily minimum and maximum surface temperature against the point observations.

Table 4 indicates that for daily maximum surface temperature, NZRA has the best scores among all the considered reanalyses, except for the correlation value where NZCSM and ERA5 have slightly higher values than NZRA. NZRA has the smallest MAE in daily minimum temperature. However, ERA5 shows smaller bias and

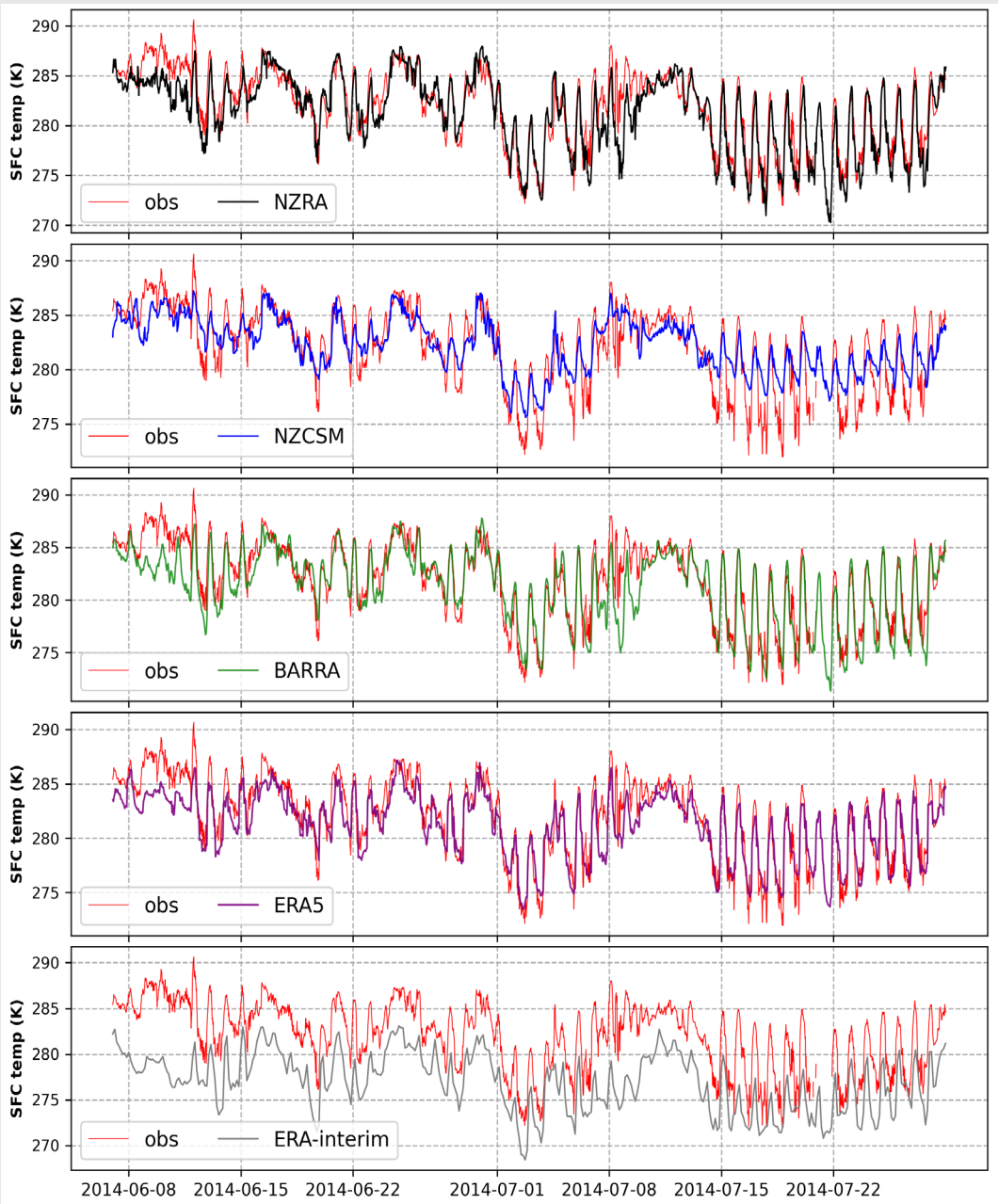

Figure 7: Comparisons of surface temperature timeseries between reanalyses and observation. Time is in UTC.

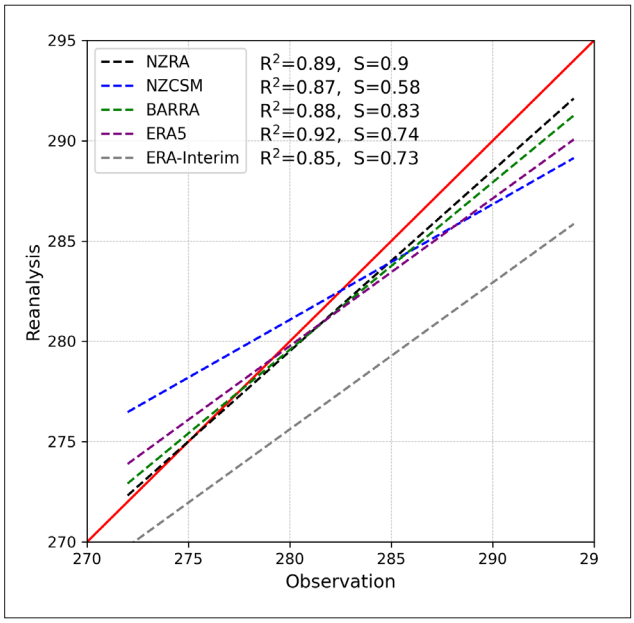

Figure 8: Linear relationship between reanalysis and observed 2m surface temperature. "S" and "R²" are the slope and correlation of the best fit line, respectively.

simulated by NZRA and NZCSM and measured at Hokitika during June-July 2014 are compared in Figure 9a. NZRA appears to capture a larger proportion of the higher rainfall rates more accurately than NZCSM does, although errors in timing and intensity do remain. For closer inspection, the daily accumulated rainfall amounts from NZRA, NZCSM and also BARRA-R are shown in Figure 9b and compared with observed values. It appears that all three products provide reasonably accurate estimates of daily precipitation amount on the daily timescale, though all datasets both under- and over-predict the daily amounts, sometimes considerably so, over the course of the DEEPWAVE campaign period. The statistical scores comparing observations with the NZRA, NZCSM and BARRA-R datasets for daily precipitation are shown in Table 5. The scores from all the considered models are relatively similar, however NZRA whilst having the lowest MAE (good) does exhibit the worst correlation, RMSE and bias values.

Figure 10 depicts the percentile comparison plot of

	Daily minimum temperature				Daily maximum temperature			
	Corr.	RMSE	Bias	MAE	Corr.	RMSE	Bias	MAE
NZRA	0.926	1.718	–0.702	1.213	0.816	1.247	–0.425	0.883
NZCSM	0.863	2.909	1.684	2.318	0.912	1.488	–1.228	1.296
BARRA-R	0.904	1.763	–0.375	1.317	0.796	1.326	–0.488	0.913
ERA5	0.946	1.534	0.163	1.230	0.868	1.578	–1.201	1.275
ERA-Int	0.898	4.124	–3.691	3.719	0.601	5.890	–5.606	5.606

Table 4: Statistical scores for daily minimum and maximum surface temperature between observations and reanalyses.

RMSE and higher correlation values. BARRA-R, although performing worse than NZRA generally, has slightly smaller bias value compared with NZRA for daily minimum temperature.

3.1.3. Precipitation

Safaei Pirooz et al. (2022) demonstrated that ERA5 and ERA-Interim perform poorly in their predictions of precipitation compared with higher resolution products such as BARRA-R, particularly over the mountainous regions and west coast of the South Island. Therefore, in this section, only the precipitation estimates of NZCSM, NZRA and BARRA-R are compared against observations. Instantaneous rainfall rates at 30 minute intervals as NZRA, NZCSM and BARRA-R hourly precipitation amounts greater than 1mm. Similar performance is found across all the datasets at the lowest percentiles ranges (up to 50th percentile) after which all begin to noticeably underpredict precipitations compared to the observations. NZCSM performs better than NZRA and BARRA-R at the more extreme percentile range, explaining the results in Table 5. Considering the short timeseries used in this verification and that this is just one location, not representative of all of NZ, in future, a more comprehensive assessment of NZRA rainfall will be conducted.

3.2. Spatial comparison

This section presents an evaluation of spatial variability

	Corr.	RMSE	Bias	MAE
NZRA	0.849	9.012	-2.584	3.910
NZCSM	0.850	7.753	-0.190	4.348
BARRA-R	0.862	7.787	-1.892	4.078

Table 5: Statistical scores for daily accumulated precipitation between observation and reanalyses.

$$\%bias = 100 \times \frac{mean(d_m) - mean(d_0)}{mean(d_0)}$$

Equation 1: Where d_m and d_0 are the daily accumulated precipitations from the reanalyses and VCSN, respectively.

In addition, MAE values of total precipitation during 30/05/2014 – 01/08/2014 averaged over the North and South Islands are summarised in Table 6. It is evident that NZRA shows smaller MAE over both islands compared with NZCSM and its driving model BARRA-R.

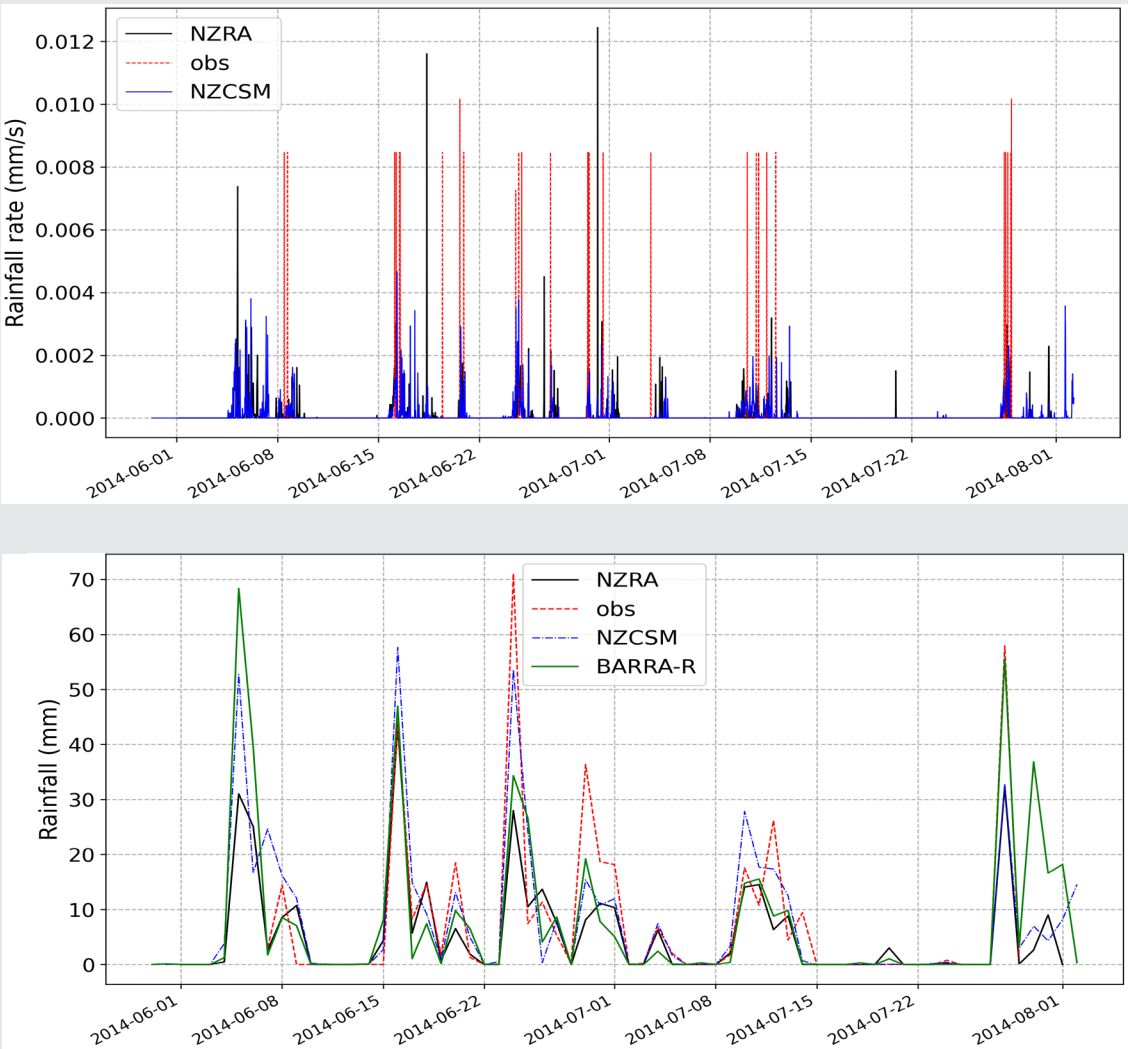

Figure 9: Comparison at Hokitika, New Zealand, during June-July 2014 of **(a)** Instantaneous rainfall rate timeseries at 30 minute intervals from point observations and closest NZRA and NZCSM grid points, and **(b)** daily accumulated precipitation, from point observations and closest NZRA, NZCSM and BARRA-R grid points.

in precipitation and frequency of high gust and mean wind speeds in the NZRA, NZCSM, BARRA-R and ERA datasets. Concentrating only on the non-ERA datasets first, the biases in the accumulated daily precipitation of the regional reanalyses are calculated using Eq. 1 with respect to the Augmented VCSN values for June-July 2014.

Due to the orographic induced rainfall over the Southern Alps, there is generally much more rainfall over the western side of the South Island than over other areas

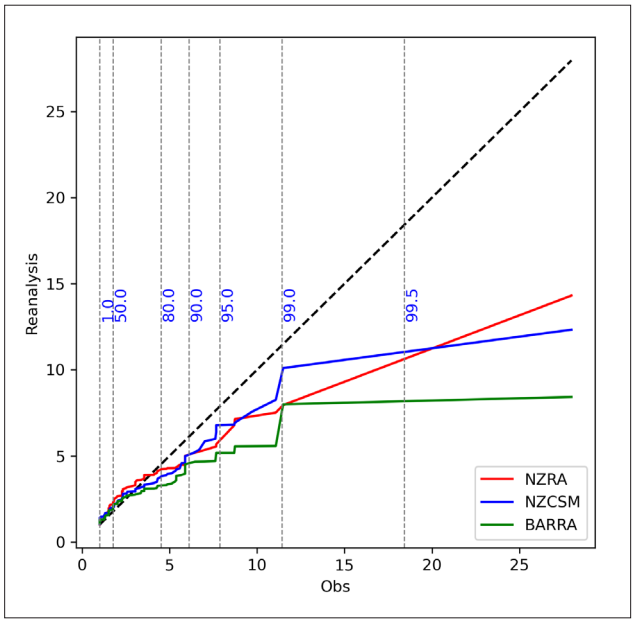

Figure 10: Comparisons of percentile values between observations at Hokitika and reanalyses for hourly accumulated precipitation greater than 1mm. The vertical dash lines indicate the corresponding percentiles of the observations.

al., 2019) and other reanalyses (Minola et al., 2020). Safaei Pirooz et al (2022) also showed that BARRA-R, unlike ERA5, does not capture the high gust wind speeds over the more southern mountains of the South Island. Figure 12 compares the frequency of gust wind speeds exceeding 25ms^{-1} in all the datasets considered in this study.

Similar to the analysis in Safaei Pirooz et al (2022), Figure 12 depicts that BARRA-R is unable to simulate strong wind speeds over the Southern Alps and other high peaks such as Mount Taranaki, and consequently shows lower occurrence of these events. All of the datasets show signs of similar high gust wind speed regions offshore, but NZRA and NZCSM deviate significantly over land from BARRA-R, ERA5 and ERA-Interim, particularly over high elevation regions, due to their higher spatial resolution being better able to resolve NZ's mountainous terrain. NZRA exhibits a higher frequency of strong winds compared to NZCSM over a larger area of mountainous terrain, particularly the central and southern most peaks of the South Island and Tararua, Ruahine and Central Plateau regions of the North Island. The other reanalyses, BARRA-R, ERA5 and ERA-Interim, significantly underestimate strong winds and their frequency over land.

	North Island MAE (mm)	South Island MAE (mm)
NZRA	64.241	102.380
NZCSM	73.451	119.318
BARRA-R	78.269	116.785

Table 6: Mean absolute errors of total accumulated precipitation (during 30/05/2014 – 01/08/2014) between VCSN and NWP models.

of the country. One of the known issues of BARRA-R is that it overestimates precipitation over regions with high elevations (Su et al., 2019), as can also be seen along the west coast of the South Island in Figure 11b. In comparison, the NZRA shows smaller wet bias in precipitation in high-elevation regions compared with BARRA-R and NZCSM. Additionally, across the North Island (Figure 11a), NZRA also exhibits smaller biases, particularly over the west coast and southeast part of the North Island. NZCSM has a predominately wet bias over much of the North Island, with NZRA following BARRA-R in terms of spatial distribution of wet and dry biases over the North Island, but the magnitude of the bias is often smaller (Figure 11a). and BARRA-R have wet and dry biases over the most part of the island. A notable exception being over the Auckland region.

Positive and negative biases during light and strong wind events are another identified issue in BARRA-R (Su et

Similar performances can be seen in the frequency of relatively strong surface mean wind speeds in Figure 13. Here, frequency of surface mean wind speeds greater than 5ms^{-1} over New Zealand are plotted. More so than in Figure 12, a stark north-south split is exhibited in the BARRA-R, ERA5 and ERA-Interim datasets, all three indicating very little occurrence of >5ms^{-1} mean wind speeds over the South Island compared to NZRA and NZCSM. Comparing against VCSN data, Safaei Pirooz et al. (2022) showed previously that BARRA-R, ERA5 and ERA-Interim have large negative biases in mean surface wind speed over the South Island generally, so the higher frequency of >5ms^{-1} mean wind speeds over the South Island in NZRA represents a clear improvement over the other reanalysis datasets.

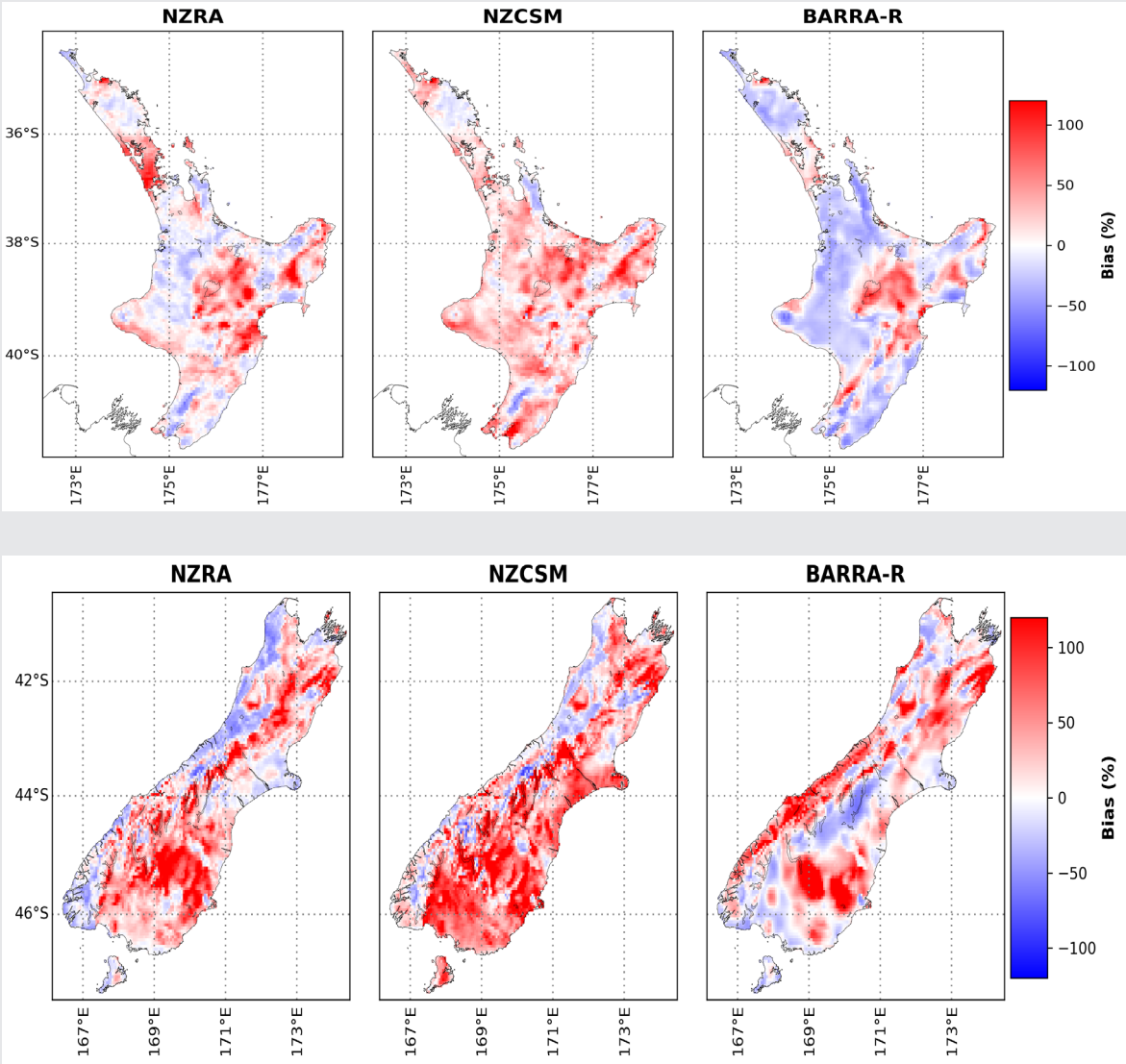

Figure 11: Mean bias percentages in daily accumulated precipitation during June-July 2014 from NZRA (left), NZCSM (middle) and BARRA-R (right) against the augmented VCSN across: (a) North Island, and (b) South Island.

4. CONCLUSION

This paper describes the development of the first high-resolution convective-permitting regional reanalysis model for New Zealand, called New Zealand Reanalysis (NZRA). NZRA, with a spatial horizontal grid spacing of 1.5km and 30 minute temporal resolution, is based on the UK Met Office Unified Model and is dynamically downscaled from the recently developed Bureau of Meteorology Atmospheric high-resolution Regional Reanalysis for Australia (BARRA-R) with approximately 12km horizontal resolution. BARRA-R provides both the initial and lateral boundary conditions to NZRA.

NZRA performance against independent observation data collected for the DEEPWAVE period (June – July 2014), has been evaluated to demonstrate its skill compared to existing global and regional reanalyses that cover New Zealand. It is shown that NZRA provides significantly better estimates of surface temperature for all percentiles and temperature ranges. In addition, NZRA surface wind speeds are closer to observations, particularly above the 90th percentile, compared with the other datasets. The biases in NZRA accumulated daily precipitation are generally smaller than NZCSM and BARRA-R over most of the North Island, and across the Canterbury region, West Coast and southern parts of the South Island. Standout areas where

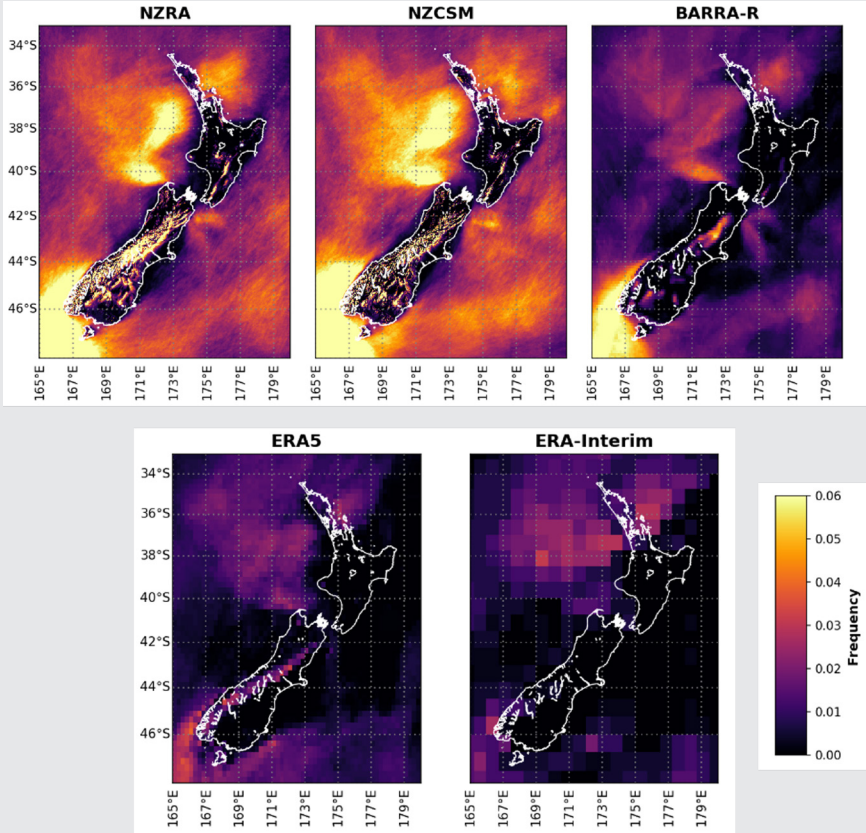

Figure 12: Frequency (ranging 0 to 1) of gust wind speeds greater than 25ms^{-1} over New Zealand for the period June – July 2014 from the different reanalyses and NZCSM. The native temporal resolution of each product (see Table 1) has been used in the calculation of frequencies.

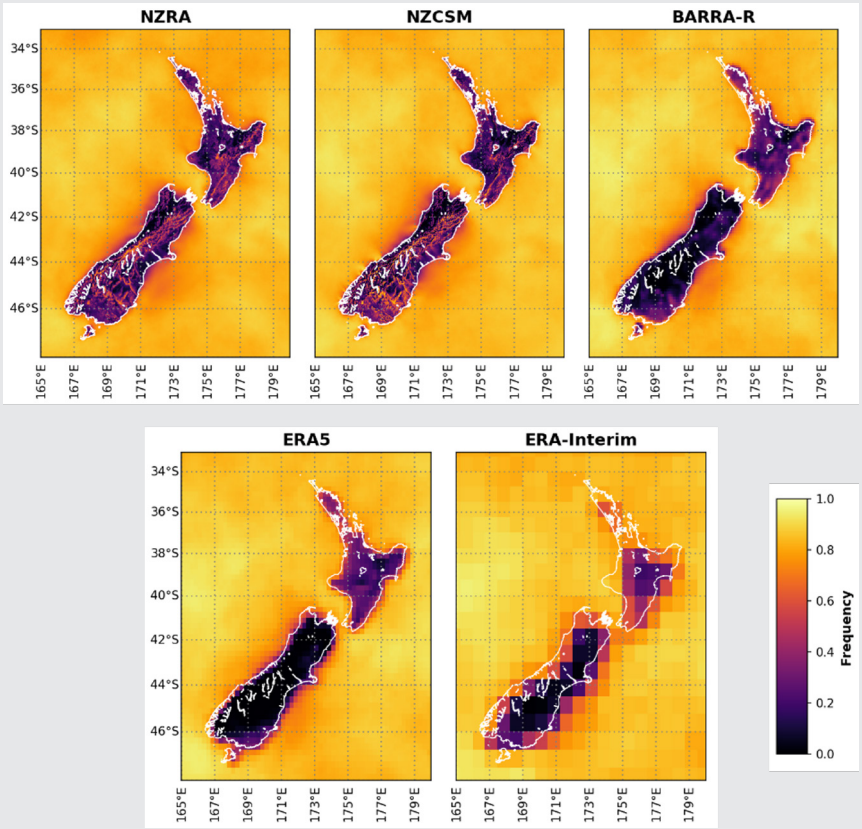

Figure 13: Frequency of surface mean wind speeds greater than 5ms^{-1} over New Zealand for the period June-July 2014 from the different reanalyses and NZCSM. The native temporal resolution of each product (see Table 1) has been used in the calculation of frequencies.

NZRA has larger biases than BARRA-R in particular are over the Auckland region (wetter) and southeastern parts of Fiordland (wetter). In addition, it appears that, for the trial period, NZRA provides an acceptable estimate of timing and intensity of rainfall rates. NZRA also outperforms its driving model in predicting strong winds over high elevation regions. Considering that the validation period was relatively short, a more comprehensive evaluation of NZRA will be conducted in future.

One of the limitations of the NZRA setup is the relatively short forecast length (9 hours) and short spin-up period (3 hours). The latter could lead to the model spin-up artefacts to still be present, especially convective clouds and rainfall as also elaborated by (Su et al., 2021). Nevertheless, NZRA outperforms its driving model and other global reanalyses in predicting precipitation, temperature and wind speed, particularly over mountainous and coastal regions.

NZRA will provide a deeper understanding of past climatology and extreme weather at local scales, particularly in places where long-term observations are not available. This knowledge can potentially contribute to several disciplines, including engineering design projects, meteorological and climatological studies, enhancing climate projection models, environmental studies, and risk and hazard assessments. Production runs of NZRA are currently underway at NIWA and will cover the 1990 – 2018 period.

ACKNOWLEDGMENTS

The authors wish to acknowledge the use of New Zealand eScience Infrastructure (NeSI) high performance computing facilities, consulting support and/or training services as part of this research. New Zealand's national facilities are provided by NeSI and funded jointly by NeSI's collaborator institutions and through the Ministry of Business, Innovation & Employment's Research Infrastructure programme. URL https://www.nesi.org.nz. We would also like to thank the Bureau of Meteorology, Australia, for providing the BARRA-R input data. We would also like to acknowledge NIWA's Strategic Science Investment Fund that supports this project.

REFERENCES

Acharya, S.C., Nathan, R., Wang, Q.J., Su, C.H., Eizenberg, N., 2019. An evaluation of daily precipitation from a regional atmospheric reanalysis over Australia. *Hydrol. Earth Syst. Sci.*, 23, 3387-3403. DOI: https://10.5194/hess-23-3387-2019

Ashrit, R., Indira Rani, S., Kumar, S., Karunasagar, S., Arulalan, T., Francis, T., Routray, A., Laskar, S.I., Mahmood, S., Jermey, P., Maycock, A., Renshaw, R., George, J.P., Rajagopal, E.N., 2020. IMDAA Regional Reanalysis: Performance Evaluation During Indian Summer Monsoon Season. *Journal of Geophysical Research: Atmospheres,* 125, e2019JD030973. DOI: https://doi.org/10.1029/2019JD030973

Bannister, R.N., 2017. A review of operational methods of variational and ensemble-variational data assimilation. *Quarterly Journal of the Royal Meteorological Society*, 143, 607-633. DOI: https://doi.org/10.1002/qj.2982

Bush, M., Allen, T., Bain, C., Boutle, I., Edwards, J., Finnenkoetter, A., Franklin, C., Hanley, K., Lean, H., Lock, A., Manners, J., Mittermaier, M., Morcrette, C., North, R., Petch, J., Short, C., Vosper, S., Walters, D., Webster, S., Weeks, M., Wilkinson, J., Wood, N., Zerroukat, M., 2020. The first Met Office Unified Model–JULES Regional Atmosphere and Land configuration, RAL1. *Geosci. Model Dev.*, 13, 1999-2029. DOI: https://10.5194/gmd-13-1999-2020

Carey-Smith, T., Andrews, P., 2016. Convective scale model verification – what can we do and what can we say?, Convective Scale Modelling Workshop, Park Royal Hotel, Singapore.

Clark, P., Roberts, N., Lean, H., Ballard, S.P., Charlton-Perez, C., 2016. Convection-permitting models: a step-change in rainfall forecasting. *Meteorological Applications*, 23, 165-181. DOI: https://doi.org/10.1002/met.1538

Davies, T., Cullen, M.J.P., Malcolm, A.J., Mawson, M.H., Staniforth, A., White, A.A., Wood, N., 2005. A new dynamical core of the Met Office's global and regional modelling of the atmosphere. *Quarterly Journal of the Royal Meteorological Society*, 131, 1759-1782. DOI: https://10.1256/qj.04.101

Dee, D.P., Uppala, S.M., Simmons, A.J., Berrisford, P., Poli, P., Kobayashi, S., Andrae, U., Balmaseda, M.A., Balsamo, G., Bauer, P., Bechtold, P., Beljaars, A.C.M., van de Berg, L., Bidlot, J., Bormann, N., Delsol, C., Dragani, R., Fuentes, M., Geer, A.J., Haimberger, L., Healy, S.B., Hersbach, H., Hólm, E.V., Isaksen, L., Kållberg, P., Köhler, M., Matricardi, M., McNally, A.P., Monge-Sanz, B., Morcrette, J.J., Park, B.K., Peubey, C., de Rosnay, P., Tavolato, C., Thépaut, J.N., Vitart, F., 2011. The ERA-Interim reanalysis: configuration and performance of the data assimilation system. *Quarterly Journal of the Royal Meteorological Society*, 137, 553-597. DOI: https://doi.org/10.1002/qj.828

Ehard, B., Achtert, P., Dörnbrack, A., Gisinger, S., Gumbel, J., Khaplanov, M., Rapp, M., Wagner, J., 2016. Combination of Lidar and Model Data for Studying Deep Gravity Wave Propagation. *Monthly Weather Review*, 144, 77-98. DOI: https://10.1175/mwr-d-14-00405.1

Frank, C.W., Pospichal, B., Wahl, S., Keller, J.D., Hense, A., Crewell, S., 2020. The added value of high resolution regional reanalyses for wind power applications. *Renewable Energy*, 148, 1094-1109. DOI: https://doi.org/10.1016/j.renene.2019.09.138

Fritts, D.C., Smith, R.B., Taylor, M.J., Doyle, J.D., Eckermann, S.D., Dörnbrack, A., Rapp, M., Williams, B.P., Pautet, P.-D., Bossert, K., Criddle, N.R., Reynolds, C.A., Reinecke, P.A., Uddstrom, M., Revell, M.J., Turner, R., Kaifler, B., Wagner, J.S., Mixa, T., Kruse, C.G., Nugent, A.D., Watson, C.D., Gisinger, S., Smith, S.M., Lieberman, R.S., Laughman, B., Moore, J.J., Brown, W.O., Haggerty, J.A., Rockwell, A., Stossmeister, G.J., Williams, S.F., Hernandez, G., Murphy, D.J., Klekociuk, A.R., Reid, I.M., Ma, J., 2016. The Deep Propagating Gravity Wave Experiment (DEEPWAVE): An Airborne and Ground-Based Exploration of Gravity Wave Propagation and Effects from Their Sources throughout the Lower and Middle Atmosphere. *Bulletin of the American Meteorological Society*, 97, 425-453. DOI: https://10.1175/bams-d-14-00269.1

Fuhrer, J., Beniston, M., Fischlin, A., Frei, C., Goyette, S., Jasper, K., Pfister, C., 2006. Climate Risks and Their Impact on Agriculture and Forests in Switzerland. *Climatic Change*, 79, 79-102. DOI: https://10.1007/s10584-006-9106-6

Gleixner, S., Demissie, T., Diro, G.T., 2020. Did ERA5 Improve Temperature and Precipitation Reanalysis over East Africa? *Atmosphere*, 11, 996.

GLOBE Task Team, 1999. The Global Land One-kilometre Base Elevation (GLOBE) Digital Elevation Model, Version 1.0, in: Hastings, D.A., Dunbar, P.K., Elphingstone, G.M., Bootz, M., Murakami, H., Maruyama, H., Masaharu, H., Holland, P., Payne, J., Bryant, N.A., Logan, T.L., Muller, J.P., Schreier, G., John, S.M. (Eds.). National Oceanic and Atmospheric Administration, National Geophysical Data Center, 325 Broadway, Boulder, Colorado 80305-3328, U.S.A.

Hanley, K., Whitall, M., Stirling, A., Clark, P., 2019. Modifications to the representation of subgrid mixing in kilometre-scale versions of the Unified Model. *Quarterly Journal of the Royal Meteorological Society*, 145, 3361-3375. DOI: https://doi.org/10.1002/qj.3624

Hartley, A.J., MacBean, N., Georgievski, G., Bontemps, S., 2017. Uncertainty in plant functional type distributions and its impact on land surface models. *Remote Sensing of Environment*, 203, 71-89. DOI: https://doi.org/10.1016/j.rse.2017.07.037

Hersbach, H., et al., 2020. The ERA5 global reanalysis. *Quarterly Journal of the Royal Meteorological Society*, 146, 1999-2049. DOI: https://doi.org/10.1002/qj.3803

Hu, G., Franzke, C.L.E., 2020. Evaluation of Daily Precipitation Extremes in Reanalysis and Gridded Observation-Based Data Sets Over Germany. *Geophysical Research Letters*, 47, e2020GL089624. DOI: https://doi.org/10.1029/2020GL089624

Keller, J.D., Wahl, S., 2021. Representation of Climate in Reanalyses: An Intercomparison for Europe and North America. *Journal of Climate*, 34, 1667-1684. DOI: https://10.1175/jcli-d-20-0609.1

Komurcu, M., Emanuel, K.A., Huber, M., Acosta, R.P., 2018. High-Resolution Climate Projections for the Northeastern United States Using Dynamical Downscaling at Convection-Permitting Scales. *Earth and Space Science*, 5, 801-826. DOI: https://doi.org/10.1029/2018EA000426

Leeper, R.D., Bell, J.E., Vines, C., Palecki, M., 2017. An Evaluation of the North American Regional

Reanalysis Simulated Soil Moisture Conditions during the 2011–13 Drought Period. *Journal of Hydrometeorology*, 18, 515-527. DOI: https://10.1175/jhm-d-16-0132.1

Lu, J., Carbone, G.J., Gao, P., 2019. Mapping the agricultural drought based on the long-term AVHRR NDVI and North American Regional Reanalysis (NARR) in the United States, 1981–2013. *Applied Geography*, 104, 10-20. DOI: https://doi.org/10.1016/j.apgeog.2019.01.005

Lu, Y., Fang, J., Pan, Y., Wang, S., Zhou, P., Yang, Y., Shao, M., Tang, J., 2021. Evaluation of 12-Years Chinese Regional Reanalysis (1998–2009): Comparison of Dynamical Downscaling Methods With/Without Local Data. *Journal of Geophysical Research: Atmospheres,* 126, e2020JD034259. DOI: https://doi.org/10.1029/2020JD034259

Mesinger, F., DiMego, G., Kalnay, E., Mitchell, K., Shafran, P.C., Ebisuzaki, W., Jović, D., Woollen, J., Rogers, E., Berbery, E.H., Ek, M.B., Fan, Y., Grumbine, R., Higgins, W., Li, H., Lin, Y., Manikin, G., Parrish, D., Shi, W., 2006. North American Regional Reanalysis. *Bulletin of the American Meteorological Society*, 87, 343-360. DOI: https://10.1175/bams-87-3-343

Miller, N.L., Bashford, K.E., Strem, E., 2003. Potential Impacts of Climate Change On California Hydrology. *Journal of the American Water Resources Association* (JAWRA), 39, 771-784. DOI: https://doi.org/10.1111/j.1752-1688.2003.tb04404.x

Minola, L., Zhang, F., Azorin-Molina, C., Pirooz, A.A.S., Flay, R.G.J., Hersbach, H., Chen, D., 2020. Near-surface mean and gust wind speeds in ERA5 across Sweden: towards an improved gust parametrization. *Climate Dynamics*, 55, 887-907. DOI: https://doi.org/10.1007/s00382-020-05302-6

Rose, S., Apt, J., 2016. Quantifying sources of uncertainty in reanalysis derived wind speed. *Renewable Energy*, 94, 157-165. DOI: https://doi.org/10.1016/j.renene.2016.03.028

Safaei Pirooz, A.A., Moore, S., Carey-Smith, T., Turner, R., Su, C.H., 2022. Evaluation of global and regional reanalyses performance over New Zealand. *Weather & Climate*, 41, 16-35.

Steinheuer, J., Friederichs, P., 2020. Vertical profiles of wind gust statistics from a regional reanalysis using multivariate extreme value theory. *Nonlin. Processes Geophys.*, 27, 239-252. DOI: https://10.5194/npg-27-239-2020

Steinke, S.W., Sabrina; Crewell, Susanne, 2019. Benefit of high resolution COSMO reanalysis: The diurnal cycle of column-integrated water vapor over Germany. *Meteorologische Zeitschrift*, 28, 165-177. DOI: https://10.1127/metz/2019/0936

Su, C.H., Eizenberg, N., Jakob, D., Fox-Hughes, P., Steinle, P., White, C.J., Franklin, C., 2021. BARRA v1.0: kilometre-scale downscaling of an Australian regional atmospheric reanalysis over four midlatitude domains. *Geoscientific Model Development*, 14, 4357-4378. DOI: https://10.5194/gmd-14-4357-2021

Su, C.H., Eizenberg, N., Steinle, P., Jakob, D., Fox-Hughes, P., White, C.J., Rennie, S., Franklin, C., Dharssi, I., Zhu, H., 2019. BARRA v1.0: the Bureau of Meteorology Atmospheric high-resolution Regional Reanalysis for Australia. *Geoscientific Model Development*, 12, 2049-2068. DOI: https://10.5194/gmd-12-2049-2019

Tait, A., Henderson, R., Turner, R., Zheng, X., 2006. Thin plate smoothing spline interpolation of daily rainfall for New Zealand using a climatological rainfall surface. *International Journal of Climatology*, 26, 2097-2115. DOI: https://10.1002/joc.1350

Tait, A., Sturman, J., Clark, M., 2012. An assessment of the accuracy of interpolated daily rainfall for New Zealand. *Journal of Hydrology* (NZ), 51, 25-44.

Tait, A., Turner, R., 2005. Generating Multiyear Gridded Daily Rainfall over New Zealand. *Journal of Applied Meteorology*, 44, 1315-1323.

Taszarek, M., Allen, J.T., Púčik, T., Hoogewind, K.A., Brooks, H.E., 2020. Severe Convective Storms across Europe and the United States. Part II: ERA5 Environments Associated with Lightning, Large Hail, Severe Wind, and Tornadoes. *Journal of Climate*, 33, 10263-10286. DOI: https://10.1175/jcli-d-20-0346.1

Tetzner, D., Thomas, E., Allen, C., 2019. A Validation of ERA5 Reanalysis Data in the Southern Antarctic Peninsula—Ellsworth Land Region, and Its Implications for Ice Core Studies. *Geosciences*, 9, 289. DOI: https://10.3390/geosciences9070289

Turner, R., Moore, S., 2017. An analysis of three years of Convective Scale Numerical Model diagnosed gusts over New Zealand, 9th Asia-Pacific Conference on Wind Engineering, Auckland, New Zealand.

Witschas, B., Rahm, S., Dörnbrack, A., Wagner, J., Rapp, M., 2017. Airborne Wind Lidar Measurements of Vertical and Horizontal Winds for the Investigation of Orographically Induced Gravity Waves. *Journal of Atmospheric and Oceanic Technology*, 34, 1371-1386. DOI: https://10.1175/jtech-d-17-0021.1

Wood, N., Staniforth, A., White, A., Allen, T., Diamantakis, M., Gross, M., Melvin, T., Smith, C., Vosper, S., Zerroukat, M., Thuburn, J., 2014. An inherently mass-conserving semi-implicit semi-Lagrangian discretization of the deep-atmosphere global non-hydrostatic equations. *Quarterly Journal of the Royal Meteorological Society*, 140, 1505-1520. DOI: https://doi.org/10.1002/qj.2235

Yang, Y., Moore, S., Uddstrom, M., Turner, R., Carey-Smith, T., 2017. Model moist bias in the middle and upper troposphere during DEEPWAVE. *Atmospheric Science Letters*, 18, 161-167. DOI: https://doi.org/10.1002/asl.738

Yoshimura, K., Kanamitsu, M., 2008. Dynamical Global Downscaling of Global Reanalysis. *Monthly Weather Review*, 136, 2983-2998. DOI: https://10.1175/2008mwr2281.1

Zhang, H., Cao, Y., Zhang, Y., Terzija, V., 2018. Quantitative synergy assessment of regional wind-solar energy resources based on MERRA reanalysis data. *Applied Energy*, 216, 172-182. DOI: https://doi.org/10.1016/j.apenergy.2018.02.094

Book review

Ciaran Doolin[1,2]

[1] Meteorological Service of New Zealand (MetService – Te Ratonga Tirorangi), PO Box 722, Wellington, New Zealand
[2] Centre for Science in Society, Victoria University of Wellington – Te Herenga Waka
Correspondence: ciaran.doolin@metservice.com

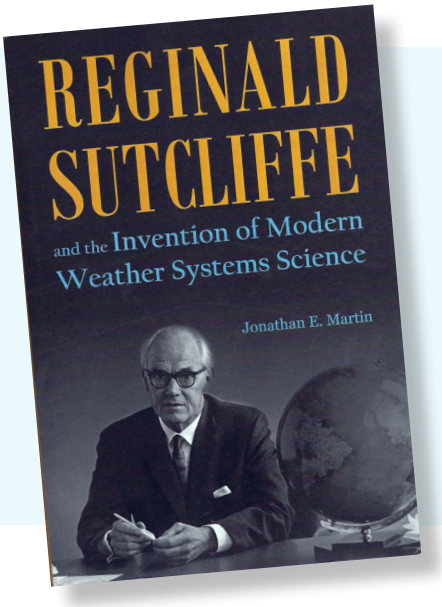

Jonathan E. Martin. 2021.

Reginald Sutcliffe and the Invention of Modern Weather Systems Science.

West Lafayette, Indiana: Purdue University Press.
484 pp. 34 illustrations.
US$39.99.

Atmospheric science is short on book-length biographies of its heroes compared to other fields in the physical sciences[1]. As such, Jonathan Martin's recent biography of renowned British meteorologist Reginald Sutcliffe is a welcome addition to the literature. Martin's study examines Sutcliffe's best-known intellectual contributions – his theory of development and his introduction of isobaric coordinates – as well as his activity with the British Meteorological Office, World Meteorological Organization, and the University of Reading. The author makes the case that Sutcliffe's contributions to meteorological theory constituted a revolutionary advance in the field.

Martin is a Professor in the Department of Atmospheric and Oceanic Sciences at the University of Wisconsin-Madison and is the author of the popular textbook *Mid-Latitude Atmospheric Dynamics*. Martin first acquired a taste for history of science as a graduate student at the University of Washington during the 1980s. Thirty years or so later, this interest has apparently only deepened as Martin decided to dedicate his first sabbatical to the task of completing a biography of Sutcliffe. The outcome of five years of investigation, the author's study draws on extensive primary and secondary sources, including detailed information obtained from Sutcliffe's relatives.

Reginald Sutcliffe was born in 1904 in Wrexham, Wales, but grew up in Cleckheaton, Yorkshire, England. His father, Ormerod, was a grocery store manager at the Cleckheaton Cooperative. Ormerod was an autodidact with wide intellectual interests. He was also a socialist, a supporter of the Labour Party, and was involved with the local Workers' Educational Association (WEA). Ormerod took evening classes in biology at the Cleckheaton Technical School, and later in life he was asked to serve as an instructor at the WEA. Naturally, Reginald's parents valued education and encouraged academic achievement amongst Reginald and his brothers.

1 Some international examples include Friedman's (1989) study of Vilhelm Bjerknes and the Bergen School of Meteorology; Hamblyn's (2002) portrait of Luke Howard, the author of modern cloud nomenclature; Guadalupe's (2014) biography of Cuban hurricane scientist Father Benito Viñes; and Gribbin's and Gribbin's (2016) study of Robert Fitzroy, Britain's first weather forecaster. More recent publications include Potter's (2020) study of Cleveland Abbe, America's first weather forecaster; and Fleming's (2020) biography of Joanne Simpson, a pioneering tropical meteorologist. To my knowledge, the only biography of a New Zealand meteorologist – and an incomplete one at that – is Isabel Kidson's (1941) study of her late husband Edward Kidson.

Sutcliffe won a County Minor Scholarship to Whitcliffe Mount School where he completed his secondary education. A talented student in mathematics and physics, he won a County Major Scholarship to the University of Leeds, where he gained a BSc with first class honours in mathematics in 1925. Impressed by his performance, the university encouraged Sutcliffe to pursue a PhD. He won the Alfred Law Scholarship, which funded his PhD studies in mathematics under the supervision of William Berwick. Upon graduating in 1927 he discovered that there were limited employment opportunities for mathematicians besides academia. However, he was advised that the British Meteorological Office sometimes employed mathematics graduates; his application there was successful and he began his meteorological career in 1927.

Sutcliffe trained as a forecaster – a "training" he described as learning through osmosis – and spent many years working at stations around Europe. A significant event in Sutcliffe's development as a meteorologist occurred in late 1928 when he arrived at his new post in Malta to be greeted by Tor Bergeron, a leading figure in the innovative Bergen School of Meteorology, who was attached to the office at the invitation of the British government. Bergeron was to spend a period of six months studying Mediterranean weather using the methods of frontal and air mass analysis that the Bergen School had pioneered. Sutcliffe keenly observed Bergeron's careful, systematic synoptic analysis featuring fronts, isobars, isallobars, and shaded air masses. Sutcliffe recalled this experience as "a revelation after the slapdash drawing of isobars which was all that was generally attempted in UK offices at the time" (p. 50). The lessons he drew from these interactions stood him in good stead for years to come: Sutcliffe later commented that he always "tried to employ the same thorough methods and always felt one step ahead of anything being done in the UK for the next 15 years" (p. 50)[2]. However, this fortuitous time with Bergeron had another long-lasting impact on Sutcliffe's career: his engagement with the Norwegian Cyclone Model (NCM) – a central feature of the Bergen School's scientific framework. Though initially an enthusiastic student of the NCM, Sutcliffe eventually came to the conclusion that it was theoretically deficient; this realisation pushed him to develop a dynamical theory of his own.

During this period, Sutcliffe carried out research in his spare time, some of which resulted in impactful publications. Although Sutcliffe acknowledged the success of the NCM as a description of the life cycle of extratropical cyclones and its utility in forecasting, by the late 1930s he had concluded that it failed to give a satisfactory theoretical account of the process of development. For Sutcliffe, any theory of development needed to explain how the atmosphere produces situations where there is an excess of upper-level divergence over low-level convergence, resulting in net removal of air from a column and decreasing surface pressure.

In two ground-breaking papers, Sutcliffe (1938; 1939a) combined mathematical rigour and sound physical reasoning to derive equations which expressed a dynamical theory of development. The key step in Sutcliffe's reasoning was his recognition that surface pressure changes happened due to the vertical distribution of divergence/convergence of the ageostrophic wind. When he assumed a constant Coriolis parameter, Sutcliffe showed that the contribution of the geostrophic wind to the overall divergence of the wind field is eliminated, leaving only the contribution from the ageostrophic wind. Because the acceleration is always 90 degrees to the left of the ageostrophic wind, the problem then became mapping the field of acceleration. Though clearly a capable theoretician, Sutcliffe was at heart a forecaster: another important feature of these works was Sutcliffe's articulation of a graphical method that would allow forecasters to utilise the physical insight obtained from his equations in the practical interpretation of operational analyses[3].

In 1939 he published *Meteorology for Aviators,* which was read widely by Royal Air Force (RAF) pilots during the Second World War. In the early phase of the war, Sutcliffe was mobilised into the RAF at the rank of Squadron Leader and was sent to France with the British Expeditionary Force to forecast for flying operations over the continent. As France fell under Nazi control, Sutcliffe was evacuated back to England. Later he was posted to Bomber Command to organise forecasting for raids over Europe. His participation in the bombing raids over Germany, albeit at a distance, left

2 Doolin (2020) examines the story of the emergence of Bergen School ideas in the Southern Hemisphere during the 1930s under the supervision of Edward Kidson, Director of the Meteorological Service of New Zealand. Norwegian meteorologist Jørgen Holmboe spent much of 1934 in New Zealand, providing Kidson with the kind of fruitful interactions Sutcliffe enjoyed with Bergeron in Malta. In fact, Bergeron was scheduled to come to New Zealand in 1938 for six months but had to cancel at the last minute due to a bout of ill health.

3 Interestingly, in the first of these two papers Sutcliffe deployed the term "quasi-geostrophic". In fact, this was the second time the term had been used; it appeared for the first time in an English-language publication in a paper Sutcliffe co-authored with Charles Durst (Durst & Sutcliffe 1938).

him with lifelong nightmares. After being appointed chief meteorologist of the Allied Expeditionary Air Force in late March 1944 Sutcliffe was involved in the historic forecasting effort for the Normandy landings on 6 June.

Despite the at-times extreme workload pressures of wartime forecasting, Sutcliffe somehow found the energy for more research. A notable innovation Sutcliffe introduced during the war years, in collaboration with the Belgian polymath Odon Godart, was the adoption of pressure instead of geometric height as the vertical coordinate. In two important memos, they showed how the use of isobaric coordinates simplified the equations for the geostrophic and thermal winds, and the continuity equation (Sutcliffe 1943; Sutcliffe & Godart 1943). For example, the use of isobaric coordinates for the geostrophic wind equation removed the dependency on density, meaning that a single geostrophic wind scale could be used at all levels. Sutcliffe and Godart also demonstrated a method for constructing upper-air charts using surface pressure analyses and upper-air temperatures, and for prognosing the evolution of upper-air charts by calculating the column-average geostrophic temperature advection.

After Germany's defeat, Sutcliffe was engaged in reorganising the German meteorological service. Upon his return to England, he resumed his work at the Meteorological Office. He quickly set to work finessing his ideas about development, leading to his famous "development theorem" (Sutcliffe 1947). In this paper he showed that the difference in divergence between the top and bottom of a column is related to the advection of the combined surface and upper-level vorticity by the thermal wind. The mathematical elegance of this result was matched by its immediate applicability in operational forecasting. In Martin's view, Sutcliffe's development theorem "represented a revolution in synoptic-dynamic meteorology" in which Sutcliffe had "achieved what no one before him had – he had placed understanding of the progression and development of midlatitude weather systems on an unshakably solid scientific foundation" (pp. 157-158)[4].

Sutcliffe eventually became Director of Research at the Meteorological Office and guided many projects to fruition, most notably the British effort in numerical weather prediction (NWP). Martin argues that the influence of Sutcliffe's development theorem on British meteorology was a factor in the different paths taken by British and American NWP efforts from around 1948. Sutcliffe's work biased British efforts towards baroclinic models from the start, whereas Jule Charney's group in the United States were initially focused on barotropic models. On this aspect, Martin is anxious to dispel the reputation Sutcliffe has apparently acquired of being an NWP sceptic. Sutcliffe's attitude towards NWP had several facets. Firstly, he felt that though NWP was likely to prove useful in forecasting in his lifetime, he doubted it would constitute the revolutionary advance that some anticipated at the time. Secondly, he lamented that the scientific problem he had been faced with as a young forecaster – however frustrating – would be rendered less satisfying for the analyst as NWP took much of the interpretative challenge out of the process. Finally, he felt that the advent of electronic computers had come at a time when meteorological theory was just starting to undergo a renaissance and consequently energy was directed away from theoretical work and into NWP. In Sutcliffe's words:

> Sometimes I think the electronic computer came too soon. If we'd followed on from Rossby's ideas, which came long before computers – the first idea on vorticity fields, and then the idea of the thermal winds that I produced, and similar things – the dynamicists would have altered weather forecasting quite radically, in quite a revolutionary way, without the high speed computer. Because the ideas didn't need a high speed computer (p. 357).

In the post-war period, Sutcliffe also became heavily involved in international meteorological collaboration, most notably with the World Meteorological Organization and International Association for Meteorology and Atmospheric Physics. He was the recipient of many scientific honours. Perhaps chief among these was his election as a Fellow of the Royal Society in 1957, an achievement which was widely seen as recognition that meteorology had been accepted by the wider scientific community as a real science.

Following his retirement from the Meteorological Office in 1965 he immediately founded the Department of Meteorology at University of Reading. Reading became the first university in Britain to offer an undergraduate course

4 It would be interesting to trace the influence of Sutcliffe's ideas on activity in New Zealand. On the other side of the Tasman, Bill Gibbs, a post-war Director of the Bureau of Meteorology, singles out Sutcliffe (1947) as the most important paper he encountered in the period immediately after the end of the war (Taba & Gibbs 1988, p. 248). It seems highly likely that Sutcliffe's work had a similar impact in New Zealand, but to uncover this would require some digging into internal Meteorological Service publications from the period as de Lisle's (1986) history of the organisation apparently makes no mention of Sutcliffe's influence.

in meteorology. He retired from academia in 1970, but maintained an involvement in meteorological affairs until his death in 1991.

One of the many interesting features of Martin's study is that it is not only a scientific biography: it is also a work of science communication. The author brings to bear his considerable experience as an educator in atmospheric science to produce a narrative that communicates the scientific concepts in plain language as he simultaneously catalogues the events of Sutcliffe's life and scientific career. Beginning with explanations of elementary meteorological concepts, Martin builds towards the more advanced dynamical ideas Sutcliffe is best known for, fortifying the reader's understanding with simple yet illuminating illustrations of the physical processes under discussion. With this approach Martin has broadened the potential appeal of his book beyond the rather narrow confines of the disciplines of atmospheric science and history of science; this book should be accessible to an interested, non-specialist readership. Given Sutcliffe's long-standing involvement with popular and specialist scientific education, this feature makes Martin's study an especially fitting tribute to his subject.

Historians of science have in recent years approached scientific biography with a degree of wariness (e.g., Greene 2007; Nye 2006; Porter 2006). Some critics argue that biography as a literary device tends to overstate the role of individual activity in the history of science, in the process washing out the broader cultural, social, and intellectual context within which science necessarily takes place. The author, while not a professional historian, does an able job of situating Sutcliffe's life within this broader context thereby minimising some of the potential pitfalls of biography as a literary genre. For example, somewhat to my surprise, the book begins with a lengthy account of the labour movement's struggle for the democratisation of education in the highly class-stratified society of turn-of-the-century Britain. Sutcliffe, being from a working-class family, was a direct beneficiary of the partial success of this movement.

I have a few minor criticisms of this study. Some of the chapters were excessively long. The chapter on the war years came to 65 pages while the chapter on Sutcliffe's international activities amounted to a gruelling 78 pages! These each could have been split into two chapters. Furthermore, I felt at times a more judicious selection could have been made of Sutcliffe's statements in various publications. This was particularly evident in the chapter on Sutcliffe's international activity in which the author seems to have nearly exhaustively quoted from Sutcliffe's many contributions to various international symposia, congresses, committee meetings, etc. A smaller sample of quotations representative of Sutcliffe's opinions and their evolution over time would have made for more fluid reading – these long tracts of commentary are likely to be lost on a non-meteorologist, or even a non-historically-inclined meteorologist. Finally, although I mentioned earlier that this book is a commendable exercise in science communication, in addition to history of science, there are places where this effort falters. Perhaps unsurprisingly, this was most evident in the sections discussing Sutcliffe's main theoretical contributions. A non-meteorologist would, I think, struggle to follow some of these discussions and likely would just have to take Martin's word that Sutcliffe's contributions were uniquely insightful and useful. Martin makes a valiant attempt to explain these concepts and that he at times falls short has less to do with his particular presentation and more to do with the simple fact that science can be rather complicated sometimes.

Martin's passion for his subject – both the science and the individual scientist he is profiling – leaps off the pages of this book. This biography was undoubtedly a labour of love.

Martin's passion for his subject – both the science and the individual scientist he is profiling – leaps off the pages of this book. This biography was undoubtedly a labour of love. In the acknowledgments, Martin describes the research process as an "academic exercise fueled by personal interest [that transformed] into a life-changing intellectual and spiritual experience" (p. 372). Though one shouldn't expect to get through this rather substantial book in a weekend of leisurely reading, it is nevertheless certainly worth the effort to see this fascinating, meticulously crafted story through to the end.

REFERENCES

De Lisle, J. F. 1986. *Sails to Satellites: A History of Meteorology in New Zealand*. Wellington, New Zealand: Meteorological Service of New Zealand.

Doolin, C. 2020. Norway Comes to New Zealand: Edward Kidson, Jørgen Holmboe, and the Mordernization of Australasian Meteorology. *Bulletin of the American Meteorological Society,* 101(12): E2095-E2112.

Durst, C. S. & Sutcliffe, R. C. 1938. The importance of vertical motion in the development of tropical revolving storms. *Quarterly Journal of the Royal Meteorological Society,* 64: 75-84.

Fleming, J. R. 2020. *First Woman: Joanne Simpson and the Tropical Atmosphere*. Oxford: Oxford University Press.

Friedman, R. M. 1989. *Appropriating the Weather: Vilhelm Bjerknes and the Construction of a Modern Meteorology.* Ithaca, New York: Cornell University Press.

Greene, M. T. 2007. Writing Scientific Biography. *Journal of the History of Biology*, 40: 727-759.

Gribbin, J. & Gribbin, M. 2016. *Fitzroy: The Remarkable Story of Darwin's Captain and the Invention of the Weather Forecast.* Golden, Colarado: ReAnimus Press.

Guadalupe, L. E. R. 2014. *Father Benito Vines: The 19th-Century Life and Contributions of a Cuban Hurricane Observer and Scientist*. Boston, Massachusetts: American Meteorological Society.

Hamblyn, R. 2002. *The Invention of Clouds: How an Amateur Meteorologist Forged the Language of the Skies*. New York: Picador.

Kidson, I. 1941. *Edward Kidson*. Christchurch, New Zealand: Whitcombe & Tombs.

Martin, J. E. 2006. *Mid-Latitude Atmospheric Dynamics: A First Course.* Chichester, England: Wiley.

Nye, M. J. 2006. Scientific Biography: History of Science by Another Means? *Isis*, 97(2): 322-329.

Porter, T. M. 2006. Is the Life of the Scientist a Scientific Unit? *Isis*, 97(2): 314-321.

Potter, S. 2020. *Too Near for Dreams: The Story of Cleveland Abbe America's First Weather Forecaster.* Boston, Massachusetts: American Meteorological Society.

Sutcliffe, R. C. 1938. On development in the field of barometric pressure. *Quarterly Journal of the Royal Meteorological Society,* 64: 495-509.

Sutcliffe, R. C. 1939a. Cyclonic and anticyclonic development. *Quarterly Journal of the Royal Meteorological Society,* 65: 518-524.

Sutcliffe, R. C. 1939b. *Meteorology for Aviators*. London: His Majesty's Stationary Office.

Sutcliffe, R. C. 1943. Construction of Upper Isobaric Contour Charts, *Meteorological Office, Synoptic Division Technical Memorandum*, 50: 9.

Sutcliffe, R. C. & Godart, O. H. 1943. Forecasting of Upper Isobaric Contour Charts, *Meteorological Office, Synoptic Division Technical Memorandum*, 50: 9.

Sutcliffe, R. C. 1947. A contribution to the problem of development. *Quarterly Journal of the Royal Meteorological Society,* 73: 370-383.

Taba, H. & Gibbs, W. J. 1988. Interview with Dr W. J. Gibbs, in *The "Bulletin" Interviews*, edited by Hessam Taba. Geneva: World Meteorological Organization: 243-256.